Using Surface Analysis to Investigate how Adsorbed Protein Structure Changes with Controlled Changes in Surface Chemistry

A Case Study Involving Bare & Sodium Styrene Sulfonate-Grafted Gold Surfaces

Rami N. Foster

A dissertation submitted in partial
fulfillment of the requirements for
the degree of

Doctor of Philosophy

University of Washington
2015

Reading Committee:
David G. Castner, Chairman
François Baneyx
Jim Pfaendtner

Program Authorized to Offer Degree:
Chemical Engineering

Abstract

Protein adsorption on synthetic surfaces is an important and widely studied phenomenon in biomaterials research. Despite its importance, it is still poorly understood. Therefore, the ultimate goal of this thesis is to contribute toward a better understanding of the protein-biomaterial interface, with application toward the next generation of biomaterial implants. Narrowing this broad objective down to something more specific, this thesis represents a body of work focused on the interaction of blood plasma proteins with sodium styrene sulfonate (NaSS) grafted surfaces. The approach to achieving this objective is straightforward.

First, proof-of-concept must be established that NaSS can be successfully grafted to a given surface. A thorough characterization of NaSS films grafted from titanium and silicon oxide surfaces using atom transfer radical polymerization (ATRP) is presented herein.

Next, the grafting procedure must be optimized and scaled in order to reliably produce sufficient quantities of NaSS-grafted samples to meet the demands of protein adsorption studies. Using a 24 factorial experimental design and "activators are continuously regenerated by electron transfer" (ARGET) ATRP chemistry, an optimized NaSS grafting procedure was developed. The findings here may be generally applied as a starting point for grafting other polymers to a variety of surfaces.

The last step is application—to use the NaSS films for their intended purpose. Surface analysis techniques were applied to characterize changes in adsorbed bovine serum albumin (BSA), bovine fibrinogen (Fgn), bovine immunoglobulin G (IgG), and bovine plasma films between bare and NaSS-grafted gold surfaces. All three proteins and plasma adsorb more readily to, and have a higher affinity for gold than NaSS surfaces. However, at higher concentrations NaSS adsorbs similar amounts (for plasma) or more (for BSA and Fgn) total protein than gold. The only protein that NaSS surfaces adsorb less of than gold is IgG, because IgG adopts a highly denatured conformation on NaSS. Each adsorbed IgG molecule takes up more space on NaSS compared to gold surfaces, resulting in less total protein adsorbed at all concentrations. Still, with the exception of BSA and plasma on gold surfaces, neither surface appeared to have saturated at the highest protein solution concentration studied. Using principal component analysis (PCA) of just the amino acid ToF-SIMS mass fragments, it was determined that all three proteins and plasma adsorb differently on NaSS and gold surfaces, and that the structure of the adsorbed protein films change with surface concentration. One difference between adsorbed

films on both surfaces, determined using peak ratios for buried/surface amino acids for each protein, is that adsorbed proteins denature more on NaSS than gold. Also, using peak ratios of non-uniformly distributed amino acids, small differences in average orientations were found between the two surfaces for BSA and IgG films. Finally, principal component (PC) modeling, was used to track changes in adsorbed plasma films with time. On NaSS surfaces the plasma films appear to be more BSA-like at short adsorption times, and more Fgn-like at longer adsorption times. Similarly, on gold surfaces the plasma films on appear to start out more IgG-like and become more Fgn-like with increasing adsorption time. However, the PC model included only the three proteins studied here, where plasma is a complex mixture of hundreds of proteins. Therefore, while both gold and NaSS appear to adsorb more Fgn with time, further study is required to confirm that this is truly representative of the final state of the adsorbed plasma films.

Table of Contents

List of Abbreviations

AFM: Atomic force microscopy

AIBN: Azobisisobutyronitrile

Amu: Atomic mass unit

ANOVA: Analysis of variance

ARGET: Activators aRe continuously reGenerated by Electron Transfer

ATRP: Atom transfer radical polymerization

Bpy: 2,2'-bipyridine

BSA: Bovine serum albumin

ClSi: Trichlorosilane/10-undecen-1-yl 2-bromo-2-methylpropionate

CPBSzI: Citrate and phosphate buffered saline with sodium azide and sodium iodide

DI: Deionized

DOF: Degrees of freedom

eV: Electron volt unit of energy equal to 1.6×10^{-19} Joules

Fgn: Fibrinogen

IgG: Immunoglobulin G

IMFP: Inelastic mean free path

IR: Infrared

MeOH: Methanol

M_n: Number average molecular weight

MPS: 3-methacryloxypropyltrimethoxysilane

MS: Mean square

MSE: Mean square error

M_w: Weight average molecular weight

NaSS: Sodium styrene sulfonate

PBS: Phosphate buffered saline

PC: Principal component

PCA: Principal component analysis

PDMS: Poly(dimethyl siloxane)

PEG: Poly(ethylene glycol)

PET: Poly(ethylene terephthalate)

pNaSS: Poly(sodium styrene sulfonate)

RMS: Root mean square

SA: Specific aim

SBF: Simulated body fluid

SEM: Scanning electron microscopy

SFG: Sum frequency generation

SIMS: Secondary ion mass spectrometry

SS: Sum of squares

TOA: Takeoff angle

ToF-SIMS: Time-of-flight secondary ion mass spectrometry

UHV: Ultra-high vacuum

VASE: Variable angle spectroscopic ellipsometry

VMD: Visual molecular dynamics

XPS: X-ray photoelectron spectroscopy

XRD: X-ray diffraction

List of Figures

List of Tables

Acknowledgements

First and foremost, I must acknowledge Jesus Christ as my Captain, God, and King. I know it's cliché to thank God after a big accomplishment. If my words bring to mind a running back pointing to the sky after scoring a touchdown, let me set the record straight. I'm not showboating across the goal line, spiking my thesis in the end zone, and giving "all glory to God" as I touchdown dance to the podium to collect my PhD-degree/Super Bowl MVP trophy. No, grad school was far too rough an experience for that. Jesus is carrying me across the goal line bloodied, bruised, and completely humbled. The MVP trophy belongs to Him. It's with that in mind that I write: to God my Savior, who alone is wise, be all glory and majesty, dominion, and power, both now and forevermore.

After the Almighty, my family has been my biggest lifeline. The love and support of my parents, who traded their legal names for Mamsi and Dad when they had children, has been absolutely invaluable. My brothers—Dani, Sami, and Naji—are the best friends a guy can ask for. We've all moved on to the next stage of life, but there will always be a special place in my heart for the holidays and vacations spent with them, gaming, watching movies, and drinking beer in the basement at home. Although not technically family, my best friend, Jeff Arnold, is like a brother to me. He's had my back since the sixth grade. Grad school was no exception.

Sticking with the theme of non-blood brothers, I owe a lot to Sean Robertson, my first community group leader and the older brother I never had. I learned a lot from Sean: the proper Marine way to iron my clothes, spit shine my shoes, detail a car, and even make a cup of coffee. However, most of what I learned, Sean never knew he taught me. The most important lessons I picked up by quietly watching his example as a warrior who dearly loves Jesus, his family, and his country. I'm a better man just for having known him.

Next, I need to acknowledge my Seattle support group—the guys and gals in the trenches with me. In no particular order: Jordan Green, Austin Webb, Meagan Wright, Nadav Egar, Erica Chong, and Sean Yeung. To them it may have looked like we were just tossing the pig skin, splitting wood, or grabbing a bite, a beer, or a coffee. But each one of them was God-sent to see me through a particular leg of my grad school journey.

Friends are great, but I'm not allowed to take my day out on them and beat them up. The UW club judo team, on the other hand, is a different story. Many of my fondest memories of Seattle

(and the ones I was sorest from the next day) took place in mat room B in the IMA. So here's to coach Dave Christianson, and the brave warriors who let me beat them up—and who gave as good as they got.

Finally, I am not the same wayward, prodigal young man who showed up to UW in the fall of 2010. While all the credit belongs to Jesus, His chosen instrument was the one man on earth who could have gotten my attention back then. Through this man's straightforward preaching, his uncompromising dedication to the truth, his strong leadership, and his heart for young men like me, God strengthened me to weather the storms and fulfill His calling to graduate with my PhD in chemical engineering from UW – Seattle. Therefore, as a token of gratitude, and for faithfully pursuing his own calling to shepherd young men like me…

I dedicate this thesis to Pastor Mark Driscoll.

1. Introduction

1.1. Motivation

Protein adsorption on synthetic surfaces is arguably the most important and widely studied phenomenon in biomaterials research today. It effects a variety of fields including protein chip microarrays,[1-4] protein purification by affinity chromatography,[5, 6] enzymatic bioreactors,[7, 8] and most important to this body of work, biomedical implants.[9-11] Despite its importance, the protein-biomaterial interface is still poorly understood. What is known is that biomaterial surfaces are covered with a random assortment of proteins almost immediately after contacting a protein-containing solution, such as blood plasma.[9, 11] These proteins adsorb to the surface in a variety of orientations and conformations, resulting in a haphazardly formed monolayer film. In the case of biomedical implants, the body, which can only "see" the biomaterial surface, fails to recognize the protein film, and attacks and attempts to digest the implant. Since most implants are too large to digest, the body gives up and instead walls off the foreign object in a fibrous capsule. This prevents intimate contact and integration with the surrounding tissue, potentially leading to implant failure, and even severe, antibiotic-resistant bacterial infections that are often curable only by surgically removing the implant. The cascade of events from nonspecific protein adsorption to fibrous encapsulation is known as the foreign body response, and is seen as the main enemy of progress in biomaterials research.[11]

Since proteins mediate many important cell interactions, and the foreign body cascade begins with nonspecific protein adsorption, the protein-biomaterial interface is a natural place to focus to "defeat" the foreign body response. One main strategy is to engineer materials that resist protein adsorption altogether. To this end poly(ethylene glycol) (PEG) and plasma-deposited tetraglyme films have been developed, which do a wonderful job resisting protein adsorption in vitro. Once in vivo, however, these materials still elicit a foreign body reaction.[12] Also, relatively little long-term testing of these materials has been done, and it is unclear if they would remain protein resistant after extended periods in vivo.[12] A second strategy is to concede that proteins will adsorb and—rather than try to avoid it—engineer biomaterial surfaces to control the adsorbed film composition, and individual protein orientation and conformation.[13] Not only can negative outcomes be avoided with this strategy, but positive responses elicited, such as wound healing. Thus, the ultimate goal of this work is a better understanding of the protein-biomaterial interface with application toward the next generation of biomaterial implants. This objective is

admittedly a bit broad and ambiguous; therefore, the specific focus of this work is narrowed to the interaction of blood plasma proteins with sodium styrene sulfonate (NaSS) grafted surfaces.

Since, upon implantation, biomaterial surfaces are immediately covered with a nonspecifically adsorbed layer of blood plasma proteins, they are an important class of proteins to study if this work is to be applied toward next-generation biomedical implants.[6, 9] NaSS-grafted surfaces were chosen as the system of interest since NaSS has shown promise in recent studies investigating the osseointegration of NaSS-grafted implants. Specifically, in vitro studies have shown increased proliferation and adhesion of fibroblasts,[14] MG63 osteoblast-like cells,[15-17] and human mandibular osteoblasts[18] on NaSS-modified titanium and poly(ethylene terephthalate) (PET) surfaces. Promising results have also been obtained in vivo for the same surfaces.[18-20] Since the foreign body response begins with non-specific protein adsorption, and cell function on surfaces is mediated by adsorbed proteins, NaSS-grafted implants are hypothesized to preferentially adsorb certain plasma proteins in an orientation and conformation that modulates the foreign body response and promotes formation of new bone. Beyond the potential application of NaSS, the biomaterials community still has a limited grasp of how adsorbed protein film properties are altered with controlled changes in surface chemistry. Polymer grafting is an excellent way of making controlled changes to surface chemistry and NaSS is an interesting system as it allows us to study the effect of introducing negatively charged sulfonate groups to the surface. Therefore, the specific aims of this work revolve around the successful fabrication of NaSS-grafted surfaces; optimizing and scaling the grafting method to reliably produce enough samples to study protein adsorption; and using surface analysis techniques to contrast protein adsorption on bare and NaSS-grafted gold surfaces.

1.2. Specific Aims

Specific Aim #1: Characterization of NaSS films grafted from titanium and silicon substrates via surface initiated atom transfer radical polymerization (ATRP).

Objective: Using surface analysis techniques such as time-of-flight secondary ion mass spectrometry (ToF-SIMS) and atomic force spectroscopy (AFM) requires smooth and chemically uniform substrates are required. ATRP is a living polymerization method known for producing low polydispersity polymer chains $(M_w/M_n < 1.3)$ in solution, which translates to uniform films

when grafted from a surface. Therefore, the goal is to use ATRP to graft thick, uniform NaSS films from titanium surfaces.

Methodology: ATRP was used to graft NaSS from trichlorosilane/10-undecen-1-yl 2-bromo-2-methylpropionate functionalized bare and titanium-coated diced silicon wafers. The bare silicon substrates were used to examine NaSS film uniformity. The titanium-coated substrates were used to examine the suitability of the ATRP method for grafting NaSS from the surface of titanium implants. The composition, molecular structure, thickness, and topography of the grafted NaSS films were characterized with X-ray photoelectron spectroscopy (XPS), time-of-flight secondary ion mass spectrometry (ToF-SIMS), variable angle spectroscopic ellipsometry (VASE), and atomic force microscopy (AFM), respectively. This work can be found in chapter 3 and results have been published in the *Journal of Vacuum Science and Technology A*, 2013 (31): 06F103.

Specific Aim #2: Optimization of and scaling of activators regenerated by electron transfer (ARGET) ATRP grafting of NaSS from titanium surfaces.

Objective: While ATRP can be used to graft chemically uniform and smooth polymer films from surfaces, it is procedurally difficult to scale to both larger batches and sample sizes. In ARGET-ATRP, the traditional ATRP is modified to make the procedure much more scalable. Much of the ARGET-ATRP literature, however, focuses on solution-phase polymerizations; not much work has been done optimizing polymer grafting conditions. Therefore, the goal is to optimize reaction conditions for ARGET-ATRP grafting of NaSS from titanium surfaces.

Methodology: XPS and AFM were used to characterize and optimize the grafting of NaSS from trichlorosilane/10-undecen-1-yl 2-bromo-2-methylpropionate-functionalized titanium surfaces in hopes of discovering principles broadly applicable to the optimization of ARGET-ATRP grafting of polymer films in general. To this end a 2^4 factorial design was performed to study the following variables: (A) ATRP initiator surface functionalization reaction time; (B) grafting reaction time; (C) $CuBr_2$ catalyst concentration; (D) reducing agent (vitamin C) concentration. This work can be found in chapter 4 and results have been accepted in the *Journal of Vacuum Science and Technology A*.

Specific Aim #3: Characterization of single-component and blood plasma protein films adsorbed on bare and NaSS-grafted gold substrates.

Objective: Specific Aims #1 and #2 established a scalable and reliable method of making controlled changes to the surface chemistry of a variety of substrates. The goal of this Specific Aim is to utilize that framework to study changes in the properties of adsorbed protein films on bare and NaSS-grafted gold substrates.
Methodology: Single-component adsorption isotherms were measured at three different solution concentrations of bovine serum albumin (BSA), bovine plasma fibrinogen (Fgn), and bovine immunoglobulin G (IgG) on both bare and NaSS-grafted gold. Adsorption of bovine blood plasma was also studied at a single concentration and times varying from 5 to 120 minutes. Protein surface concentrations were determined via XPS nitrogen content. Protein orientation and conformation were characterized with ToF-SIMS. A principal component analysis (PCA) model, constructed from the ToF-SIMS data, was used to interpret spectra collected from bare and NaSS-grafted samples exposed to bovine blood plasma.

1.3. Organization of this document

Chapter One provides an overview of this dissertation and the topics covered within.

Chapter Two provides an extended background on ATRP, protein adsorption, and the surface analysis techniques used in this work.

Chapter Three describes the fabrication and characterization of NaSS-grafted substrates, as summarized in Specific Aim #1. This work has been published: J. Vac. Sci. Tech. A, 31(6), 06F103-109 (2013).

Chapter Four describes the optimization of and scaling of ARGET-ATRP grafting of NaSS from titanium surfaces, as summarized in Specific Aim #2. This work has been accepted in the J. Vac. Sci. Tech. A (2015).

Chapter Five describes the characterization of single-component and blood plasma protein films adsorbed on bare and NaSS-grafted gold substrates, as summarized in Specific Aim #3.

Chapter Six recapitulates the conclusions reached in this thesis and proposes future directions for continuation of this work.

2. Materials and Methods

This chapter was written with two goals in mind. First, to lay a foundation so that someone not intimately familiar with surface analysis, but with a sufficiently technical background, can understand this thesis. As such, the use of overly technical jargon, acronyms, and unnecessary details was avoided whenever possible. Second, to satisfy my curiosity and deepen my knowledge of the inner-workings of the instruments used in this work. Each instrument is both immensely complicated and extremely fascinating. And while only superficial knowledge of XPS, for example, is absolutely necessary to obtain and analyze data, misinterpretation and false conclusions often come of such a "black box" approach. That being said, this chapter is not intended to be an exhaustive resource. Entire books have been written on the inner-workings and theory of each instrument. In fact, unless otherwise cited, the sections below are simply distillations of the material found in various chapters throughout *Surface Analysis: The Principal Techniques* (2^{nd} Ed.). This book is recommended as a resource should further detail be desired for any of the instrumental techniques broached below.

2.1 Sample Preparation

All samples were prepared on 1×1 cm^2 silicon substrates (Microelectronics Inc., San Jose, CA). A 100 nm thick layer of titanium was electron-beam deposited onto the silicon substrates at room temperature and pressures < $1x10^{-6}$ torr. When necessary, samples were cleaned by sonicating twice for five min. in each of the following solvents: 18-Ω deionized water, dichloromethane, acetone, and methanol. Additional sonication steps and UV-ozone cleanings were also occasionally used.

2.2 Atom Transfer Radical Polymerization (ATRP)

Why ATRP?

There are multiple methods to chemically graft a polymer to a surface. The simplest of these, procedurally, is free-radical polymerization, which begins with the introduction of an unsaturated functional group to the surface.[21-23] For surfaces bearing hydroxyl groups, silane chemistry is a convenient way of achieving this.[24-26] The procedure consists of soaking a clean substrate in a silane solution for a period of time. Substrates were soaked overnight in this work, but complete surface coverage is likely achieved sooner.[26] The surface functionalization is a self-limiting reaction, and after the minimum time to achieve monolayer coverage, soaking longer does not substantially alter the silane film quality.[24, 27]

Following the silane reaction, unbound silane is cleaned from the surface, and the sample is transferred to a solution of monomer dissolved in an appropriate solvent. After adding a free-radical initiator—azobisisobutyronitrile (AIBN) being a popular choice—the mixture is heated under vacuum. Upon heating, the initiator decomposes into free-radicals that then propagate in solution in a polymer-forming chain-reaction.[22, 23] This must be done under vacuum, because oxygen scavenges free-radicals killing the polymerization reaction.[28] Grafting occurs when one of the reacting polymer strands catches a surface-bound double-bond. When run in this manner—using a solution-phase initiator—free-radical polymerization is considered a "grafting-to" reaction, since polymer strands form in solution and then graft themselves *to* the surface. Again, the advantage of free-radical polymerization is its procedural simplicity. The disadvantage is the lack of control over the reaction.[28] Polymer chains can grow to any length in solution before grafting to the surface. Or, two active polymer radicals may react together in solution, terminating the propagation of those chains.[23, 28] Both may result in patchy surface coverage if termination reactions expend a significant portion of monomer in solution, or simply if a long chain grafts to the surface and then flops over blocking unreacted double bonds (i.e., steric effects). In short, a controlled polymerization reaction is needed to create uniform grafted films.[21]

There exists a class of controlled grafting reactions known as living polymerizations. These reactions are considered "living" because they can be quenched, the samples removed from solution, re-immersed in a fresh reaction solution—even one containing a different monomer—and the polymerization will resume where it left off. Often, living polymerizations are classified as "grafting-from" reactions because, instead of growing a polymer chain in solution and then grafting it to the surface, as with free-radical grafting-to reactions, the polymer chains are grown *from* the surface one link at a time. Of the living polymerization reactions, atom transfer radical polymerization (ATRP) is among the most controlled.[21, 28]

How does ATRP work?

Procedurally, ATRP begins much like free-radical polymerization in that a functional group must be introduced onto the surface—using silane chemistry for oxide and other hydroxyl-bearing substrates, and thiol chemistry for any oxide-less metal surfaces, namely gold.[21, 29, 30] However, rather than an alkene functionality, a halide-terminated ATRP initiator is introduced.[31] This is a fundamental difference between ATRP and free-radical grafting-to reactions: ATRP

initiators are surface-bound, whereas grafting-to initiators are in the solution phase.[31] Once the surface has been successfully functionalized with the ATRP initiator, the substrate is immersed in a solution of monomer dissolved in an appropriate solvent. Next is added a solution of CuX/CuX_2, where X is a halide, and a ligand—2,2'-bipyridine (bpy) being one of the more popular choices.[28, 32] The ligand coordinates with the CuX, electronically stabilizing it so that it can remove the halide from the ATRP initiator, oxidizing the CuX to CuX_2, and generating a surface-bound radical at the end of the initiator where the halide was removed (figure 2.1, A and B).[31] However, the system is in a dynamic equilibrium that favors the singly oxidized CuX, rather than the doubly oxidized CuX_2.[28] Therefore, the radical is briefly exposed for just long enough to react with any monomer in the immediate area. In doing so the radical is transferred from the initiator to the monomer, which is then capped by the halide from the initiator as the catalyst is reduced from CuX_2 to CuX (figure 2.1, C and D).[31] This process is what provides ATRP the control over polymer chain propagation, because radicals are only generated long enough to react with one monomer chain link at a time.[21] Thus, ATRP can be used for the grafting of thick and uniform polymer films to any surface to which an initiator can be immobilized.[31]

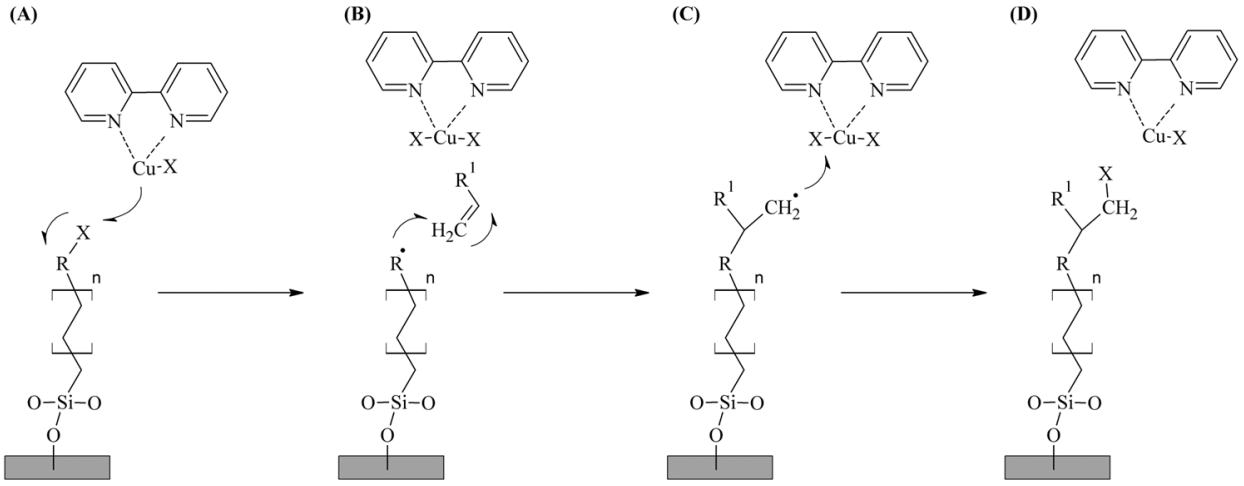

Figure 2.1. Schematic representation of a generic ATRP reaction. (A) Bpy-copper ligand removing the halide from the surface-bound ATRP initiator. (B) Exposed surface-bound radical reacting with nearby monomer. (C) Radical is propagated from the initiator to the grafted monomer. (D) Halide is transferred from the bpy-copper, which is once again reduced from CuX_2 to CuX.

What are the difficulties associated with ATRP?

The main difficulty associated with ATRP is that the CuX, which is critical to the reaction, is rapidly and permanently doubly oxidized in the presence of oxygen. Put another way, oxygen kills ATRP,[33] and must therefore be rigorously excluded from the reaction. This usually involves a complicated schlenk-line procedure that is nearly impossible to scale up, though another alternative is to run the reaction is a glove box. However, most glove boxes are designed to be not only oxygen-free, but also moisture-free, and NaSS monomer is essentially only soluble in water. Therefore, for ATRP reactions employing aqueous solvents, the use of a glove box is often not an option.

In 2007 Matyjaszewski et al.[33] found a way to circumvent the need for an oxygen-free environment. The new procedure, known as "Activators aRe continuously reGenerated by Electron Transfer" (ARGET) ATRP, calls for the addition of a reducing agent, such as vitamin C, to the reaction.[31] The reducing agent regenerates poisoned CuX, effectively scavenging dissolved oxygen. What was once a complicated schlenk-line procedure becomes as simple as mixing a few reagents together in solution, adding a reducing agent, and capping the reaction. The amount of reducing agent added must be in large excess over the amount of oxygen present. In order to minimize the amount of reducing agent required the amount of oxygen and therefore the headspace in the reaction vessel should also be minimized. There is some concern about loss of control for ARGET-ATRP vs. traditional ATRP, but Matyjaszewski et al.[33] found that polydispersitiy indices of 1.1 can be achieved by both procedures.

What is the ATRP grafting procedure?

A detailed ATRP grafting procedure is found in chapter 3. However, a brief synopsis is as follows: the first step is the surface-immobilization of an ATRP initiator. The reaction is performed in toluene, which was dried over 4A molecular sieves. Anhydrous toluene is necessary because silane chemistry is sensitive to the amount of water in solution.[26, 34, 35] The initiator is trichlorosilane/10-undecen-1-yl 2-bromo-2-methylpropionate, referred to as ClSi for brevity, the synthesis of which can be found in ref.[36] Following the ClSi functionalization, the grafting reaction is performed in 60/40 water/methanol and the reagent ratio used is 180/22/10/1 NaSS/bpy/CuBr/$CuBr_2$ (mole basis).

Optimization of the ARGET-ATRP procedure is found in chapter 4, and the end result—as used on gold substrates—is found in chapter 5. Briefly, the ClSi functionalization is identical to

that above, which, again, is suitable to any oxide or hydroxyl-bearing surface. Thiol chemistry, from a 1 mM solution of bromoisobutyrate undecyl disulfide in ethanol, is used for gold surface functionalization. The grafting-reaction solvent is again 60/40 water/methanol and reagents amounts per nominal cm^2 of functionalized surface area are: 250 mg NaSS, 0.5 mg $CuBr_2$, 1.4 mg bpy (1:2 $CuBr_2$:bpy—mole basis), and 39.5 mg vitamin C. The reactions are carried out in parafilm-sealed, 20-ml glass scintillation vials, with two 1×1 cm^2 functionalized substrates (i.e., 2-cm^2 nominal functionalized surface area) per vial. The NaSS is weighed into each individual reaction vial along with 1.2 ml 18-Ω DI H_2O. However, bulk catalyst ($CuBr_2$ and bpy) and vitamin C solutions are prepared separately to minimize weighing error. The catalyst solution is added to the reaction vial, which is often sonicated briefly to fully dissolve the NaSS. The samples are then added, taking care that they stay face up and do not overlap. Finally, the reaction commences upon addition of the vitamin C solution, which, upon addition, turns the reaction solution from light blue/green to light brown, indicating that the $CuBr_2$ has been reduced to CuBr. At this point the container is sealed to avoid introducing additional oxygen. The samples are worked up as reported in Chapters 4 and 5.

2.3 Protein adsorption

What is the motivation for studying protein adsorption?

As mentioned in chapter 1, protein adsorption begins within seconds of a surface being brought into contact with a protein solution, and continues until that surface is completely covered. And again, this phenomenon is extremely important in many biomedical applications, which is the ultimate application of this thesis.

Why does protein adsorption occur?

Surfaces are at a higher energy state than the bulk, and a rule of nature is that systems tend toward the lowest energy state possible. One way to minimize surface energy is through adsorption. Expose any surface to the ambient and within minutes it will adsorb a layer of adventitious carbon.[37, 38] This is because the adventitious carbon-contaminated surface is at the minimum energy state in ambient air. Expose any surface to an aqueous protein solution and—rather than adsorbing hydrocarbons—it will adsorb a layer of protein because, in an aqueous protein solution, the protein-covered surface is the lowest energy state.[9] Thus, surface-energy minimization is the main driving force for protein adsorption.[39, 40]

While surface energy minimization is a fine thermodynamic explanation, the exact mechanism of protein adsorption is not completely understood and likely changes for different proteins-surface combinations.[6, 11, 13, 41] It may be that proteins adsorb by first attaching multiple segments until they are unable to desorb.[12] Unlike simple polymers, proteins are composed of thousands of segments from a library of 20 different amino acids. These can be polar or non-polar, charged or neutral. Which amino acids interact with the surface and how exactly they do so is not known. What is known is that the total adsorption process is due to the sum of hydrogen bonding, electrostatic, Van der Walls, polar, and hydrophobic/hydrophilic interactions, and can also involve conformational changes after a protein adsorbs.[6, 12, 39, 41] These forces can be altered by changing surface chemistry, which leads to different proteins being adsorbed in different orientations and conformations. For example, one study showed that the orientation of a protein-G mutant—with one side enriched in negatively charged amino acids, and the other in positively charged amino acids—changed depending on whether it was adsorbed to a positively or negatively charged surface.[42, 43] Outside of such model systems, it is difficult to predict how protein adsorption might change in response to changes in surface chemistry.

What is the protein adsorption procedure?

All protein adsorption experiments are performed in a 24-well plate in a commercially available aqueous solution of sodium phosphate (0.01 M), sodium chloride (0.138 M), and potassium chloride (0.0027 M), known as phosphate buffered saline (PBS). Samples are hydrated in degassed PBS for at least 30 minutes prior to adsorption. The adsorption is typically carried out at 37 ^{o}C for two hours, although shorter times are sometimes used. Following the adsorption step, the protein solution in each well is diluted eight times with fresh PBS before removing the samples, to avoid pulling them through a layer of denatured proteins at the air-liquid interface. Following removal from the well-plate, the samples are rinsed twice in fresh PBS to remove any loosely bound protein, and then three times in 18-Ω deionized water to remove excess buffer salts. Samples are dried with a stream of nitrogen and then stored under nitrogen until analyzed, and also in between analyses.

2.4 Analysis techniques

In large part due to the fields of catalysis and microelectronics, a suite of specialized techniques has been developed, dedicated solely to studying surfaces in minute detail. Despite these advancements in surface analysis, no one particular instrument can give a complete picture

of the surface. Therefore, multiple techniques—the more, the better—must be used in conjunction with each other to form an appreciable understanding of surface phenomena such as protein adsorption.[44, 45] The main techniques used in this work are X-ray photoelectron spectroscopy (XPS), time-of-flight secondary ion mass spectrometry (ToF-SIMS, or just SIMS), and atomic force microscopy (AFM). What each of these techniques does and how they work will be the subject of the remainder of this chapter.

2.4.1 X-ray Photoelectron Spectroscopy (XPS)

Unless otherwise cited, this section is a distillation of the discussion in ref.[46]

In XPS, surfaces are irradiated with X-rays causing valence and core electrons to be emitted as photoelectrons in a phenomenon known as the photoelectron effect. The kinetic energy (KE) of these electrons can be measured with a spectrometer and related to binding energy (E_B) using the Einstein equation:

$$E_B = h\nu - KE$$

where $h\nu$ is the X-ray energy. This form of the Einstein equation is sufficient to explain the theory behind XPS, but in practice additional terms are needed to account for experimental conditions (e.g., spectrometer work function, flood gun use, etc.). Binding energy is a measure of how tightly an electron is bound to the nucleus of an atom. The strength of this interaction depends on from which orbital of which element the electron originated, and to a lesser extent the chemical environment of the atom. XPS data are presented as spectra—with intensity or counts per second (cps) on the y-axis and binding energy in electron-volts (eV) on the x-axis—composed of a series of peaks centered at different binding energies. Each peak corresponds to electrons from a particular orbital of a particular element. For example, the peak corresponding to carbon 1s electrons appears at a binding energy of 285 eV, while the oxygen 1s peak appears at 532 eV. The area under each peak is related to the amount of that particular element present on the surface. Therefore, surface compositions can be determined with XPS, as well as some information about the chemical environment of each element.

While it is true that X-rays penetrate and elicit photoelectron emission deep into the bulk of a material, XPS is considered a surface analysis technique because only electrons from approximately the uppermost 10 nm are able to escape the surface without recombining with, or losing energy due to collisions with other atoms (i.e., inelastic scattering). Thus, 10 nm is a good approximation of the XPS sampling depth for photoelectrons with kinetic energies of several

hundred to a thousand eV. A more precise definition of sampling depth is three times the inelastic mean free path (IMFP) of the photoelectron. IMFP is the thickness (d) of matter through which 63% of the traversing electrons will undergo a collision, as described by Beer's law:

$$I_k = I_o \mathrm{e}^{(-d/\lambda \cos\theta)}$$

where λ is the IMFP, θ is the emission angle measured relative to the surface normal, and I_k and I_o are the exiting and entering intensities, respectively. Based on Beer's law, sampling depth is defined as d when $I_k/I_o = 0.95$. However, this definition requires prior knowledge of the IMFP. For the range of kinetic energies of interest, IMFP increases with kinetic energy, but also depends on the density of the material through which the electron is traversing (e.g., inorganic vs. organic compounds). Equations relating IMFP to kinetic energy and material type have been empirically derived, though these provide only estimates and exact IMFP values are still a subject of debate. Nonetheless, IMFP estimates for photoelectrons of interest are all within the range of 1 – 4 nm, which puts the sampling depth at somewhere in the range of 3 – 12 nm.

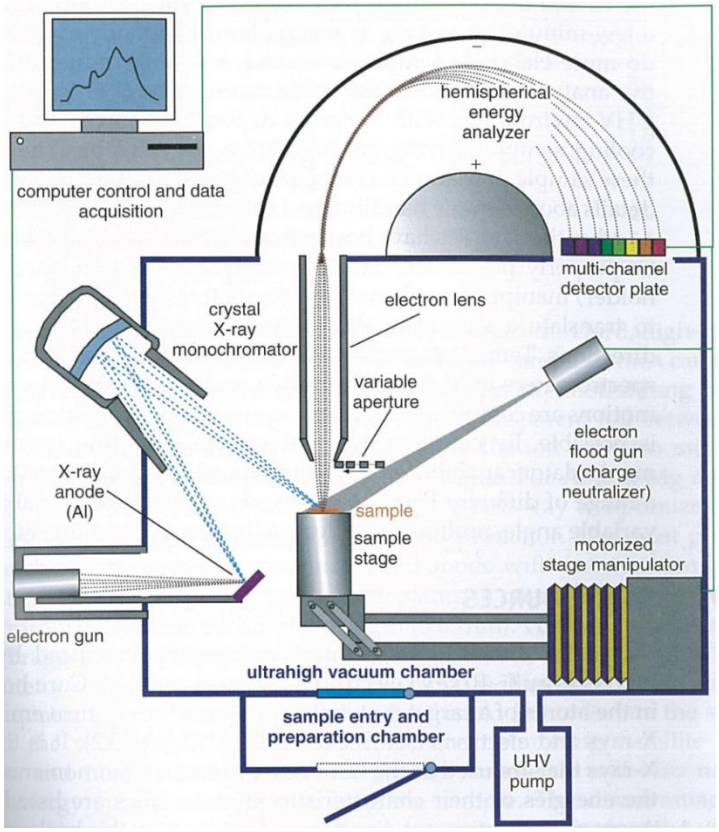

Figure 2.2. Schematic of an XPS system. Adapted with permission from ref.[46]

How does XPS work?

The X-ray source: X-ray sources are composed of an anode, usually a piece of aluminum or magnesium, irradiated by an electron gun. Electrons are generated by heating a piece of metal, usually a tungsten filament such as those found in incandescent light bulbs. Since electrons interact strongly with matter, XPS instruments—X-ray source included—are operated under ultra-high vacuum (UHV) conditions (defined as pressures < 10^{-9} torr). Different electric fields collimate the electrons into a beam and accelerate them toward the anode, where most of the energy is dissipated as heat. Therefore, anodes are usually back coated with copper and water cooled to prevent them from melting. Rather than releasing heat, some electrons excite photoelectron emission. X-ray generation occurs when an electron from a higher energy level relaxes to fill a vacancy left by photoelectron emission from a lower energy level (figure 2.3). The excess energy released by the relaxation of the higher energy electron can be dissipated in two ways: (1) emission of another electron, known as an Auger electron, after French physicist Pierre Auger; and (2) fluorescence of an X-ray photon. The probability of emitting X-rays vs. Auger electrons increases with the atomic number of the anode material. Aluminum (atomic number 13) and magnesium (atomic number 12) are used despite being relatively light elements for two reasons. First, they emit lower energy X-rays, preserving the XPS surface sensitivity. Higher energy X-rays produce higher kinetic energy electrons, which can escape from deeper within the bulk of the sample resulting in spectra that are not representative of the surface composition. Second, X-rays emitted from aluminum and magnesium have narrower line widths—that is, a narrower range of X-ray energies. The natural line widths for aluminum and magnesium are about one third of those for silver and titanium, two other commonly used anodes. Narrower X-ray line widths lead to better energy resolution, which is advantageous when doing some of the detailed analyses described below. However, even spectra from magnesium or aluminum anodes still bear improving. This brings us to the subject of X-ray monochromaters.

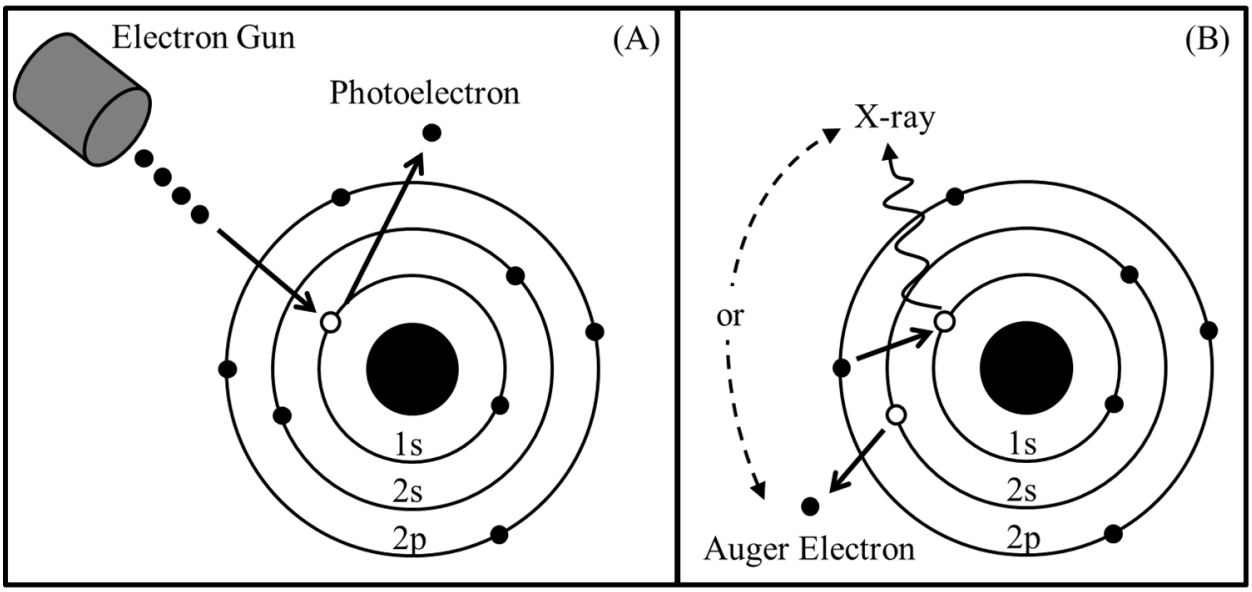

Figure 2.3. Schematic illustrating the process of X-ray generation. (A) an electron gun induces emission of a photoelectron leaving behind a vacancy in a core energy level. (Photoelectron emission can also be induced by X-rays). (B) a higher energy electron relaxes to fill the vacancy; the excess energy from this process can be released as either an X-ray or an Auger electron.

The monochromater: Monochromaters are made of one or more quartz crystals, with a natural lattice spacing such that only a narrow band of X-ray wavelengths are reflected onto the sample. These remaining wavelengths are diffracted according to Bragg's Law. To protect the sample from stray X-ray lines, sputtered material, heat, and electrons backscattered off the X-ray anode, a thin window (often a piece of aluminum foil) is placed between the anode and the monochromater. The main advantage of using a monochromater is narrower X-ray line widths leading to increased energy resolution. A disadvantage is that the line widths are decreased by cutting out a significant portion of the emitted X-rays, resulting in a lower overall signal. Also, monochromaters are expensive and increase the cost of an XPS system.

The analyzer: An analyzer collects and detects the photoelectrons ejected from the surface. Analyzers are composed of three main parts: a collection lens, an energy analyzer, and a detector. The collection lens uses electric and magnetic fields to collect electrons coming from sample and focuses them into the energy analyzer. Modern systems can collect electrons from solid angles > 20^{o}. Most lenses also reduce (or "retard") the kinetic energy of the entering

photoelectrons, so that only electrons within a certain kinetic energy range are allowed into the analyzer.

XPS systems are most commonly equipped with electrostatic hemispherical analyzers. These are made up of two concentric hemispheres with a voltage placed across them so that the outer hemisphere is negative and the inner hemisphere positive relative to the center line potential, known as the pass energy. Only electrons with kinetic energies within ± ~5% of the pass energy follow a centerline trajectory and make it through the analyzer. Electrons with kinetic energies greater than the pass energy take a larger arc and crash into the outer hemisphere. Those with kinetic energies less than the pass energy take a smaller arc crash into the inner hemisphere. The pass energy is usually fixed for a given XPS measurement, and spectra are collected by ramping the retardation energy. For example, a survey scan might begin with a retardation of 0 eV and pass energy of 100 eV. With these settings, electrons with kinetic energies from 0 – 95 eV crash into the inner hemisphere, those with kinetic energies > 105 eV crash into the outer hemisphere, and those with kinetic energies between 95 – 105 eV make it to the detector. Then imagine that the retardation energy is ramped to 10 eV, while the pass energy remains constant. Now all kinetic energies have been reduced by 10 eV so that electrons with kinetic energies < 10 eV do not enter the analyzer, those with kinetic energies between 10 – 105 eV crash into the inner hemisphere, and those with kinetic energies > 115 eV crash into the outer hemisphere. This time only electrons with kinetic energies between 105 – 115 eV are detected. This procedure is repeated to collect the entire survey spectrum in 10 eV increments. Therefore, the retardation and pass energies are a dual approach to increase energy resolution by limiting the number electrons and range of energies that reach the detector.

Photoelectrons that reach the detector pass through a number of microchannel plates (five, for the XPS used in this work) before finally hitting a position sensitive resistive anode. Microchannel plates are constructed of a highly resistive material perforated by a regular array of densely packed micron-sized channels (10 μm in diameter, 2 mm in length, and 15 μm apart, for the XPS used in this work). Each channel is a continuous-dynode electron multiplier—simply a structure that emits 1-3 electrons for every collision between an entering photoelectron and the channel wall. The walls are angled to guarantee a collision. The electrons given off will surely collide with the wall farther down the channel and in this fashion set off a chain multiplication of electrons that amplify the signal from a single incoming electron by a factor of 10^8. An electric

field applied across the microchannel plate ensures that the electrons move toward the outlet of each pore. At the end of the stack of microchannel plates, the electrons come to the position sensitive resistive anode, which measures the amplified signal. The coordinates of the electron collision on the anode are directly correlated to the kinetic energy of the original photoelectron entering the microchannel plate.

Conditions used in this dissertation

Two different XPS systems were used throughout this dissertation. The conditions for the first are as follows: XPS compositions were determined from an average of three spots on two replicate samples for each substrate. The data were acquired on a Kratos AXIS Ultra DLD instrument (Kratos, Manchester, UK) in hybrid mode using a nominal 0° photoelectron takeoff angle (TOA) and a monochromatic Al $K\alpha_{1,2}$ X-ray source $(h\nu = 1486.6 \text{ eV})$. The photoelectron TOA is defined as the angle between the surface normal and the axis of the analyzer lens. Atomic compositions were calculated from peak areas obtained from survey scans (0–1200 eV) with analyzer pass energy of 80 eV, a 1 eV step size, and a 200 ms dwell time. Carbon and sulfur chemical shifts were determined from high resolution C_{1s} and S_{2p} spectra obtained with analyzer pass energy of 20 eV, a 0.3 eV step size, and 259.7 ms and 425.5 ms dwell times for C_{1s} and S_{2p}, respectively. All samples were grounded to the spectrometer and run as conductors. Binding energy scales were calibrated by setting the CH_x peak in the C_{1s} region to 285.0 eV, and a linear background was subtracted for all peak area quantifications. The peak areas were normalized by manufacturer supplied sensitivity factors, and surface concentrations were calculated using CASA XPS (Casa Software, Ltd.).

XPS data were also collected on a Surface Science Instruments S-Probe instrument using a 55^o photoelectron takeoff angle (an analyzer upgrade changed the TOA to 0^o, though this only effects data collection starting in chapter 4) and a monochromatic Al $K\alpha_{1,2}$ X-ray source $(h\nu = 1486.6 \text{ eV})$. Atomic compositions were calculated from peak areas obtained from survey scans (0–1100 eV) with analyzer pass energy of 150 eV and a 1 eV step size. Carbon and sulfur chemical shifts were determined from high resolution C_{1s} and S_{2p} spectra obtained with analyzer pass energy of 50 eV and a 0.065 eV step size. Dwell times for all scans were 100 ms and all samples were grounded to the spectrometer and run as conductors. Binding energy scales

were calibrated by setting the CH_x peak in the C_{1s} region to 284.6 eV, and a linear background was subtracted for all peak area quantifications. The peak areas were normalized by manufacturer supplied sensitivity factors, and surface concentrations were calculated using Hawk Data Analysis 7 (Surface Physics, Inc.).

2.4.2 Time-of-Flight Secondary Ion Mass Spectrometry (ToF-SIMS)

Unless otherwise cited, this section is a distillation of the discussion in ref.[47]

In ToF-SIMS, surfaces are bombarded with a pulsed beam of either single-atom or cluster primary ions. The bombardment ejects material—single atoms, molecular fragments, and entire molecules—from the uppermost ~ 2 nm of the surface, most of which is neutral, but about 1% are ions that can be collected and manipulated with magnetic or electric fields. Identities for these secondary ions can be proposed based on their masses, which are determined by a mass analyzer, and prior knowledge of the chemical makeup of the surface. ToF-SIMS data are presented as spectra, which along with peak identification methods, are described in greater detail below.

ToF-SIMS can also be used to construct chemical maps of surfaces. The analysis area is sectioned into a square grid and a spectrum collected from each square. An image is then constructed by displaying the intensity of a given peak at each square on a color scale (figure 2.4).

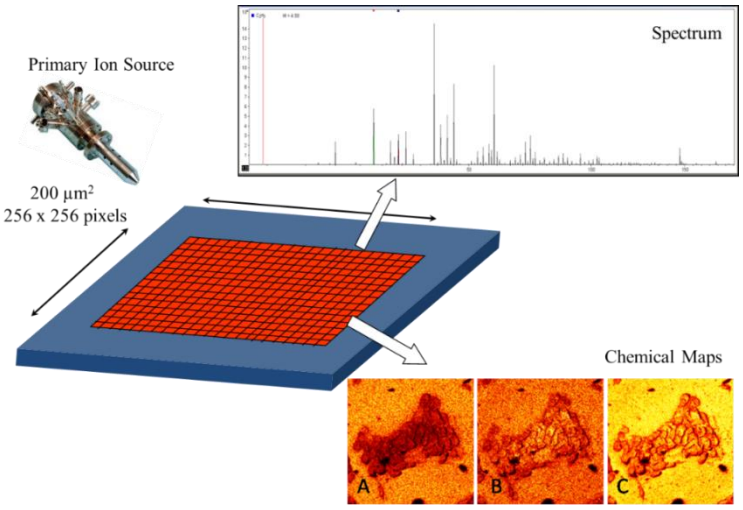

Figure 2.4. Schematic of ToF-SIMS imaging. Shown is a 200 × 200 µm^2 analysis area sectioned into a grid of 256 × 256 pixels, where a mass spectrum is collected at each pixel. Chemical maps

are constructed by displaying the intensity of a given peak at each pixel on a color scale. A, B, and C are three different chemical maps resulting from the selection of three different peaks.

How does ToF-SIMS work?

ToF-SIMS is composed of two main components: a primary ion source and a mass analyzer. **The primary ion source:** Ion sources are composed of six main parts: (1) a source region/extraction zone to create the ions; (2) focusing and collimating regions to focus the ions into a beam; (3) a mass (Wien) filter to purify the beam; (4) a pulsing mechanism for systems with time-of-flight analyzers (the importance of this is addressed later); (5) stigmation/focus lenses to reduce the beam diameter; (6) and scan rods to raster the beam across a sample. There are four main types of primary ion sources: electron bombardment, plasma, surface ionization, and field emission. Each of these sources has its own pros and cons, and each fills its own niche in SIMS research. However, since a bismuth liquid metal field ionization source was used in this work, only field ionization sources will be explained. These sources work by flowing a liquid metal over a sharp tip (radius < 1 μm). A strong electric field is applied to the tip, which shapes the liquid metal into a (Taylor's) cone, stripping electrons from and ionizing the atoms at the apex to create a plasma ball. Ions are stripped away from the plasma ball into a beam, which is collimated, purified, and focused using a combination of electric and magnetic fields. The ions stripped away from the plasma ball are a mixture of Bi_n^+ ions, where n = 1, 3, 5, etc. Both monoatomic (n = 1) and polyatomic (n = 3, 5, etc.) ion beams are used in SIMS, and the pros and cons of monoatomic vs. polyatomic ion sources are explained in a separate section below. Either way, a mass selection process is used to mass filter out all other ions except the desired one. Next, a chopper cuts the beam into 20 – 50 nanosecond-sized pulses by rapidly sweeping it over an aperture. For time-of-flight analyzers, mass resolution increases as pulse length decreases. Therefore, the beam can be bunched by applying an electric field that will speed up the ions at the back of a pulse so that they catch up with the ions at the front. Mass resolution is defined as $m/\Delta m$, where m is the mass that a given peak represents, and Δm the width of that peak. A buncher decreases pulse lengths to less than one nanosecond, significantly reducing Δm. However, this is at the cost of decreased spatial resolution since the beam diameter is increased in the bunching process. Finally, scan rods raster the beam across the desired analysis area so that each primary ion strikes a pristine spot on the surface, and also so chemical imaging experiments can be performed.

The analyzer: After a primary ion impact, the secondary ions ejected from the surface are funneled into an analyzer using an extraction field. There are multiple types of analyzers: quadrupole, magnetic sector, and time-of-flight to name a few of those more commonly used. A time-of-flight (ToF) analyzer was used in this work. In its simplest form a ToF analyzer is essentially a long tube of length L. Secondary ions from, in theory, an infinitely short primary ion pulse simultaneously enter the tube, and race toward and strike a detector at the end. Upon entering the tube, all secondary ions are accelerated to the same kinetic energy by an acceleration potential V. The time it takes to reach the detector is related to the mass-to-charge ratio (m/z) of the ion by the following equation:

$$t = L\left(\frac{m}{2zV}\right)^{\frac{1}{2}}$$

where t is the time it takes for a given secondary ion to travel from the entrance of the tube to the detector, and it is assumed that $z = \pm 1$. In reality the secondary ions will all leave the surface with slightly different kinetic energies. The energy spread at the surface is on the order of tens of eV, while the acceleration potential is on the order of a few thousand eV, which helps reduce the importance of the initial kinetic energy spread. However, this energy spread still decreases the mass resolution of the instrument, but this can be compensated for using an ion mirror, also called a reflectron. A reflectron is a series of concentric ring electrodes with increasing voltages down the flight path of the secondary ions. If two secondary ions with the same m/z ratio have slightly different kinetic energies, the higher kinetic energy ion will travel farther into the reflectron before being reflected back down the flight tube. Therefore, the higher energy ion will have a longer flight path than lower energy one and that way both ions will leave the reflectron and reach the detector at the same time. The detector is a microchannel plate similar to those used to detect electrons in hemispherical analyzers.

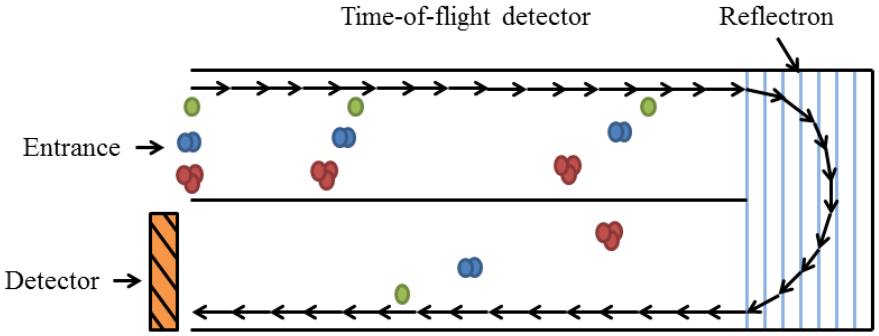

Figure 2.5. Schematic of a time-of-flight mass analyzer. Adapted from ref.[48]

Important ToF-SIMS Concepts

Billiard Ball Collision Cascade Theory: The most convenient theory for how high-energy monoatomic primary ions interact with a surface is to model all atoms as hard billiard ball-like spheres. In this model the impact a primary ion with the surface is much like breaking to begin a game of billiards: the cue ball (primary ion) collides with the first layer of billiard balls (surface atoms), setting off a cascade where each layer collides with the next. This creates a shockwave-like effect as the energy travels radially away from the impact site. The amount of energy deposited at the impact site is high enough that only atomic species are ejected. However, since the energy lessens as the shockwave propagates across the surface, larger and larger species are ejected including molecular fragments and even entire molecules. Again, only about 1% of the material ejected from the surface in a SIMS experiment will be ionized. The remaining 99% will be neutral species, which is one of the key reasons that SIMS is primarily used to qualitatively—as opposed to quantitatively—characterize surface molecular structure.

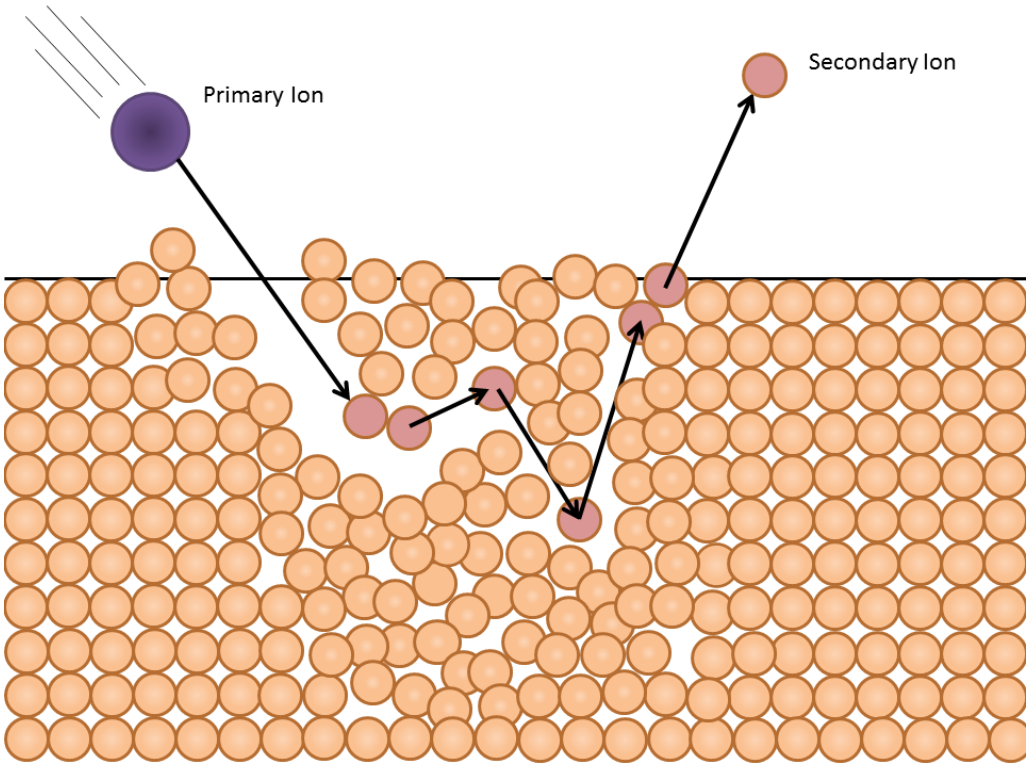

Figure 2.6. Schematic of the billiard ball collision cascade theory. A collision between a primary ion and the surface results in chemical rearrangement below the surface and ejection of a secondary ion. Adapted from ref.[48]

The Static Limit: Clearly, SIMS is a destructive technique, since it damages the sample both by removing material from the surface and rearranging material beneath it. Therefore, a legitimate concern is that multiple primary ion collisions at the same impact site will produce an erroneous picture of the molecular structure of the surface. To avoid this, SIMS experiments are typically run below the "static limit", which is defined as a primary ion dose of $< 10^{12}$ ions/cm^2. Assuming surfaces are made up of about 10^{15} atoms/cm^2, below the static limit there is less than one primary ion impact per 1000 surface atoms. This ensures that "double sampling" occurs so infrequently that the resulting spectra do in fact accurately represent the true molecular structure of the native surface.

Polyatomic Ions: Another way to minimize damage to the sample is to use polyatomic ions to reduce chemical rearrangement beneath the surface. To illustrate how this works, imagine a 30 keV bismuth ion source. Again, these sources can produce Bi_n^+ ion beams, where n = 1, 3, 5, etc. If Bi^+ is produced, then each ion has 30 keV of energy. If Bi_3^+ is produced, then the energy of each atom carries with it $30\ \text{keV} \div 3 = 10\ \text{keV}$. The higher energy Bi^+ ions implant deeper into

the sample than the Bi_3^+ ions, dispersing less energy at the surface and causing more damage below. Another advantage of polyatomic ion beams is that, because more of the energy is released at the surface, the secondary ion yields increase by 100 to 1000 times over those obtained using Bi^+. Also, since the impact is spread over a larger area, less material is atomized and more molecular fragments and whole molecules are ejected from the surface. However, at some point the energy per atom decreases beyond the optimal range and a decrease in the secondary ion yield occurs. For this work it was found that a Bi_3^+ primary ion beam provided a good balance between sufficiently high signal and production of larger secondary ions.

Analysis of ToF-SIMS Spectra

ToF-SIMS spectra are collections of hundreds to thousands of peaks spanning a mass range of $10^2 – 10^3$ amu. There are, of course, certain challenges inherent to analyzing data of such complexity. First, the identity of most of these peaks is unknown, and it is unrealistic and unnecessary, even, to identify every peak. However, without a process to objectively identify which peaks are important, it is up to the researcher to determine—blindly or based on experience—which peaks are important enough to bear identifying. In the simplest case peak identification is made by deduction. For example, a negative spectrum peak at 17.003 m/z is almost certainly OH- because O (15.999 amu) + H (1.008 amu) sum to 17.007, which is within error of the measured mass. There are also no other logical options at that mass. However, the number of possible options increases precipitously with increasing m/z, oftentimes with multiple options equally likely of being correct. In a minority of cases, published peak identities can be found in the literature. Most of the time, however, either a given level of uncertainty in the peak identity must be accepted, or further experimentation involving analysis of standards—using ToF-SIMS or other more specialized mass spectrometry techniques—is required to identify peaks at higher masses. Obviously, an objective method for determining when, and for which peaks, such efforts will be effective is important.

Another difficulty in analyzing ToF-SIMS data is identifying differences between spectra: peaks that appear in one spectrum but not another, or intensity differences of the same peak in both spectra. Considering that the average ToF-SIMS spectrum contains hundreds of peaks, comparing two spectra by eye is impractical. Again, an objective method for determining the significant peaks to compare between spectra is important.

Principal Component Analysis (PCA)

Unless otherwise cited, this section is a distillation of the discussion in ref.[49]

Principal component analysis is a complex multivariate statistical technique, the exact workings of which are outside of the scope of this document. In general terms, in the context of ToF-SIMS, PCA reduces hundreds of variables (peaks) to a handful of principal components (PCs) that capture the largest amount of variance within the data set. Put another way, PCA is a clustering algorithm, which outputs two different graphs: a scores plot and a loadings plot. Sample sets clustered closely together on a scores plot can be said to be more similar to each other than those grouped farther apart. Samples sets with overlapping 95% confidence intervals are considered indistinguishable under those particular analysis conditions. However, rerunning the analysis using a different combination of peaks and samples can yield a different outcome, and care should be taken not to over-interpret PCA results. In loadings plots, peaks are plotted against their loading value. Peaks with positive loading values correspond to samples with positive score values, and vice versa for negative scores and loadings. For example, the samples with negative scores in figure 2.7 correspond with the negative loading sulfur-containing peaks. The samples with positive scores correspond with the positive loading silicon-containing peaks. From these plots it can be concluded that the negatively loading samples contain more sulfur, whereas the positively loading samples are rich in silicon. Furthermore, those peaks with the highest loadings are those influencing the analysis the most. Therefore, PCA is an objective method to both determine which peaks are important and worth identifying, and to highlight the differences between sample sets and which peaks account for those differences.

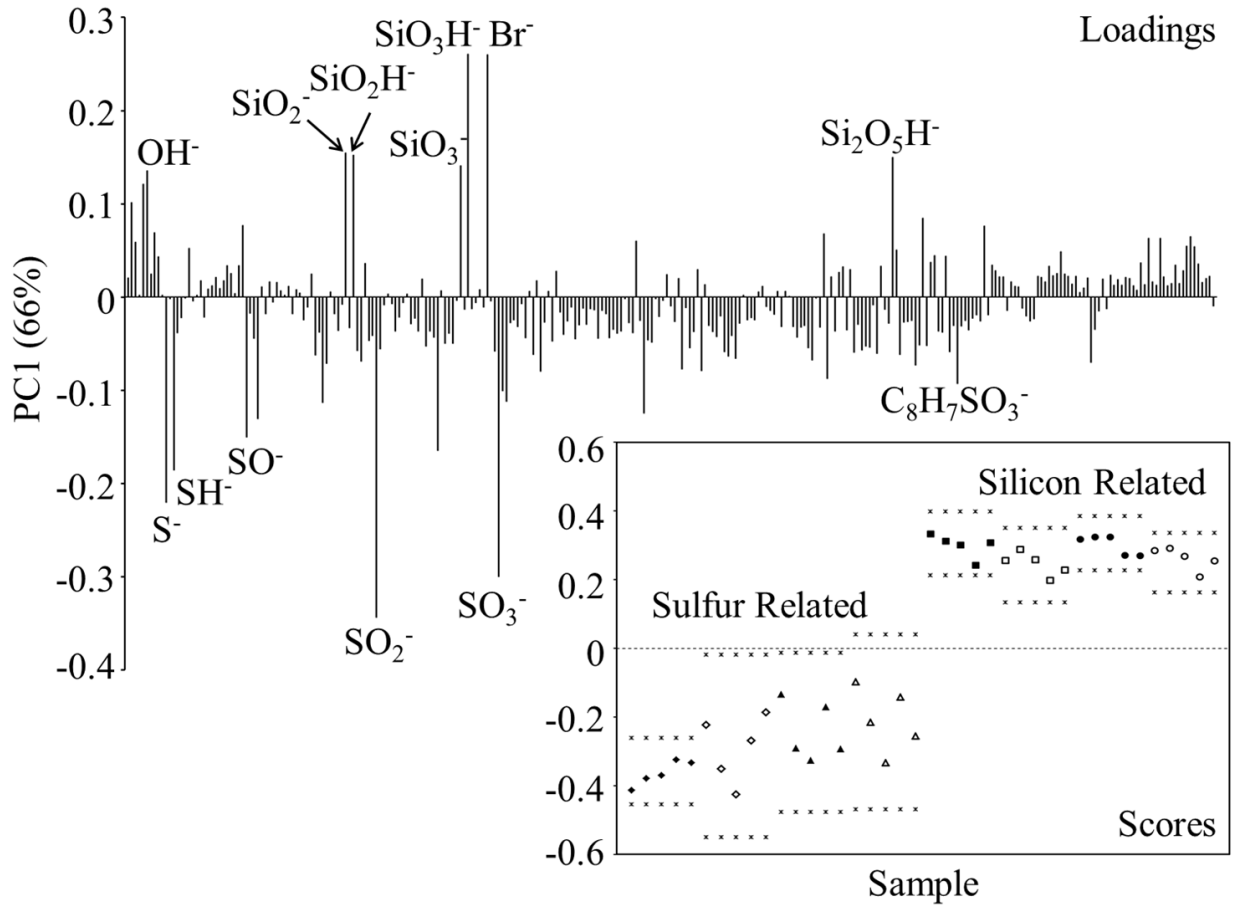

Figure 2.7. Example loadings plot and inset scores plot. Samples with negative score values correlate with the negative loading sulfur peaks; samples with positive score values correlate with the positive loading silicon peaks. Adapted from ref.[50]

2.4.3 Atomic Force Microscopy (AFM)

Unless otherwise cited, this section is a distillation of the discussion in ref.[51]

AFM is capable imaging the topography of a surface from the micron scale down to the nanometer or, in special cases, even atomic scale. It does so by raster scanning a very fine tip at the end of a cantilever across a surface with a constant set point. The choice of set point depends on the imaging mode, as explained further below. A feedback loop raises or lowers the tip as necessary to keep the set point constant. This is done with a piezoelectric crystal, which is capable of making very fine predefined movements as a response to voltage changes applied across the crystal.

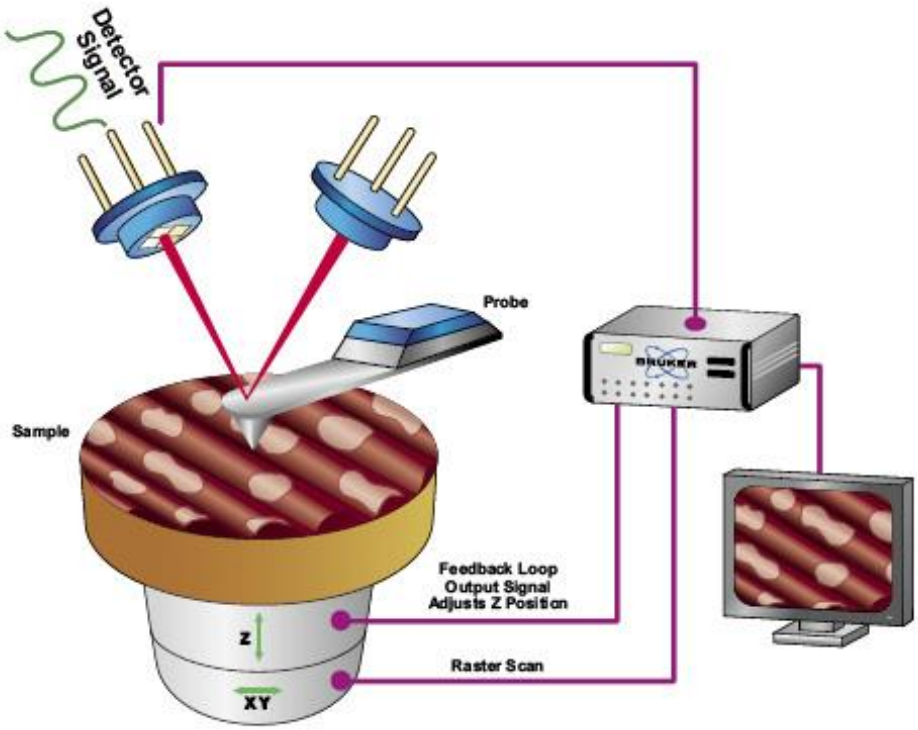

Figure 2.8. Schematic of the necessary components comprising an AFM.[52]

AFM Imaging Modes

There are a variety of AFM imaging modes, the two most common being contact mode and tapping mode. In contact mode, the tip is in constant contact with the surface, and the set point is the deflection of the cantilever, which is directly related to the force between the tip and the surface. Cantilever deflection is measured by reflecting a laser off the back of the cantilever onto a photodetector. While contact mode was the original mode of operation used in AFM, the high shear forces applied by the tip can lead to sample damage and distortion of topography features when imaging soft samples. Sample damage is something to be avoided the majority of the time, but it can be taken advantage of when performing so-called "scratch tests" to measure polymer film thicknesses. Scratch tests consist of using a high deflection set point and smaller scan size to scratch a hole in the film. The deflection set point is then reduced and the scan size increased to measure the depth of the hole. This procedure is iterated until the depth of the hole remains unchanged between two successive iterations.

In tapping mode—which was developed as a way to reduce the high forces experienced in contact mode—the cantilever is driven at its resonant frequency causing it to oscillate. The tip

contacts the surface at the bottom of each oscillation cycle as the cantilever completes its arc. For the stiff silicon cantilevers typically used in tapping mode experiments ($k \sim 40$ N m^{-1}, $f_o = 300$ kHz), this means that the tip "taps" the surface 10^5 times per second as the whole cantilever/tip assembly is raster scanned across the surface.

Image Processing

Piezoelectric crystals reversibly change shape in response to a change in voltage, which is a convenient method for making very small controlled movements with the AFM cantilever/tip assembly (both laterally and vertically). However, the response between the physical deformation and voltage changes is nonlinear, which introduces a number of so-called scanner artifacts into the AFM images. Scanner artifacts appear as artificial tilting or bowing of the image, and can be removed by using either line or plane flattening. In line flattening, each line in the image is fit to a 0^{th}, 1^{st}, 2^{nd},…, n^{th}-order polynomial. These polynomials are then subtracted from each line to flatten the image. Similarly, in plane flattening the AFM data is fit with a two-dimensional plane polynomial (in both x and y), which is then subtracted from the whole image at once.

3. Surface Initiated ATRP Grafting of Sodium Styrene Sulfonate from Titanium and Silicon Substrates

Rami N. Foster

Department of Chemical Engineering, University of Washington – Seattle, and National ESCA and Surface Analysis Center for Biomedical Problems, Seattle, Washington 98195

Andrew J. Keefe, Shaoyi Jiang

Department of Chemical Engineering, University of Washington – Seattle, Seattle, Washington 98195

David G. Castner[a)]

Departments of Chemical Engineering and Bioengineering, University of Washington – Seattle, and National ESCA and Surface Analysis Center for Biomedical Problems, Seattle, Washington 98195

[a)]Electronic mail: castner@uw.edu

3.1 Abstract

This study investigates the grafting of poly-sodium styrene sulfonate (pNaSS) from trichlorosilane/10-undecen-1-yl 2-bromo-2-methylpropionate (ClSi) functionalized Si and Ti substrates by atom transfer radical polymerization (ATRP). The composition, molecular structure, thickness, and topography of the grafted pNaSS films were characterized with x-ray photoelectron spectroscopy (XPS), time-of-flight secondary ion mass spectrometry (ToF-SIMS), variable angle spectroscopic ellipsometry (VASE), and atomic force microscopy (AFM), respectively. XPS and ToF-SIMS results were consistent with the successful grafting of a thick and uniform pNaSS film on both substrates. VASE and AFM scratch tests showed the films were between 25 – 49 nm thick on Si, and between 13 – 35 nm thick on Ti. AFM determined root-mean-square roughness values were ~ 2 nm on both Si and Ti substrates. Therefore, ATRP grafting is capable of producing relatively smooth, thick, and chemically homogeneous pNaSS films on Si and Ti substrates. These films will be used in subsequent studies to test the hypothesis that pNaSS-grafted Ti implants preferentially adsorb certain plasma proteins in an orientation and conformation that modulates the foreign body response and promotes formation of new bone.

3.2 Introduction

Titanium and its alloys are widely used in biomedical implants due to their optimal mechanical properties and relative bio-inertness.[53, 54] However, Ti implants are prone to failure due to the foreign body response, which is a cascade of events beginning with non-specific protein adsorption onto the implant surface, and ending with envelopment of the implant within a fibrous capsule.[11, 53] The fibrous encapsulation is hypothesized to prevent osseointegration, by inhibiting intimate bone-implant contact, leading to implant failure. A number of surface treatments have been developed to increase Ti-implant osseointegration. (Readers are referred to the reviews in references[55, 56] for further insight into the surface modification of Ti implants.) However, the surface treatment most relevant to the current study is surface modification with bioactive polymers.

Increased proliferation and adhesion of fibroblasts,[14] MG63 osteoblast-like cells,[15-17] and human mandibular osteoblasts[18] has been shown *in vitro* on sodium styrene sulfonate (NaSS) modified Ti and poly(ethylene terephthalate) (PET) surfaces. Promising results have also been obtained *in vivo* for the same surfaces.[18-20] Since the foreign body response begins with non-

specific protein adsorption, and cell function on surfaces is mediated by adsorbed proteins,[11] poly(NaSS) (pNaSS) grafted implants are hypothesized to preferentially adsorb certain plasma proteins in an orientation and conformation that modulates the foreign body response and promotes formation of new bone. Our ultimate goal is to test this hypothesis.

Two general grafting methods for NaSS surface modification were employed in previous studies on Ti surfaces: (1) surface-initiated radical polymerization from titanium peroxide groups obtained by chemical oxidation of the Ti;[16, 17, 20] and (2) solution-initiated free-radical polymerization onto 3-methacryloxypropyltrimethoxysilane (MPS) functionalized Ti.[15, 57] While these grafting methods produced films that successfully demonstrated the beneficial effects of grafted NaSS, they do not allow the control of the grafted polymers in terms of chain length uniformity, thickness, etc. that can be obtained from atom transfer radical polymerization (ATRP). The substrates grafted via free-radical polymerization are suitable for cell-based *in vitro* and *in vivo* investigations, but to analyze the shape and size of adsorbed proteins with techniques such as atomic force microscopy, smooth and chemically uniform substrates are required.

ATRP is a living polymerization method known for producing low polydispersity polymer chains $(M_w/M_n < 1.3)$ in solution, which translates to uniform films when grafted from a surface.[21, 28] ATRP is relatively versatile and has been applied with a wide variety of monomers.[21, 28, 31, 58] When coupled with a material-specific strategy for surface immobilization of the ATRP initiator, ATRP can be applied to a wide range of surfaces. As a case-in-point, using a variety of immobilization strategies ATRP has been used to graft NaSS from: reduced $\mathrm{Si(100)}$,[59-61] plasma-treated poly(tetrafluoroethylene)[62-64] and poly(vinylidene fluoride),[65] carbon black,[66] multi-walled carbon nanotubes,[67] $\mathrm{Fe_3O_4}$ [68, 69] and $\mathrm{SiO_2}$ [70, 71] nanoparticles, Ludox CL silica sols,[72] and gold.[73] Therefore, in this study we used ATRP to graft NaSS from trichlorosilane/10-undecen-1-yl 2-bromo-2-methylpropionate (henceforth referred to as ClSi) functionalized 1×1 cm^2 diced Si wafers and 1×1 cm^2 diced Si coated with ~100 nm of electron-beam deposited Ti (Fig. 3.1). Since the surfaces of polished Si wafers are very uniform, both chemically and topographically (typical RMS roughness values are ca. 0.1 nm), the diced Si substrates are used to examine pNaSS film uniformity. The Ti-coated substrates are used to examine the suitability of the ATRP method for grafting NaSS from the surface of Ti implants. To our knowledge, this is the first such study to use ATRP to graft NaSS from Ti, and also the

first such study to investigate the role of substrate effects on the uniformity of NaSS films grown via ATRP. The composition, molecular structure, thickness, and topography of the grafted pNaSS films were characterized with x-ray photoelectron spectroscopy (XPS), time-of-flight secondary ion mass spectrometry (ToF-SIMS), variable angle spectroscopic ellipsometry (VASE), and atomic force microscopy (AFM), respectively.

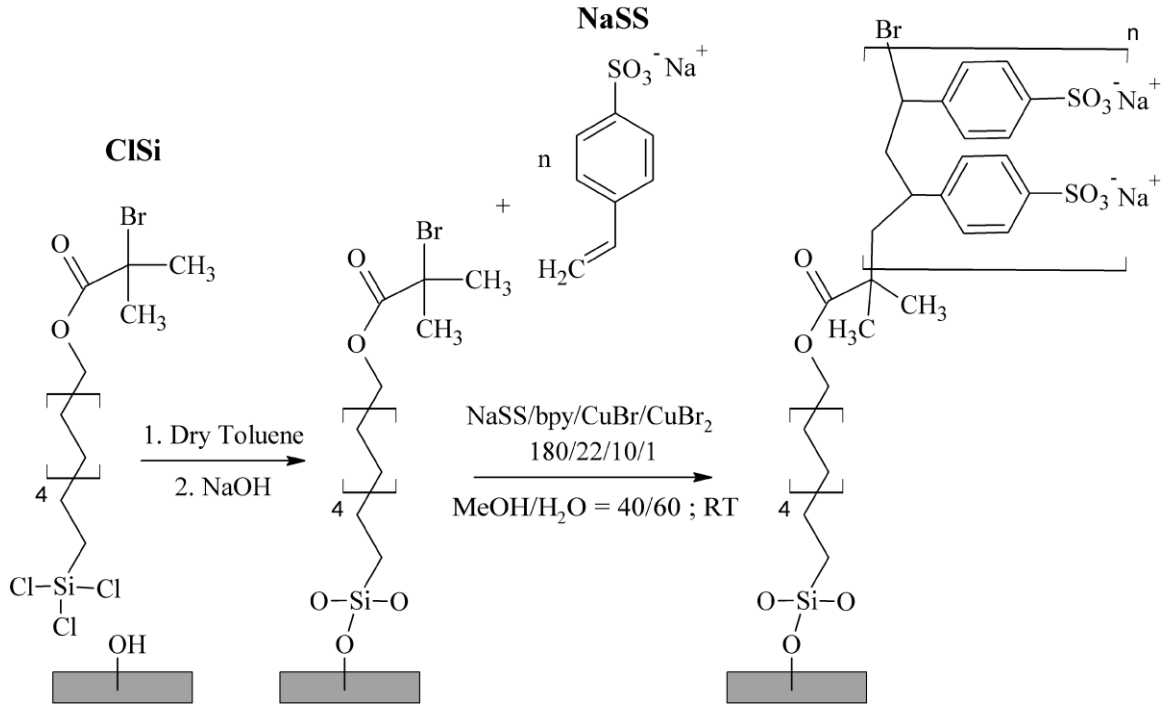

Figure 3.1. Schematic representation of the two-step NaSS grafting procedure: step 1 – surface immobilization of the ATRP initiator via ClSi functionalization of the substrate; step 2 – ATRP grafting of NaSS.

3.3 Experimental

3.3.1 Materials

Si wafers (Silicon Valley Microelectronics Inc., San Jose, CA) were diced into 1×1 cm^2 substrates using a diamond saw. Ti substrates were fabricated by depositing 100 nm of Ti onto the diced Si substrates via e-beam deposition at RT and pressures < $1x10^{-6}$ torr. Methanol, acetone, dichloromethane, toluene, phosphate buffered saline (PBS; 0.01 M phosphate, 0.138 M sodium chloride, 0.0027 M potassium chloride, pH 7.4), Cu(I) bromide (99.999%), Cu(II) bromide (>99.0%), 2,2'-bipyridine (bpy), and NaSS were all purchased from Sigma. The toluene

was dried by storing over 4A molecular sieves, the rest of the chemicals were used as received. The synthesis of the ATRP initiator, trichlorosilane/10-undecen-1-yl 2-bromo-2-methylpropionate (ClSi), has been described previously.[36]

3.3.2 Substrate cleaning and ATRP-initiator functionalization

Substrates were cleaned by sonicating twice for five min. in each of the following solvents: dichloromethane, acetone, and MeOH. This cleaning was performed prior to the Ti e-beam deposition, and again prior to the ClSi functionalization. After a subsequent 15-min. UV-ozone step, the cleaned substrates were functionalized overnight at RT in a 0.2 vol% solution of ClSi in dry toluene. The ClSi functionalization and ATRP steps were performed in glass test tubes with two substrates, one Si and one Ti, placed back-to-back in each tube. Functionalized substrates were rinsed in dry toluene followed by MeOH, and then briefly dipped in 1 mM $NaOH$ ($pH = 11$) to cross-link the surface silanes and neutralize the HCl byproducts.

3.3.3 ATRP

ATRP catalyst solids, $Cu(I)Br$ (6.42 mg, 4.48 µmol), $Cu(II)Br_2$ (1 mg, 44.8 µmol), and bpy (15.4 mg, 98.6 µmol), were weighed and sealed in a glass test tube. ClSi-functionalized substrates were sealed in glass test tubes with NaSS monomer (203 mg, 98.6 mmol). All sealed tubes were cyclically evacuated and N_2-backfilled to purge all oxygen. Meanwhile, the reaction solvents, 18-Ω DI H_2O and MeOH, were deoxygenated by bubbling N_2 through them for at least 30 min. The ATRP catalyst solids were dissolved in 2 ml MeOH. The NaSS monomer was dissolved in 1 ml MeOH and then 1.5 ml of 18-Ω DI H_2O was added to achieve a 60/40 $H_2O/MeOH$ ratio. Each reaction was started by adding 90 µL of ATRP catalyst solution to a test tube containing the NaSS monomer plus the functionalized substrates. All reactions were shaken, not stirred, and allowed to proceed to completion for ca. 72 hrs, after which the substrates were rinsed with 18-Ω DI H_2O and soaked in PBS overnight to remove any residual Cu catalyst and monomer. Finally, the grafted substrates were rinsed again with 18-Ω DI H_2O, gently dried with a stream of N_2, and stored under N_2 overnight before XPS analysis. All analyses were performed on the same set of samples in the following order: XPS, ToF-SIMS,

AFM, VASE. Two replicate samples for each substrate were prepared and analyzed for each treatment.

3.3.4 XPS

XPS compositions were determined from an average of three spots on two replicate samples for each substrate. The data were acquired on a Kratos AXIS Ultra DLD instrument (Kratos, Manchester, UK) in the hybrid mode using a nominal 0° photoelectron takeoff angle (TOA) and a monochromatic Al $K\alpha_{1,2}$ X-ray source $(h\nu = 1486.6\ \text{eV})$. Here, the photoelectron TOA is defined as the angle between the surface normal and the axis of the analyzer lens. Atomic compositions were calculated from peak areas obtained from survey scans (0–1200 eV) with analyzer pass energy of 80 eV, a 1 eV step size, and a 200 ms dwell time. Carbon and sulfur chemical shifts were determined from high resolution C_{1s} and S_{2p} spectra obtained with analyzer pass energy of 20 eV, a 0.3 eV step size, and 259.7 ms and 425.5 ms dwell times for C_{1s} and S_{2p}, respectively. All samples were grounded to the spectrometer and run as conductors. Binding energy scales were calibrated by setting the CH_x peak in the C_{1s} region to 285.0 eV, and a linear background was subtracted for all peak area quantifications. The peak areas were normalized by the manufacturer supplied sensitivity factors, and surface concentrations were calculated using CASA XPS (Casa Software, Ltd.).

3.3.5 ToF-SIMS

Positive and negative secondary ion spectra and images were acquired on a TOF.SIMS 5-100 instrument (ION-TOF, Münster, Germany) using a pulsed 25 keV Bi_3^+ primary ion beam under static conditions (primary ion dose < 10^{12} ions/cm^2). Five spectra were collected from 100 × 100 μm^2 regions for each sample at both polarities, and at least one image was acquired from 500 × 500 μm^2 regions for each sample at both polarities. Spectra were acquired in high-current bunch (high mass resolution) mode, and images in burst alignment (high spatial resolution) mode. Secondary ions were collected over a range of 0–800 m/z at a mass resolution $(m/\Delta m)$, in high-current bunch mode, between 4000 and 8000. Positive spectra were mass calibrated using CH_3^+, $C_2H_3^+$, and $C_3H_5^+$ peaks, and negative spectra were calibrating using CH^-, OH^-, C_2H^-, C_3^-, C_4H^-, and C_5^- peaks. Mass calibration corrections were typically below 20 ppm.

3.3.6 Principal Component Analysis (PCA)

PCA of the ToF-SIMS data, previously described in detail,[74-76] is a multivariate analysis technique that was used to identify principal sources of variation between sample spectra. For both positive and negative spectra, lists of all significant peaks – defined as any peak with intensity three times the background noise – were compiled and imported into a series of scripts written by NESAC/BIO for MATLAB[77, 78] (MathWorks, Inc., Natick, MA). Contaminant peaks (e.g., poly(dimethyl siloxane) peaks) were removed from the peak lists prior to PCA analysis. Data sets were also normalized by the sum of selected peaks, mean centered, and square-root transformed to ensure that variance within the data set was due to differences in sample variances rather than in sample means.

3.3.7 VASE

VASE measurements were made using an M-2000 ellipsometer (J.A. Woolam, Lincoln, NE). On one spot per sample, spectra were collected at three different angles (55^o, 65^o, and 75^o) in a spectral range from 210 – 1700 nm. These data were used to develop the ellipsometric angle models. Following these single-spot measurements, sample mapping measurements were performed on a grid of 25 spots evenly spaced 0.1 cm apart in a 0.5×0.5 cm^2 area. The mapping measurements were performed at a single angle of 65^o using a focused spot size of ~ 150 µm. Modeling was performed with the CompleteEASE software package provided by the manufacturer. The accuracy of the model fits was evaluated based on a χ^2 figure of merit as well as physical relevance of the refractive index and extinction coefficient plots generated by the model.

3.3.8 AFM

AFM images were acquired on a Dimension Icon (Bruker, Santa Barbara, CA) in TappingMode™ using OTESPA rectangular cantilevers (k = 40 N/m; Bruker, Santa Barbara, CA). One 1-µm scan, and one larger-area scan, was collected at five different spots per sample. Images were line and plane flattened as necessary the using the NanoScope Analysis software package.

Scratch test measurements were also performed to verify the accuracy of the ellipsometry models. These consisted of using a high deflection set point in contact mode to scratch a 5×5 μm^2 hole in the pNaSS film, reducing the deflection set point and increasing the scan size to 20×20 μm^2 to determine the depth of the scratched hole. This procedure was iterated, each time

scratching with a high deflection set point until the thickness remained constant between iterations.

3.4 Results and Discussion

3.4.1 NaSS Grafting Conditions

A preliminary set of experiments was performed to optimize the NaSS grafting conditions. A series of reactions was performed on e-beam deposited Ti under conditions nearly identical to those reported above, except that a 50/50 $H_2O/MeOH$ ratio was used. Initial conditions were adapted from the work of Choi and Kim on solution-phase ATRP of NaSS.[79] The reactions were followed with XPS and three spots were analyzed on two samples at each time point (2, 8, and 72 hrs).

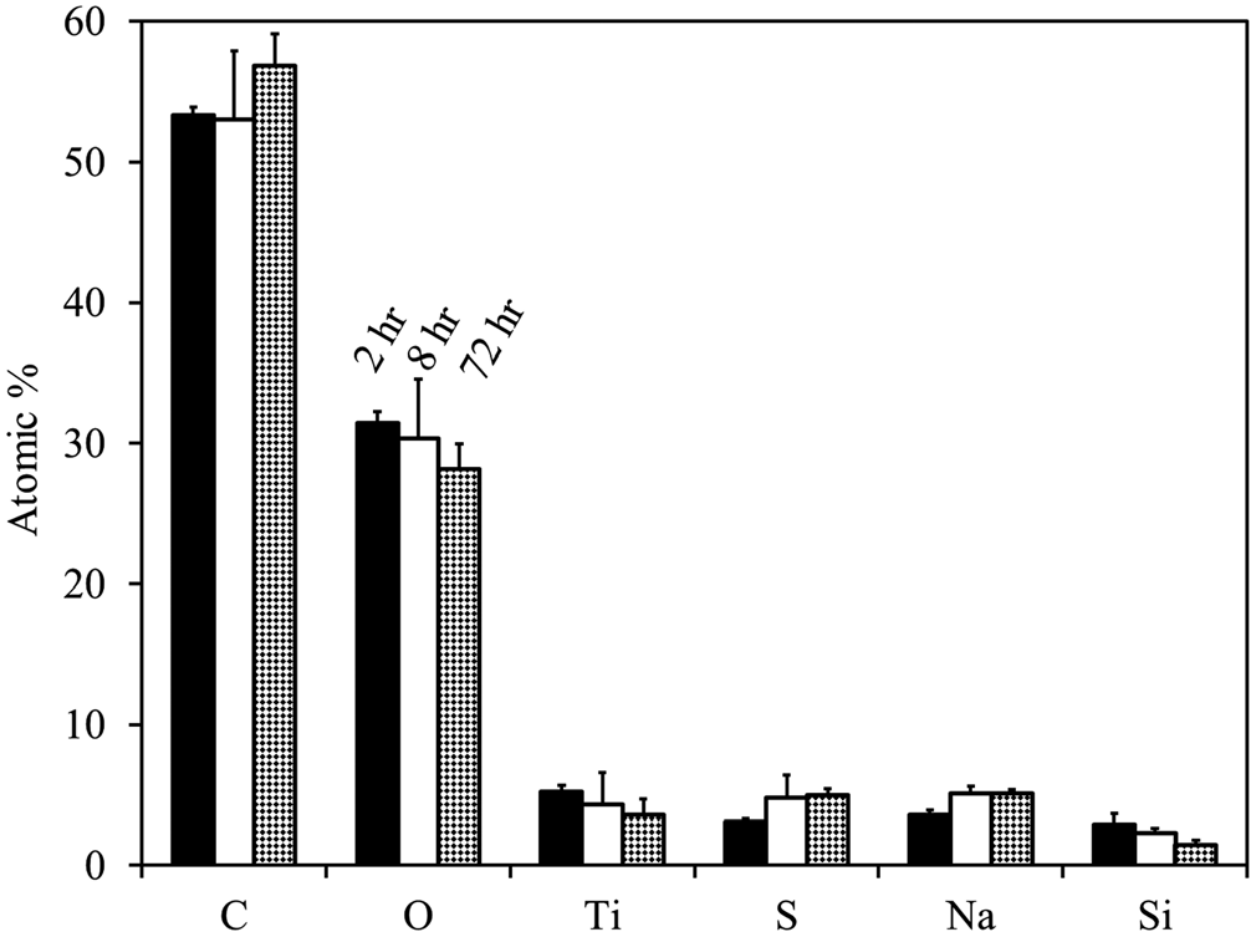

Figure 3.2. XPS compositions for a preliminary time-dependent study. Reactions were performed solely on Ti substrates under identical conditions to those described in the

experimental section, except that a 50/50 $H_2O/MeOH$ ratio was used. Compositions are reported as the avg $\pm$ stdev of three spots on two samples.

The survey composition results (Fig. 3.2) show decreasing Ti, O, and Si content with increasing reaction time. This is due to the attenuation of the substrate signal by an increasingly thick pNaSS film, and is accompanied by the expected corresponding increase in C, S, and Na content. Of note is the significant Ti content observed even after 72 hrs reaction time, which suggests that the pNaSS films are either patchy or thinner than the ~ 10 nm XPS sampling depth. Accompanying ToF-SIMS imaging and AFM measurements (not shown) were indicative of uniform and continuous films, indicating the films were <10 nm thick. Increasing solvent water content has been shown to increase reaction kinetics and final film thickness, but at the cost of decreased mono-dispersity.[79, 80] Therefore, the $H_2O/MeOH$ was increased slightly to 60/40 to graft thicker films, while maintaining good pNaSS-film uniformity.

It should be noted that, within error, S and Na content does not change between pNaSS films grown for 8 and 72 hrs at 50/50 $H_2O/MeOH$. This indicates that the reaction has essentially gone to completion after ca. 8 hrs. Increasing water content increases reaction kinetics, thus the reactions run at 60/40 $H_2O/MeOH$ have likely gone to completion in <8 hrs. And since reaction kinetics were not a main focus of this study, it was only out of convenience that the reactions were allowed to run for ~72 hrs (i.e., over the weekend). Therefore, the long reaction times reported in this paper should not be interpreted as a measure of NaSS grafting kinetics.

3.4.2 XPS Survey and High Resolution Spectra

XPS survey composition results (Table 3.1) show the bare substrates to be composed of Ti, Si, O, and C from a thin adventitious hydrocarbon overlayer. The bare substrate high resolution C_{1s} spectra show a hydrocarbon peak at 285 eV, with a slight shoulder at 286.7 eV, and a small peak at 288.7 eV (not shown). Following ClSi functionalization, the addition of Br and Si are observed for the Ti substrates, and the addition of Br is observed for the Si substrates. Furthermore, the ClSi high resolution C_{1s} spectra (Fig. 3.3 A and C) show well-defined hydrocarbon (C-C/C-H), ether (C-O), and ester (O-C=O) peaks at 285, 286.8 and 289.3 eV, respectively. However, the ether:ester peak area ratios are consistently ~2.5:1, where the ClSi

stoichiometry would predict a ratio of 1:1. This is partially due to the contribution of an overlapping C-Br peak to the ether peak. While the C-Br chemical shift is only ~ 0.8 eV, the C-Br carbon is also β-shifted ~ 0.8 eV by the ester group[81, 82] Adding the two chemical shifts as a rough approximation places the C-Br peak at ~ 286.6 eV, which overlaps with the ether peak. Lacking the energy resolution distinguish the two peaks from each other, the C-Br peak is detected by the added contribution to the ether peak area. This results in an expected 2:1 (ether + C-Br):ester peak area ratio, which is similar to the observed peak area ratio. The addition of the Br and Si in the survey spectra, and well-defined ether and ester peaks in the high resolution C_{1s} spectra are consistent with the successful ClSi functionalization of both Ti and Si substrates.

Table 3.1. XPS determined elemental compositions of bare, ClSi-modified, and pNaSS-grafted Ti and Si substrates. AFM RMS roughness values for each sample are also listed. All composition and roughness values are reported as the avg $\pm$ stdev of three spots on two samples.

XPS Atomic %						
	Evaporated Ti			Diced Si		
	Bare Substrate	ClSi Modified	pNaSS Grafted	Bare Substrate	ClSi Modified	pNaSS Grafted
O_{1s}	54.2 ± 0.5	37.6 ± 1.0	22.5 ± 1.2	34.8 ± 0.7	25.5 ± 0.6	22.6 ± 0.6
C_{1s}	23.3 ± 0.4	44.3 ± 2.1	63.2 ± 1.2	12.6 ± 0.9	41.8 ± 2.3	64.0 ± 0.6
Ti_{2p}	22.4 ± 0.2	13.2 ± 0.5	0.3 ± 0.2	-	-	-
Si_{2p}	-	3.3 ± 1.0	1.3 ± 1.4	52.6 ± 1.3	29.5 ± 1.7	2.0 ± 0.6
Br_{3d}	-	1.5 ± 0.2	-	-	3.2 ± 1.3	-
S_{2p}	-	-	6.3 ± 0.5	-	-	5.8 ± 0.3
Na_{1s}	-	-	6.4 ± 0.4	-	-	5.6 ± 0.7
AFM RMS Roughness	2.2 ± 0.2	2.1 ± 0.3	2.4 ± 0.7	0.2 ± 0.01	0.8 ± 0.2	1.9 ± 0.9

The ClSi layer thickness can be calculated from the attenuation of the substrate peaks between the bare and ClSi-functionalized substrates using:

$$I = I_o \exp\left(\frac{-d}{\lambda \cos\theta}\right) \qquad (1)$$

where d is the overlayer thickness, θ the photoemission angle relative to the surface normal, λ the inelastic mean free path (IMFP), and I and I_o the attenuated and bare substrate intensities, respectively. In nearly all cases, before Eq. (1) can be used bare substrate intensities must be corrected for the attenuation caused by the presence of an adventitious hydrocarbon overlayer.[38] This can be done using the method of Smith.[38] First the thickness of the adventitious hydrocarbon overlayer must be determined using:

$$d = -\lambda_{C1s,C} \cos\theta \ln(1 - x/100) \qquad (2)$$

where x is the hydrocarbon atom%, $\lambda_{C1s,C}$ is the effective attenuation length for C_{1s} photoelectrons traveling through the hydrocarbon overlayer (taken to be 3.5 nm), and θ is the photoelectron emission angle relative to the surface normal. Next, the substrate composition may be estimated without the effect of the hydrocarbon overlayer using:[38]

$$I_{corr} = I_{meas} \exp\left(\frac{d}{\lambda \cos\theta}\right) \qquad (3)$$

where I_{meas} is the measured atom% with the overlayer, d the overlayer thickness calculated with Eq. (2), and λ the effective attenuation length for the element and line of interest through the hydrocarbon overlayer. The corrected atom%, I_{corr}, is found for each element except carbon and must be renormalized to 100% to estimate the bare substrate composition without the hydrocarbon overlayer. For inorganic compounds, excited with an Al Kα source in the kinetic energy (E) range between 400 – 1500 eV, λ may be calculated using:[43]

$$\lambda = 0.0129E^{0.7193} \qquad (4)$$

With this method, assuming an effective photoelectron TOA of 40° for the spectrometer operated in hybrid mode,[83] thicknesses of 1.0 ± 0.1 nm and 0.9 ± 0.1 nm were calculated for ClSi films on Ti and Si, respectively.

Following the ATRP surface grafting, equal amounts of S and Na are observed in the survey spectra, as well as the disappearance of Br and near complete attenuation of the substrate peaks. The equal amounts of S and Na are in accordance with the stoichiometry expected from the NaSS monomer, and the disappearance of the Br and attenuation of the substrate peaks are indicative of the successful grafting of a ≥ 10 nm thick layer of pNaSS on both Si and Ti substrates. This is supported by the high resolution S_{2p} spectra (Fig. 3 E and F), which show the $S_{2p3/2}$ and $S_{2p1/2}$ doublet peaks in the expected 2:1 ratio appearing at ~ 168 eV, which is the expected binding energy for a $PhSO_3Na$ sulfur species.[84] Furthermore, the high resolution C_{1s} spectra (Fig. 3 B and D) are marked by the disappearance of the ester peak, as well as the addition of a shake-up peak at ~ 291.7 eV characteristic of the aromatic ring[85] present in the NaSS monomer structure. It should be noted that on the Ti samples, the Ti substrate signal is attenuated to a much greater extent (13.2 ± 0.5 At% to 0.3 ± 0.2 At% before and after NaSS grafting) than the Si signal (3.3 ± 1.0 At% to 1.3 ± 1.4 At% before and after NaSS grafting). This is due to the contribution of low levels of PDMS contamination on the Ti samples. The PDMS was detected by the presence of characteristic peaks at nominal m/z of 73 $((CH_3)_3Si^+)$, 147 $((CH_3)_5Si_2O^+)$, and 207 $((CH_3)_6Si_3O_3^+)$ in the positive ToF-SIMS spectra. No PDMS peaks were found in the negative spectra, and those found in the positive spectra were isolated to one set of Ti and Si replicates, both of which originated from the same reaction tube. As best as could be determined, no other ClSi or NaSS samples appeared to be contaminated.

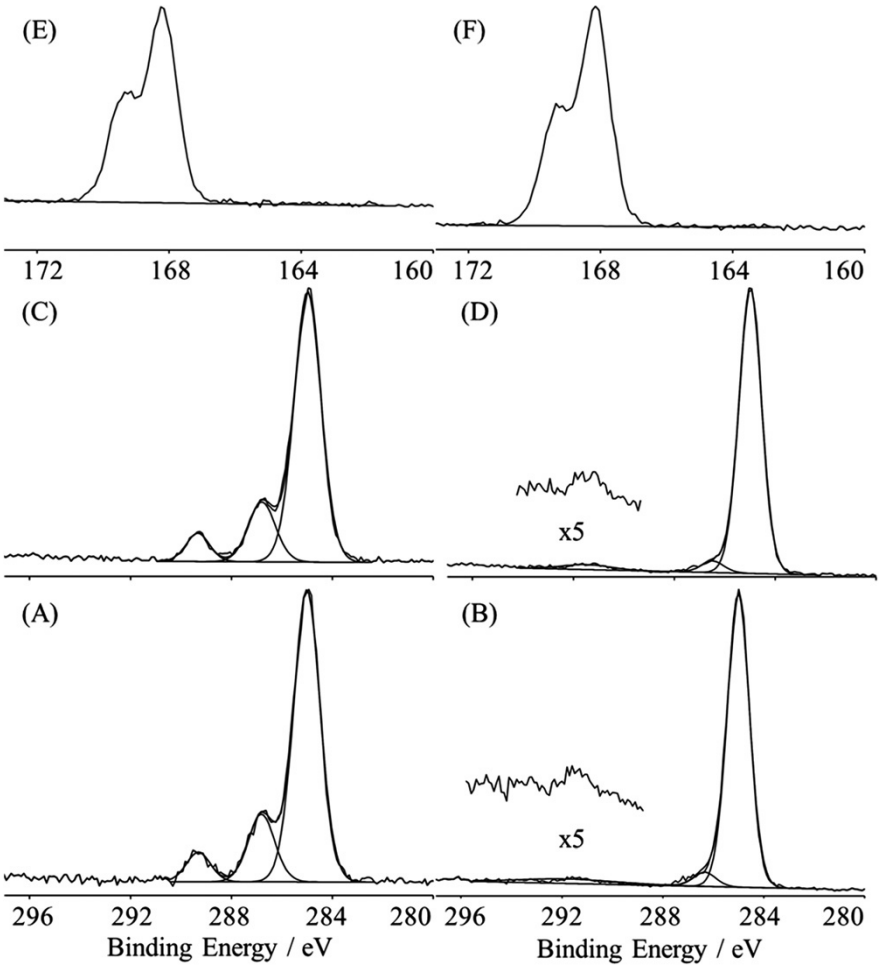

Figure 3.3. XPS high resolution C_{1s} spectra of the ClSi (A) and NaSS (B) films on Ti; XPS high resolution C_{1s} spectra of the ClSi (C) and NaSS (D) films on Si; XPS high resolution S_{2p} spectra of the NaSS film on Ti (E) and Si (F).

3.4.3 ToF-SIMS

PCA results from the ToF-SIMS spectra are reported for an m/z range from 0 – 400 (Fig. 4 A and B). Peaks of intensity 3x the background could not be found outside of that range. PCA results for the negative spectra (Figs. 3.4 A and B) separate the ClSi from the NaSS samples: ClSi samples load positively and are associated with Br^- and Si-containing peaks; NaSS samples load negatively and are associated with sulfonate containing fragments and the NaSS monomer $(C_8H_7SO_3^-)$. The 95% confidence intervals for the NaSS samples on the two different substrates overlap completely, indicating that PCA is unable to chemically differentiate NaSS films prepared on Ti and Si substrates. The same is true of the ClSi samples when the entire data set is

analyzed at once. However, when analyzed by themselves, the ClSi samples separate based on substrate type, indicating that the ClSi film thickness is less than the ~2 nm SIMS sampling depth (not shown).

The positive spectra PCA results separate the samples in the same way, with the ClSi samples loading positively and the NaSS samples loading negatively. However, since both ClSi and NaSS contain electronegative atoms (e.g., O, S, Br), most of the ClSi and NaSS characteristic ions are present in the negative spectra. The $BrC_3H_6^+$ peak in the positive spectra is the only fragment found that can be attributed to the ClSi head group. As expected, several Na-containing ions (Na^+, Na_2OH^+, $SO_3Na_3^+$, $SO_4Na_3^+$) are present in the positive ion spectra of the NaSS samples.

Figure 3.5 shows 500 × 500 μm^2 ToF-SIMS images of the Br^- signal (Fig. 3.5 A and B) and the sum of $C_xH_ySO_3^-$ fragments (Fig. 3.5 C and D) for both Ti and Si substrates. The Br^- images show uniform coverage, at the spatial resolution used in the ToF-SIMS analysis (~2 μm), of the ClSi film across both substrates. Similar results are obtained for the sum of Br-containing fragments (e.g., BrC_xH_y) in the positive polarity. However, the signal is lower for the Si substrate since many of the Br-containing fragments are Ti adducts. The $C_xH_ySO_3^-$ images also show uniform coverage of NaSS across both substrates.

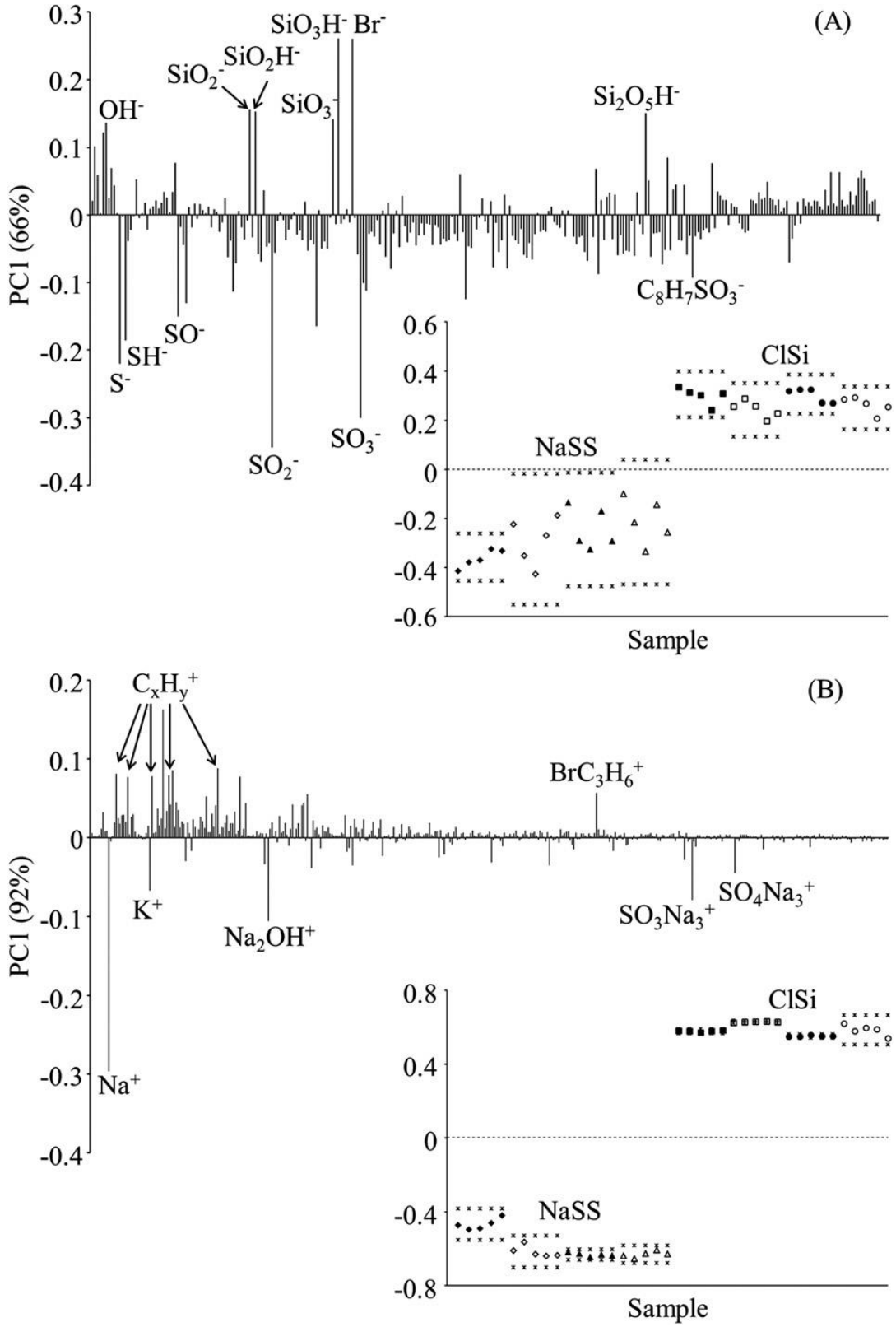

Figure 3.4. ToF-SIMS PCA loadings plots with inset scores plots for negative (A) and positive (B) secondary ion spectra.

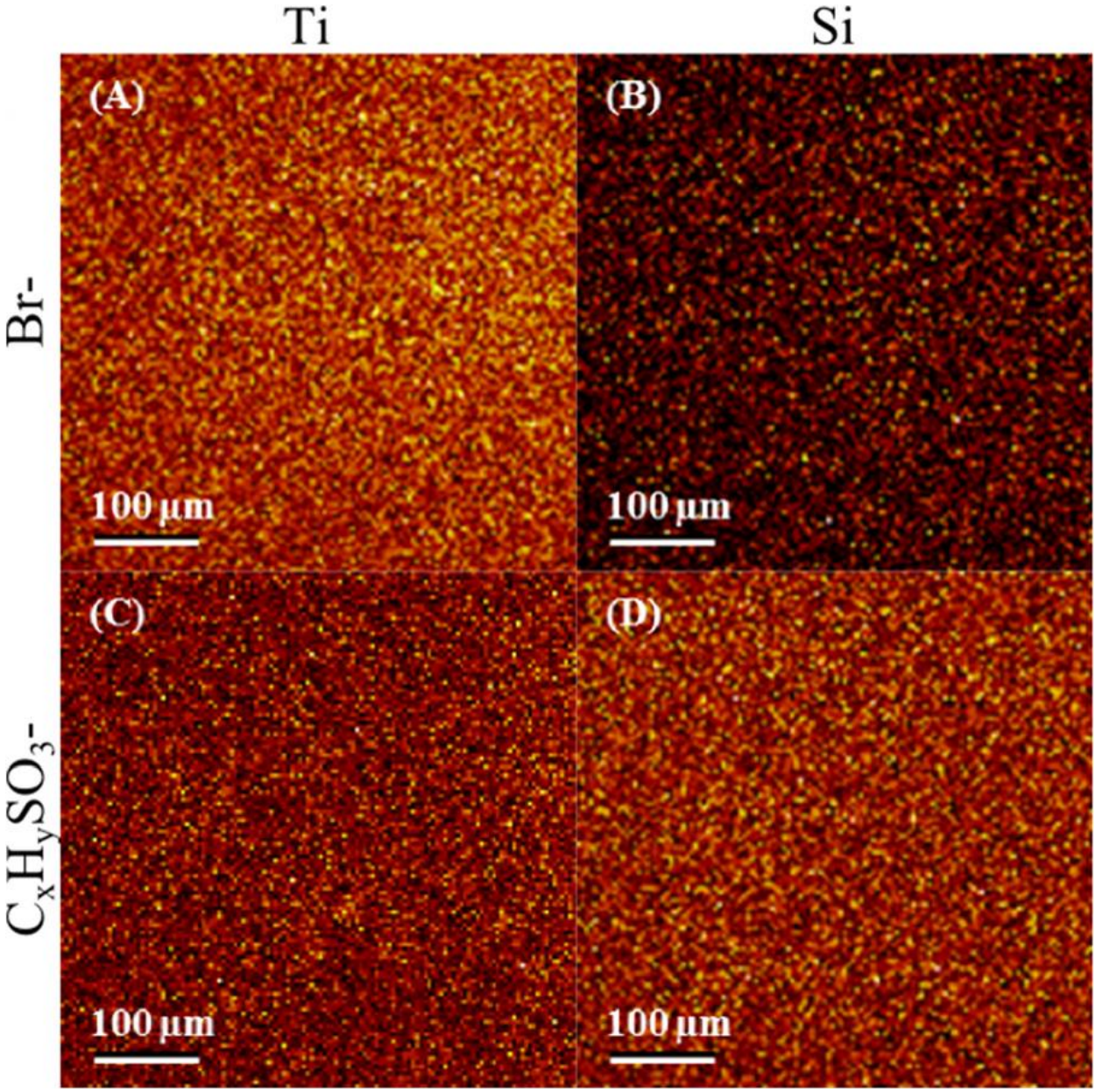

Figure 3.5. 500 × 500 µm^2 ToF-SIMS images of the Br^- signal on ClSi functionalized Ti (A) and Si (B) substrates, and the sum of $C_xH_ySO_3^-$ fragments on NaSS grafted Ti (C) and Si (D) substrates.

3.4.4 VASE

The ellipsometry models were built stepwise from VASE measurements performed on two samples each of blank, ClSi-functionalized, and NaSS-grafted Si and Ti substrates. Thicknesses for the ClSi and pNaSS layers are reported in Table 3.2. The blank Si samples were treated as a

SiO_2 layer atop a pure Si substrate using prefabricated Si and SiO_2 models included in the CompleteEASE software. This model returned an oxide layer thickness of 2.3 nm for the VASE measurements, and a range of oxide thicknesses between 2.3 – 2.7 nm for the ellipsometry mapping measurements.

Table 3.2. Ellipsometry and AFM determined ClSi and pNaSS film thicknesses (nm). SE mapping thicknesses are reported as the avg ± stdev of the 25 spots measured across each sample (see Figure 6). Scratch test thicknesses are reported as the avg ± stdev of three spots across each sample. Replicate number refers to the fact that two replicates of each substrate were prepared and analyzed after each treatment.

Substrate	Film	Replicate Number	VASE (nm)	SE Mapping (nm)	Scratch Test (nm)
Si	ClSi	1	1.3	1.5 ± 0.2	1.4 ± 0.2
		2	1.8	1.2 ± 0.1	1.1 ± 0.1
	pNaSS	1	24.7	25.4 ± 3.8	16.8 ± 2.1
		2	45.7	48.9 ± 5.9	49.0 ± 3.8
Ti	ClSi	1	2.3	2.1 ± 0.2	1.9 ± 0.1
		2	1.1	0.9 ± 0.1	1.6 ± 0.2
	pNaSS	1	13.2	13.3 ± 0.5	10.8 ± 1.3
		2	33.8	34.9 ± 3.4	41.0 ± 8.8

The modeling of deposited Ti VASE spectra is complicated by the large TiO_2 band gap. Additionally, the high reactivity of Ti means that, even under high vacuum conditions, the oxide film composition is difficult to control and can vary with thickness to include sub-oxides (e.g., Ti_2O_3), nitrides, and carbides.[86-88] Thus, developing a physically meaningful VASE model that accurately describes the optical properties and thickness of deposited Ti film is non-trivial. However, determination of the Ti substrate optical properties is not a focus of this study. Therefore, the analysis was simplified by treating the blank Ti samples as a single layer using a B-spline function to parameterize the pseudo optical properties of the substrate.[89, 90]

The Cauchy dispersion equation, which is suitable for transparent thin films such as silanes,[89, 91] was used to fit the VASE measurements on the ClSi-functionalized substrates. The Cauchy model yielded ClSi-layer thicknesses of ~ 1.5 nm on Si, and 1 – 2 nm on Ti, which are in good agreement with the XPS-determined overlayer thicknesses. This indicates that the ClSi functionalization process produces similar thickness films on both Si and Ti substrates.

Thickness maps for one replicate ClSi-functionalized on the Si and Ti substrates are shown in Fig. 3.6 A and B, respectively.

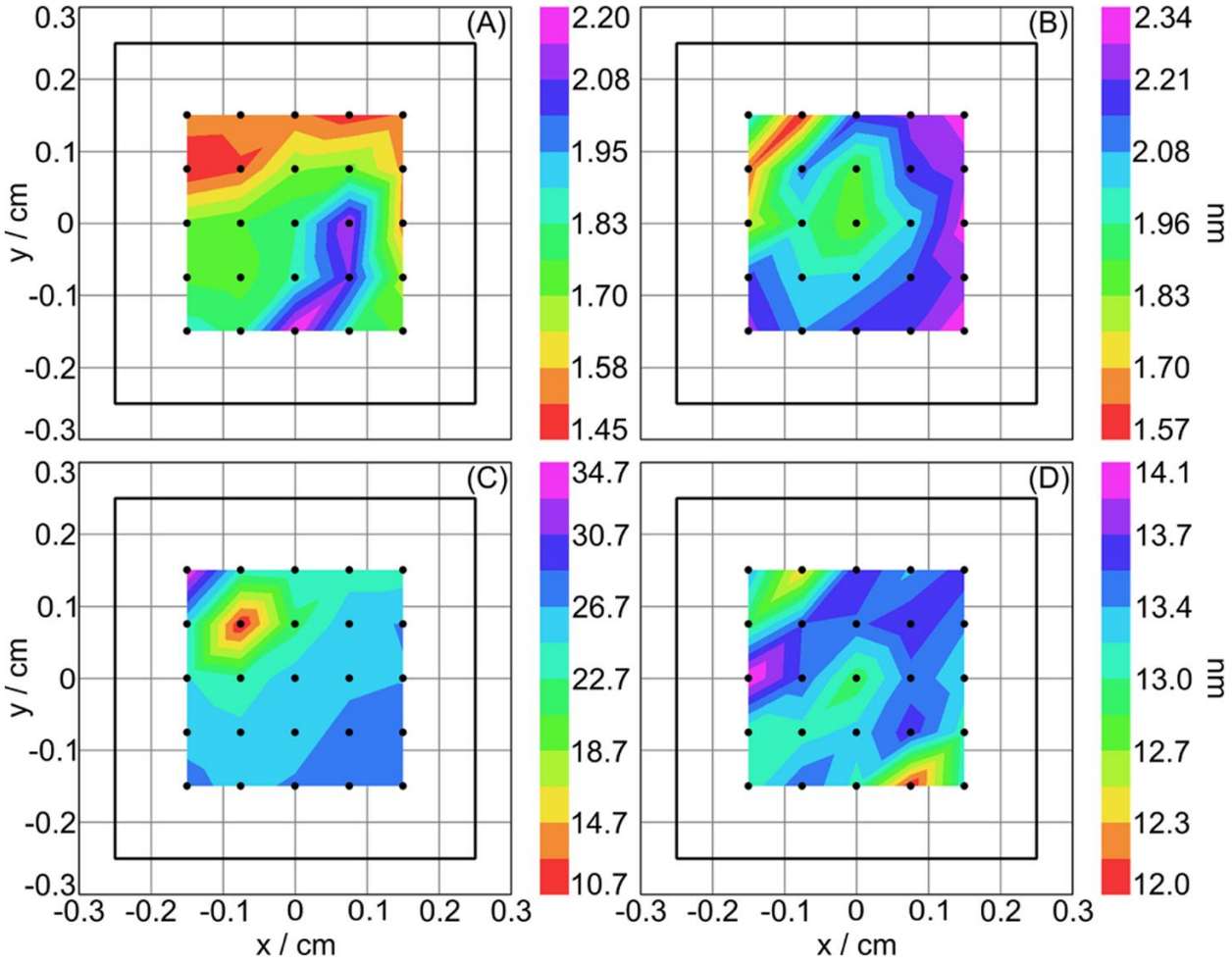

Figure 3.6. Ellipsometry thickness maps for the ClSi-functionalized Si (A) and Ti (B) substrates, and for NaSS-grafted Si (C) and Ti (D) substrates.

The pNaSS films on both substrates had a visible yellow tint to them. Therefore, in addition to absorbing in the UV range due to benzene ring $\pi - \pi^*$ transition,[92] they absorb in the yellow visible range (~600 nm). Therefore, the optical properties were once again parameterized with a B-spline function, yielding pNaSS film thicknesses between 25 – 49 nm on Si, and 13 – 34 nm on Ti. Figure 6 C and D shows the pNaSS films to be fairly uniform across the substrate, and that the wide range in pNaSS film thicknesses represents the variability between replicates. It should be noted that the thinner Si and Ti replicates both came from the same reaction vial, as did the

thicker Si and Ti replicates. Thicknesses obtained from AFM scratch test measurements (Table 2) are in excellent agreement with the ellipsometry results. Thickness maps for one replicate of the NaSS-grafted Si and Ti samples are shown in Fig. 3.6 C and D, respectively. Thus, it appears that the grafting reaction produces slightly thicker films on Si, and that relatively large variances in film thickness may be expected between batches. These differences are despite running each reaction with one Si and one Ti each vial, and using the same catalyst mixture for all reactions.

The film-thickness differences *between substrates* might be attributed to differences in ClSi film quality, since organosilane self-assembled monolayer (SAM) quality is known to be affected by substrate roughness and surface chemistry.[93] This hypothesis is supported by the SE mapping measurements, since the ClSi film thicknesses on Ti are much more variable than on Si: the 2.1 nm average thickness for Ti replicate 1 could be indicative of multilayer formation, and the 0.9 nm average thickness for replicate 2 could be indicative of a less well-ordered film. As a reference, C_{11} organosilane monolayers on Si were found to be ~ 1.5 nm thick, which is in the same range as the ClSi films on Si.[94] The film-thickness differences *between batches* could also be due to sensitivity toward small variances in reaction conditions. For example, ATRP is very sensitive to oxygen. Therefore, solvents are always degassed with either nitrogen or argon to purge dissolved oxygen, and reactions quenched by exposure to air.[59-73] Thus, it may be that a small leak in vial 1 lead to the premature termination of the grafting reaction and thinner pNaSS films on Si and Ti replicate 1.

3.4.5 AFM

AFM images are shown in Fig. 3.7 and average RMS roughness values ± standard deviations are reported in Table 1. Within error, the Ti roughness values remain constant regardless of treatment. The AFM images (Fig. 3.7 D – F) show the surface topography of the Ti samples to be unchanged by the ClSi treatment and significantly changed by the pNaSS grafting. However, the Si roughness values increase significantly with each treatment, as does the surface topography (Fig. 3.7 A – C). Interestingly enough, despite the difference in roughness values between the bare Ti and Si substrates, within error there is no difference in the roughness values of the NaSS films grafted from the two substrates. This indicates that the NaSS film is thick enough to obscure the initial Ti roughness, and that the uniformity of NaSS films grown by surface initiated ATRP under the above reported conditions can be taken to be approximately 2 nm.

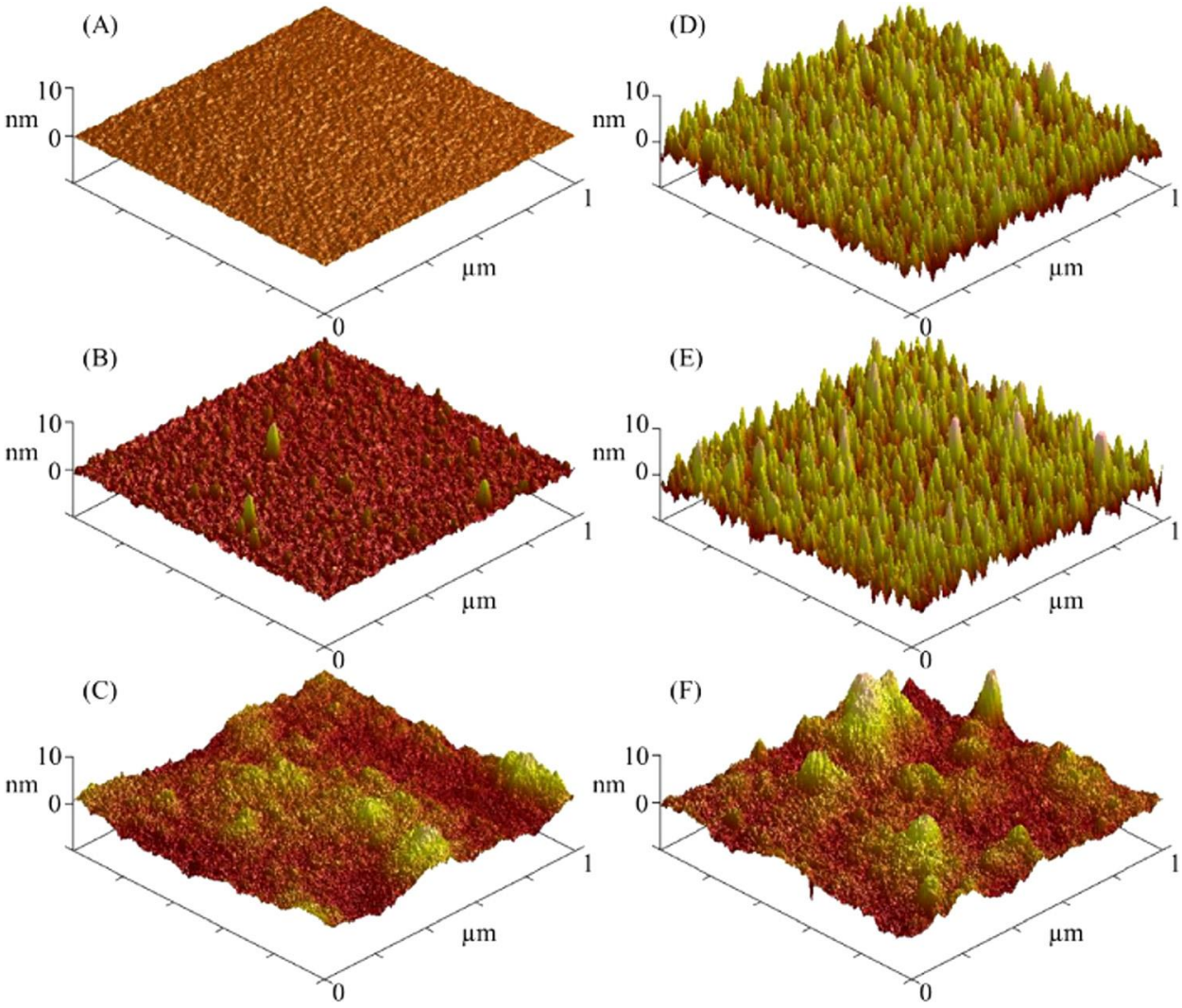

Figure 3.7. 1 × 1 µm^2 AFM images of bare Si (A) and Ti (D) substrates, ClSi-functionalized Si (B) and Ti (E) substrates, and NaSS grafted Si (C) and Ti (F) substrates.

3.5 Summary and Conclusions

In this study we used ATRP to graft NaSS from ClSi functionalized Si and Ti surfaces. The composition, molecular structure, thickness, and topography of the grafted pNaSS films were characterized with XPS, ToF-SIMS, VASE, and AFM, respectively. XPS and ToF-SIMS results confirmed that both Si and Ti substrates were successfully first functionalized with a ClSi layer and then grafted with a laterally chemically homogeneous NaSS film. VASE and spectroscopic ellipsometry mapping measurements found the grafting reaction produces slightly thicker NaSS films on Si vs. Ti substrates, and that relatively large variances in film thickness may be expected between batches. AFM found that within error there is no difference in NaSS film roughness

values between the Si and Ti substrates, despite relatively large differences bare-substrate roughness values. Thus, we have successfully produced chemically homogeneous and relatively smooth NaSS-grafted substrates. These may now be used in subsequent studies testing the hypothesis that pNaSS-grafted Ti implants preferentially adsorb certain plasma proteins in an orientation and conformation that modulates the foreign body response and promotes formation of new bone.

3.6 Acknowledgements

This study was supported by NIH grant EB-002027 (RNF and DGC) and ONR grant N000141210441 (AJK and SJ). The ellipsometry experiments were done at the University of Washington Nanotechnology User Facility, a member of the NSF National Nanotechnology Infrastructure Network. Prof. Veronique Migonney is thanked for stimulating discussions about the preparation and biological applications of grafted NaSS films. Special thanks to Dr. Jonathan Lane, without whose mentorship, and encouragement to publish these results, this publication might not have been realized.

4. Experimental Design and Analysis of ARGET-ATRP Experimental Conditions for Grafting Sodium Styrene Sulfonate from Titanium Substrates

Rami N. Foster
Department of Chemical Engineering, University of Washington – Seattle, and National ESCA and Surface Analysis Center for Biomedical Problems, Seattle, WA 98195

Patrik K. Johansson
Department of Bioengineering, University of Washington – Seattle, and National ESCA and Surface Analysis Center for Biomedical Problems, Seattle, WA 98195

Nicole R. Tom
Department of Chemical Engineering, Carnegie Mellon University, Pittsburg, PA 15213

Patrick Koelsch
Department of Bioengineering, University of Washington – Seattle, and National ESCA and Surface Analysis Center for Biomedical Problems, Seattle, WA 98195

David G. Castner
Departments of Chemical Engineering and Bioengineering, University of Washington – Seattle, and National ESCA and Surface Analysis Center for Biomedical Problems, Seattle, WA 98195

4.1 Abstract

A 2^4 factorial design was used to optimize the activators regenerated by electron transfer-atom transfer radical polymerization (ARGET-ATRP) grafting of sodium styrene sulfonate (NaSS) films from trichlorosilane/10-undecen-1-yl 2-bromo-2-methylpropionate (ester ClSi) functionalized titanium substrates. The process variables explored were: A) ATRP initiator surface functionalization reaction time; (B) grafting reaction time; (C) CuBr2 concentration; (D) reducing agent (vitamin C) concentration. All samples were characterized using x-ray photoelectron spectroscopy (XPS). Two statistical methods were used to analyze the results: (1) Analysis of variance (ANOVA) with $\alpha = 0.05$, using average √Ti XPS atomic percent as the response; (2) Principal component analysis (PCA) using a peak list compiled from all the XPS composition results. Through this analysis combined with follow-up studies, the following conclusions are reached: (1) ATRP-initiator surface functionalization reaction times have no discernable effect on NaSS film quality; (2) minimum (≤ 24 hr for this system) grafting reaction times should be used on titanium substrates since NaSS film quality decreased and variability increased with increasing reaction times; (3) minimum (≤ 0.5 mg cm-2 for this system) CuBr2 concentrations should be used to graft thicker NaSS films; (4) no deleterious effects were detected with increasing vitamin C concentration.

4.2 Introduction

Controlling surface properties is important in a number of fields.[21, 29, 95, 96] One strategy to do so is polymer grafting. Activators regenerated by electron transfer-atom transfer radical polymerization (ARGET-ATRP) is a versatile and scalable method for polymer synthesis. When combined with a material-specific strategy for immobilizing an ATPR initiator, ARGET-ATRP can be used to modify most metal, oxide, and ceramic surfaces,[21, 29, 30] as well as polymer surfaces.[36, 97-99] However, much of the fundamental understanding of ARGET-ATRP, or more generally ATRP, is based on studies focusing on solution-phase polymerizations.[80, 100-106] While publications describing ATRP and ARGET-ATRP grafting of different polymers from a variety of surfaces are plentiful in the literature, the authors are aware of few studies that explore in detail the relationship between process variables and film quality. (We define high quality films to be thick and laterally homogeneous—i.e., hole and defect free.) Therefore, in this study we use surface analysis techniques to characterize and optimize the grafting of sodium styrene sulfonate (NaSS) from trichlorosilane/10-undecen-1-yl 2-bromo-2-methylpropionate-

functionalized titanium surfaces (figure 4.1). Interest in NaSS extends to a number of applications, such as an antiflocculating agent, emulsifier, catalyst, and for use in ion-exchange resins and membranes.[69-71, 79] It has also shown promise as a strategy to increase the osseointegration of titanium[15-17, 20] and poly(ethylene terephthalate)[14, 18, 107] biomedical implants. To investigate possible reasons for the increased osseointegration of these materials, in future studies the authors intend to test the hypothesis that the NaSS-grafted surfaces preferentially adsorb certain plasma proteins in an orientation and conformation that modulates the foreign body response and promotes formation of new bone. A necessary prerequisite for doing so is the ability to reliably produce sufficient quantities of high quality NaSS-grafted substrates. Therefore, the goals of this work are twofold: (1) examine the influence of experimental conditions on NaSS grafting; and (2) by doing so, further our general understanding of ARGET-ATRP grafting from surfaces. To this end a 2^4 factorial design was performed to study the following variables: (A) ATRP initiator surface functionalization reaction time; (B) grafting reaction time; (C) $CuBr_2$ concentration; (D) reducing agent (vitamin C) concentration.

Even though statistical experimental design methods are extremely useful in efficiently optimizing process conditions, they rarely go as planned. Under "real world" conditions, undesired and uncontrolled changes in process conditions are routinely encountered. These can obscure trends and further complicate analysis of the experimental design results. The current work is no exception, where an analyzer upgrade for the X-ray photoelectron spectrometer occurred during data collection. Therefore, in addition to the traditional analysis of variance (ANOVA), we employed principal component analysis (PCA) to evaluate the factorial design results. Through this combination of statistical analyses, we were able to account for the effect of the analyzer upgrade on the data and draw meaningful conclusions regarding optimal NaSS grafting conditions, which is the main focus of this paper.

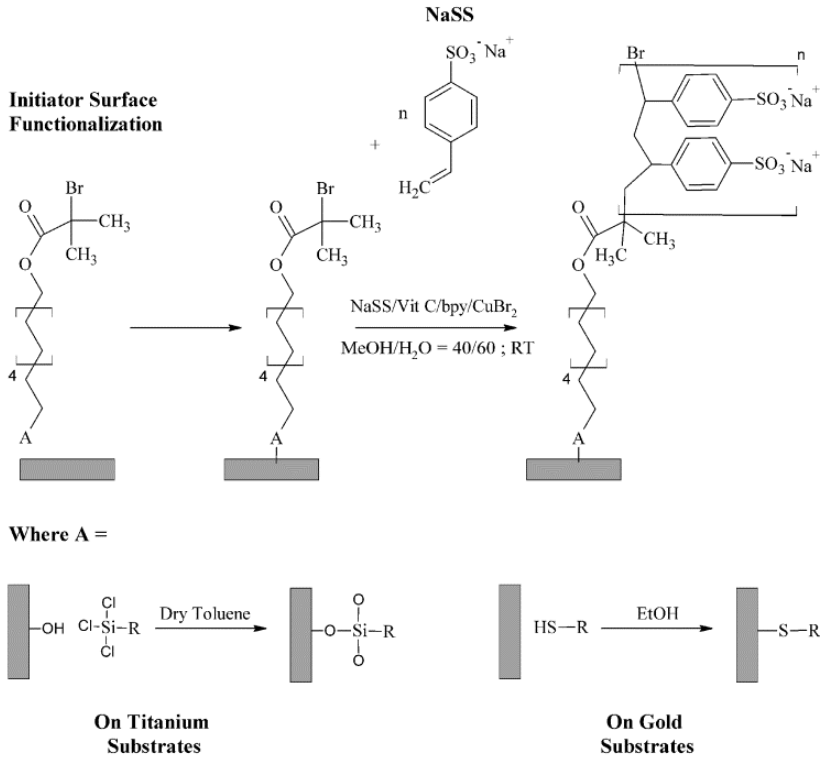

Figure 4.1. Schematic representation of the two-step NaSS grafting procedure. Step 1: surface immobilization of the ATRP initiator using a material-specific functionalization strategy to form either thiol (on gold) or silane (on titanium) self-assembled monolayers. Step 2: ARGET-ATRP grafting of NaSS from the surface-bound initiator.

4.3 Experimental

4.3.1 Materials

Silicon wafers (Silicon Valley Microelectronics Inc., San Jose, CA) were diced into 1×1 cm^2 substrates using a diamond saw. Titanium substrates were fabricated by evaporation of 100 nm of titanium from an electron-beam heated titanium target onto diced silicon substrates at room temperature and vacuum pressures < $3x10^{-6}$ torr. Gold substrates, also 100 nm thick, were fabricated in the same way, first depositing a 5 nm titanium adhesion layer. Methanol, acetone, dichloromethane, toluene, phosphate buffered saline (PBS; 0.010 M phosphate, 0.138 M sodium chloride, 0.0027 M potassium chloride, pH 7.4), Cu(II) bromide (>99.0%), 2,2'-bipyridine (bpy) (≥99%), vitamin C (≥98%), and sodium styrene sulfonate (NaSS) (≥90%) were all purchased

from Sigma. Ethanol (200 proof) was purchased from Decon Laboratories. The toluene was dried by storing over 4A molecular sieves; the rest of the chemicals were used as received. The synthesis of the ATRP initiator, trichlorosilane/10-undecen-1-yl 2-bromo-2-methylpropionate (henceforth referred to as ester ClSi), has been described previously.[36] An amide (referred to as amide ClSi) version of the same molecule was graciously provided by the Jiang group at the University of Washington. Bromoisobutyrate undecyl disulfide (99%) (henceforth referred to simply as thiol, since it forms a gold-thiolate bond on the surface) was purchased from Asemblon.

4.3.2 Substrate cleaning and ATRP-initiator functionalization

Prior to the e-beam deposition, substrates were cleaned by sonicating twice for 5 minutes each sequentially in dichloromethane, acetone, and methanol. The e-beam deposited titanium substrates were functionalized in a 0.2 vol. % solution of ester ClSi in dry toluene for the length of time specified by the factorial design. Functionalized substrates were rinsed in dry toluene followed by methanol, and then briefly dipped in 1mM NaOH to cross-link the surface silanes and neutralize HCl byproducts.

E-beam deposited gold substrates were rinsed with ethanol and immersed in a 1 mM solution of thiol in ethanol for 18 – 24 hrs. The substrates were then rinsed with ethanol, sonicated for 1 – 3 min. to remove any unbound thiol, and rinsed once more with ethanol. Both the titanium and gold functionalization reactions were performed at room temperature in N_2-backfilled glass test tubes stoppered with rubber septa.

4.3.3 ARGET-ATRP

The ARGET-ATRP reaction solids were weighed into three 20-ml glass scintillation vials. The first contained 203 mg (98.6 mmol) of NaSS monomer dissolved in 1.2 ml 18-Ω DI H_2O. The second contained $CuBr_2$ and bpy (1:2 ratio) dissolved in 2.4 ml methanol and 1.2 ml 18-Ω DI H_2O. The third vial contained vitamin C dissolved in 1.2 ml 18-Ω DI H_2O. The total solvent volume was 6 ml (60/40 H_2O/methanol). The amount of $CuBr_2$/bpy and vitamin C varied depending on the treatment combination as dictated by the experimental design. The catalyst solution, along with two initiator-functionalized substrates, was added to the NaSS vial, making sure that the substrates stayed face up and did not overlap each other. NaSS grafting was initiated upon addition of the vitamin C solution to the reaction vial, which was then capped and sealed

with parafilm. Since excess vitamin C is present during the reaction, it is not necessary to degas the reaction solvent. After the allotted time specified by the factorial design the substrates were rinsed with 18-Ω DI H_2O, soaked in PBS for several hours, and then soaked overnight in 18-Ω DI H_2O to remove any residual catalyst, excess sodium/buffer salts, and monomer. Finally, the grafted substrates were rinsed again with 18-Ω DI H_2O, gently dried with a stream of N_2, and stored under N_2 until analyzed.

4.3.4 X-Ray Photoelectron Spectroscopy (XPS)

XPS data were acquired on an SSI S-Probe instrument (Surface Science Instruments, Mountain View, California). Half way through the first replicate of the factorial design, the analyzer was upgraded and the photoelectron takeoff angle (TOA) changed from 55° to 0°. Here, the photoelectron TOA is defined as the angle between the surface normal and the axis of the analyzer lens. All spectra were acquired using a monochromatic Al $K\alpha_{1,2}$ X-ray source (hv = 1486.6 eV). Atomic compositions were calculated from peak areas obtained from survey scans (0–1100 eV) with analyzer pass energy of 150 eV, a 1 eV step size, and a 100 ms dwell time. Carbon chemical shifts were determined from high-resolution C_{1s} spectra obtained with analyzer pass energy of 50 eV, a 0.065 eV step size, and 100 ms dwell time. All samples were grounded to the spectrometer and run as conductors. Binding energy scales were calibrated by setting the CH_x peak in the C_{1s} region to 284.6 eV, and a linear background was subtracted for all peak area quantifications. The peak areas were normalized by the manufacturer supplied sensitivity factors, and surface concentrations were calculated using Hawk Data Analysis 7 (Service Physics, Inc., Bend, Oregon).

4.3.5 Atomic Force Microscopy (AFM)

AFM images were acquired on a Dimension Icon (Bruker, Santa Barbara, CA) in TappingMode^{TM} using OTESPA rectangular cantilevers (k = 40 N/m; Bruker, Santa Barbara, CA). Images were line and plane flattened as necessary the using the NanoScope Analysis software package. Scratch-test measurements were also performed to determine NaSS film thicknesses. These consisted of using a high deflection set point in contact mode to scratch a 5 × 5 μm^2 hole in the NaSS film, reducing the deflection set point, and increasing the scan size to 20 × 20 μm^2 to determine the depth of the scratched hole. This procedure was iterated, each time

scratching with a higher deflection set point until the thickness remained constant between iterations.

4.3.6 Vibrational Sum Frequency Generation Spectroscopy (SFG)

SFG spectra were measured with a ps-pulsed laser system (EKSPLA, Nd:YAG and OPA/OPG/DFG). Spectra were collected for ester ClSi films on Ti surfaces, functionalized for either 1 or 7 days, to determine the effect of reaction time on the ester ClSi film quality. The incident angles relative the surface normal were 60° and 62° for the infrared (IR) and visible beams, respectively. The *ppp* (*p*-polarized SFG, *p*-polarized visible and *p*-polarized IR) polarization combination was used for all spectra. Average data acquired from three replicates of each sample (1 day and 7 days) were analyzed for the ester and C-H spectral regions (ester: 1700-1800 cm^{-1} and C-H: 2800-3000 cm^{-1}), with one exception (7 days, ester region: 1700-1800 cm^{-1}) where average data acquired from four replicates were analyzed. For the ester region, a step size of 1 cm^{-1} was used with 600 acquisitions per step, while a step size of 2 cm^{-1} and 400 acquisitions per step were used for the C-H region. To account for any variations in IR and visible intensities that occurred during spectra acquisition, all data points were normalized against a signal produced in parallel from an SFG-active crystal (ZnS).

4.3.7 Factorial Design

A 2^4 factorial design was performed varying (A) ester ClSi reaction time, (B) grafting reaction time, (C) $CuBr_2$ concentration, and (D) vitamin C concentration (table 4.1). Two duplicate samples were prepared and analyzed at each treatment combination. The entire design was replicated twice totaling four samples per treatment combination. The run order was randomized but within replicates only. The design matrix and response are listed in table 4.2.

Table 4.1. Factors and treatment levels.

Factor	Symbol	Low (-1)	High (1)
Ester ClSi Reaction Time	A	24 hrs	72 hrs
Grafting Reaction Time	B	24 hrs	72 hrs
$CuBr_2$	C	1 mg cm-2	2 mg cm-2
Vitamin C	D	39.5 mg cm-2	79 mg cm-2
Covariate	-	Pre-upgrade	Post-upgrade

Table 4.2. Experimental conditions and results.

Treatment Combination	Ester ClSi Reaction Time (hrs)		Grafting Reaction Time (hrs)		$CuBr_2$ (mg cm^{-2})		Vitamin C (mg cm^{-2})		Covariate*	Replicate 1	Replicate 2
	A		B		C		D			√Ti	
(1)**	-1	(24)	-1	(24)	-1	(1)	-1	(79)	1	1.11	0.17
A	1	(72)	-1	(24)	-1	(1)	-1	(79)	-1	0.00	0.09
B	-1	(24)	1	(72)	-1	(1)	-1	(79)	-1	2.29	3.55
AB	1	(72)	1	(72)	-1	(1)	-1	(79)	1	1.21	0.18
C	-1	(24)	-1	(24)	1	(2)	-1	(79)	-1	0.00	0.00
AC	1	(72)	-1	(24)	1	(2)	-1	(79)	1	1.15	0.12
BC	-1	(24)	1	(72)	1	(2)	-1	(79)	1	0.64	2.34
ABC	1	(72)	1	(72)	1	(2)	-1	(79)	-1	0.22	1.87
D	-1	(24)	-1	(24)	-1	(1)	1	(158)	-1	0.48	0.43
AD	1	(72)	-1	(24)	-1	(1)	1	(158)	1	1.16	0.18
BD	-1	(24)	1	(72)	-1	(1)	1	(158)	1	0.62	2.46
ABD	1	(72)	1	(72)	-1	(1)	1	(158)	-1	0.00	1.15
CD	-1	(24)	-1	(24)	1	(2)	1	(158)	1	0.76	1.44
ACD	1	(72)	-1	(24)	1	(2)	1	(158)	-1	0.00	1.09
BCD	-1	(24)	1	(72)	1	(2)	1	(158)	-1	0.00	0.36
ABCD	1	(72)	1	(72)	1	(2)	1	(158)	1	1.22	1.71

*The covariate levels apply to replicate 1 only. The covariate level was 1 (analyzer angle of 0^o) throughout replicate 2.

**The treatment combination "(1)" is where low (-1) levels are used for all factors. See table 4.1 for these experimental conditions.

4.3.8 Data Analysis

The factorial design was analyzed using both analysis of variance (ANOVA) with $\alpha = 0.05$ and principal component analysis (PCA). For the ANOVA, average √Ti XPS atomic percent was chosen as the response. XPS data are technically "count-based," thus the decision to use square-root transformed titanium compositions.[108] Since the experimental order was randomized within replicates only, blocking was performed on replicates. The additional variance added to the

system by the analyzer upgrade was accounted for by including a covariate in the ANOVA. Also, some spectra were discarded due to sample charging. Even with the discarded data at least seven spectra were collected for each treatment combination, whereas the remaining responses represent a total of twelve measurements. All ANOVA were done "by hand" in MS Excel. Chapters 3, 5, and 6 from reference[108] are recommended as a resource for more information about factorial designs.

PCA, previously described in detail,[74-76] is a multivariate analysis technique used to identify principal sources of variation between sample spectra. Briefly, PCA can be described as a clustering algorithm with two outputs: a scores plot and a loadings plot. Samples that cluster closely together in the scores plot are considered more similar to each other than those that do not. The loadings plot explains the differences between the samples. Samples with negative scores are associated with variables with negative loadings, and vice versa. Peak lists for all 173 XPS spectra—composed of S, C, Ti, O, and Na—were imported into a series of scripts written by NESAC/BIO for MATLAB (MathWorks, Inc., Natick, MA).[77, 78] Although data normalization is often performed prior to PCA, XPS compositions are in the form of atomic percentages and therefore already normalized. The data were, however, square-root transformed and mean centered to be consistent with the ANOVA procedure and to ensure that variance within the data set was due to differences in sample variances rather than in sample means.

4.4 Results/Discussion

Since the focus of this work is optimizing ARGET-ATRP grafting conditions, the extensive set of spectral data from the NaSS-grafted substrates used in this study is not provided here. However, readers desiring further details regarding characterization of NaSS-grafted substrates are directed to reference[50], which describes characterization of NaSS-grafted titanium and silicon substrates using XPS, AFM, time-of-flight secondary ion mass spectrometry (ToF-SIMS), and spectral ellipsometry.

4.4.1 Factorial Design Analysis/Results

The factorial design was analyzed using both ANOVA and PCA. Three main advantages of ANOVA are: (1) causal relationships can be established between the effects and the response; (2) higher-level (two-way, three-way, etc.) interaction effects can be investigated; (3) the analysis typically yields a physically meaningful regression model that can be used to optimize process

conditions within the investigated experimental space.[108] However, only one response can be considered at a time and any remaining information is discarded. This is illustrated by the system at hand. Average √Ti XPS atomic percent is a logical choice of response since increasing substrate signal is indicative of either patchy or thin grafted NaSS films and therefore inversely proportional to film quality. However, this approach neglects the remaining elements (C, S, Na, etc.) found in the XPS composition results. PCA, on the other hand, is able to handle complex data sets, meaning that all of the XPS composition results can be simultaneously analyzed.

Table 4.3. ANOVA results.

Source	Sum of Squares	Degrees of Freedom	Mean Square	F_o*	F_{crit}*	P-value	Significant?
A	0.87	1	0.87	2.35	4.60	0.15	
B	4.26	1	4.26	11.45	4.60	4.5E-3	yes
C	0.14	1	0.14	0.39	4.60	0.54	
D	0.11	1	0.11	0.30	4.60	0.59	
AB	0.53	1	0.53	1.41	4.60	0.25	
AC	2.51	1	2.51	6.76	4.60	0.02	yes
AD	0.85	1	0.85	2.30	4.60	0.15	
BC	0.52	1	0.52	1.40	4.60	0.26	
BD	1.84	1	1.84	4.96	4.60	0.04	yes
CD	0.18	1	0.18	0.48	4.60	0.50	
ABC	1.58	1	1.58	4.26	4.60	0.06	
ABD	1.43	1	1.43	3.84	4.60	0.07	
ACD	0.29	1	0.29	0.79	4.60	0.39	
BCD	0.00	1	0.00	0.00	4.60	0.97	
ABCD	0.76	1	0.76	2.04	4.60	0.18	
Covariate	2.52	1	2.52	6.77	4.60	0.02	yes
Blocks	1.23	1	1.23	3.32	4.60	0.09	
Error	5.20	14	0.37				
Total	24.84	31					

*F_o is referred to as the test statistic, and is calculated by diving the mean square for each effect by the mean square error. F_{crit} is the critical value, based on the F-distribution, which the test statistic must be greater than for an effect to be considered significant.

$$\sqrt{Ti} = 0.87 + 0.36x_B + 0.28x_Ax_C - 0.24x_Bx_D \text{ (Eq. 1)}$$

Table 4.4. Goodness-of-fit statistics for the regression model (Eq. 1).

Statistic	Value
R^2	0.35
$R^2{}_{adj}$	0.30
$R^2{}_{predicted}$	-0.23

The ANOVA results and regression model can be found in table 4.3 and equation 1. Plots of the residuals are found in figure S4.1 of the supporting information. The significant factors are B (grafting reaction time; P = 4.5E-3), AC (the two-way interaction between ester ClSi reaction time and $CuBr_2$ amount; P = 0.02), and BD (the two-way interaction between grafting reaction time and vitamin C amount; P = 0.04). The covariate was also significant, indicating that the analyzer upgrade had an impact on the response. This is expected since the sampling depth—defined as three times the inelastic mean free path (IMFP, λ) times the cosine of the TOA (Eq. 2)—nearly doubled with the analyzer upgrade. The relative concentrations of overlayer (NaSS) to substrate (TiO_2) signals will change with increasing sampling depth.

$$Sampling\ Depth = 3\lambda \cos(TOA) \quad \text{(Eq. 2)}$$

Interpretation of the ANOVA results and regression model is somewhat challenging for multiple reasons. First, from the goodness-of-fit statistics (table 4.4), Eq. 1 does not account for much of the variance in this system (R^2 values significantly less than 1) despite the negative $R^2{}_{predicted}$ value, which suggests that the data are overfit. Next, interaction terms are significant ($x_A x_C$ and $x_B x_D$), when their constituent main effects are not (x_A, x_C, and x_D). This is could be a residual artifact of the analyzer upgrade and the discarded spectra, for which the covariate could not adequately compensate. However, further complicating matters is the fact that grafting reaction time is involved in two terms—as a main effect (x_B) and also as a two-way ($x_B x_D$) interaction—with opposite signs. The main effect is the most significant term in the regression model and the positive coefficient suggests that titanium signal increases with increasing reaction time. Or, stated another way, film quality decreases with increasing reaction time. However, the two-way interaction ($x_B x_D$) coefficient is negative suggesting that the combination of long reaction times and high concentrations of vitamin C lead to increased NaSS film quality. This is

more likely a false positive than a physically meaningful result since the vitamin C concentration term (x_D) was not significant (P = 0.59).

We next turned to PCA to clarify the conflicting ANOVA results. The first thing to notice is that the first principal component (PC1) shown in figure 4.2 accounts for 91% of the variance in the data compared to only 30 – 35% for the ANOVA. Next, the treatment levels corresponding to short reaction times (B = -1) are relatively tightly clustered and the majority of the data fall below zero on the PC1 scores plot (figure 4.2A). According to the loadings plot (figure 4.2B), negative scores are associated with C, S, and Na from the NaSS layer and positive scores with Ti and O from the substrate.

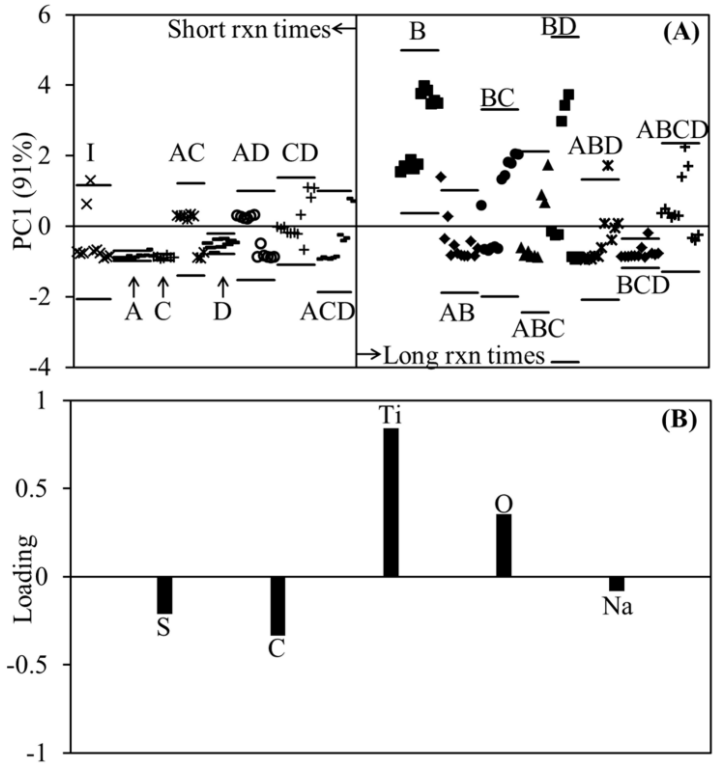

Figure 4.2. PC1 vs. sample type (A) and the corresponding loadings plot (B) for PCA of the factorial design results. The labels in (A) correspond to the factorial design treatment combinations listed in Table 4.2. These results suggest NaSS film quality and reproducibility decreases with increasing ARGET-ATRP grafting reaction time.

Conversely, the scores for the treatment levels corresponding to long reaction times (B = 1) vary widely and much of the data falls above the x-axis. This indicates that with increasing

reaction time the samples move from being more NaSS-like to having more contributions from the substrate, corroborating the ANOVA findings. The position and scatter of the scores for treatment combinations involving long reaction times did not appear to improve with high vitamin C content (BD, ABD, BCD, and ABCD in figure 4.2A), lending credence to the assertion that the $x_B x_D$ two-way interaction term is a false positive. To further support this claim, another ANOVA was performed using the PC1 scores as the response (Tables S4.1 and S4.2 of the supplemental information). In these results the x_B (P = 0.01) and $x_A x_C$ (P = 0.02) terms are retained, while $x_B x_D$ is no longer significant (P = 0.07). Also interesting is that the covariate is no longer significant (P = 0.07) meaning that PCA was able to diminish the effect of the analyzer upgrade. However, PCA was unable to resolve the $x_A x_C$ term and neither statistical analysis method is able to supply mechanistic explanations for the observed results. Therefore, studies were launched to investigate the effect ClSi reaction time (C), ARGET-ATRP reaction time (B), and $CuBr_2$ amount (C) in isolation, and also the AC and BD interactions.

4.4.2 ClSi Reaction Time (A)

While the x_C (ClSi reaction time) term was not found to be significant by either ANOVA or PCA, the $x_A x_C$ (two-way interaction between ClSi reaction time and catalyst amount) was retained by both methods. However, it is unlikely that this result is physically meaningful since these two factors are physically decoupled: i.e., there is no catalyst present during the ClSi functionalization, and the grafting and functionalization steps are prepared in different vials. More likely is that the two-way interaction term is registering the significance of one or both of the main effects, which was obscured by the analyzer upgrade and/or discarded data. In fact, catalyst amount (C) had the most (5) discarded spectra of any treatment combination. It is not surprising that this reduction in the number of data points complicates analysis and interpretation of the factorial design results. Therefore, ClSi reaction time and catalyst amount were studied to determine which of these main effects is significant. The results of the ClSi reaction time study are discussed in this section. Results of the catalyst study are discussed later.

Our hypothesis was that the ClSi film quality—ordering and/or uniformity—increases with increasing reaction time. Corresponding increases in NaSS film quality might be due to a greater availability or access to the surface-bound halide from which the grafting reaction is initiated. While near-monolayer film coverages are likely achieved in a matter of hours, full monolayer

formation and ordering might take a few, or even several days.[109, 110] Therefore, to test this hypothesis ClSi films were synthesized using 1, 3 and 7 day reaction times. Film chemical uniformity, morphology, and ordering were investigated using XPS, AFM, and SFG, respectively. None of these techniques revealed any significant differences between ClSi films synthesized for different lengths of time. However, interesting SFG results were obtained regarding ester ClSi film structure.

SFG spectra in the C-H and ester regions were recorded to compare ester ClSi films prepared on titanium during 1 and 7 days reaction times (figure 4.3). For films such as the ester ClSi, the relative spectral contributions of methyl and methylene vibrations in the C-H region (2800-3000 cm^{-1}) are related to alkane chain conformation.[99, 111] SFG probes IR and Raman active vibrational modes of molecules, which are neither isotropic in arrangement nor have a center of inversion.[112] A perfectly ordered alkane chain with the methylene groups in an all-*trans* conformation does have a center of inversion in between the methylene groups.[99, 113, 114] In such a scenario, the C-H spectral region would be dominated by SFG signals from the terminal methyl vibrations. However, our results show that peaks from methylene vibrations (around 2855 cm^{-1} for symmetric and around 2920 cm^{-1} for asymmetric vibrations) dominate the C-H region, indicating that the alkane chains contain gauche defects. Most importantly, the spectra for 1 and 7 day reaction times overlap almost perfectly showing that no significant change in molecular conformation of the alkane chain is observable by SFG. We also measured the SFG spectra for the ester region (1700-1800 cm^{-1}) and detected the carbonyl stretching peak of the ester group at 1743 cm^{-1}.[115, 116] Since a species must be at least partially ordered to be SFG active, the presence of an SFG signal confirms partial ordering of the ester group.

To quantitatively compare the spectral intensities in the ester region for the 1 and 7 days reaction times, the spectra were fitted with Eq. 3:

$$\chi_{SFG}^{(2)} = \chi_{NR}^{(2)} + \sum_k \frac{A_k}{\omega_{IR} - \omega_k + i\Gamma_k}, \quad \text{(Eq. 3)}$$

where $\chi_{SFG}^{(2)}$ is the second order susceptibility; $\chi_{NR}^{(2)}$ is the non-resonant part; A_k, ω_k, Γ_k are the peak amplitude, peak wavenumber, and damping factor (peak width) for the k_{th} IR and Raman active vibration; and ω_{IR} is the IR wavenumber. The ester peak fits for 1 (blue) and 7 (red) days reaction times are presented in figure 4.3, in which the bar plot displays the value of the peak amplitudes from the two fits. Although the mean values are slightly different, they are within experimental error. This, in conjunction with the striking similarity of the spectra in the C-H

region, provides further evidence that the ClSi films prepared during 1 and 7 days reaction times are similar. As mentioned above, this conclusion is consistent with the results from the XPS and AFM experiments (figures S4.3 and S4.4 of the Supplemental Information). It is therefore unlikely that an increased ClSi reaction time leads to an improved NaSS film quality.

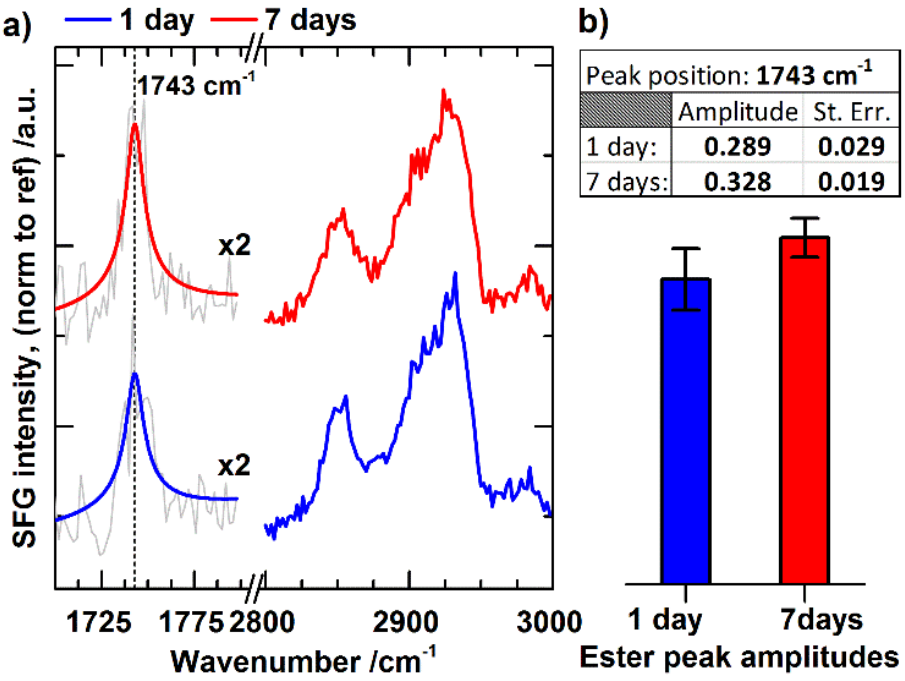

Figure 4.3. SFG spectra of the C-H region (2800 – 2900 cm^{-1}) for ClSi films functionalized for 1 day (blue) and 7 days (red), respectively. For the ester region at 1743 cm^{-1}, the grey traces are averaged data, while the blue and red traces are fits made with Eq. 3. The vertical line at 1743 cm^{-1} denotes the peak position for the fits. For the C-H region only the averaged data are presented. The amplitudes of the fits in the ester region, with error bars showing standard errors of the fits, are included in the table and bar-plot. The data indicate that the films prepared for 1 day and 7 days reaction times are of similar quality.

4.4.3 Grafting Reaction Time (B)

Grafting reaction time was involved in the ANOVA regression model (Eq. 1) as both a main effect (x_B) and interaction term ($x_B x_D$). Both ANOVA and PCA confirmed the significance of the main effect, which was strongly correlated with decreased NaSS film quality leading to

increased titanium signal. For reasons discussed above the significance of the interaction term is thought to be a false positive.

It is surprising that film quality should decrease with increasing grafting reaction time. Assuming the stability of the grafted film under reaction conditions, film properties should remain constant once the reaction reaches completion. NaSS film stability under the reaction (i.e., aqueous) conditions is seemingly a safe assumption since no degradation has been observed in the final step of the grafting procedure, which is to leach any residual catalyst from the films by soaking them in PBS and then water over night. Therefore, we hypothesized that the mechanism for decreased NaSS film quality is hydrolysis of the ester ClSi head group, which may be somehow affected by vitamin C. To test this hypothesis a 2^2 factorial design was performed: functionalized titanium substrates were soaked for 24 or 72 hours in 60/40 H_2O/methanol (the reaction solvent) with or without vitamin C (Table 4.5). Samples were analyzed with XPS before and after soaking, collecting three composition and one high-resolution C1s spectra per sample. The design was replicated twice yielding a total of six composition and two high-resolution C1s measurements per treatment. The compositions and high-resolution C1s results are found in table S4.3 of the supplemental information.

Table 4.5. ClSi hydrolysis 2^2 factorial design: factors and treatment levels.

Factor	Symbol	Low (-1)	High (1)
Vitamin C	A	0 mg	39.5 mg
Soak Time	B	24 hrs	72 hrs

The data were again analyzed using PCA. Two PCs were retained that captured 97% of the variance in the data. The PC1 scores increase with soak time corresponding to an increase in C and a decrease in O, Ti, and the O=C-O high resolution C1s peak (figure 4.4). There is no obvious separation along PC2. The observed decrease in O=C-O signal with reaction time could be a sign of degradation of the ester head group. Loss of the head group would also explain the decrease in oxygen signal. However, a lack of decrease in the Br signal, which would also be expected, combined with the increase in C suggests these trends could be due to attenuation by a contamination layer rather than degradation.

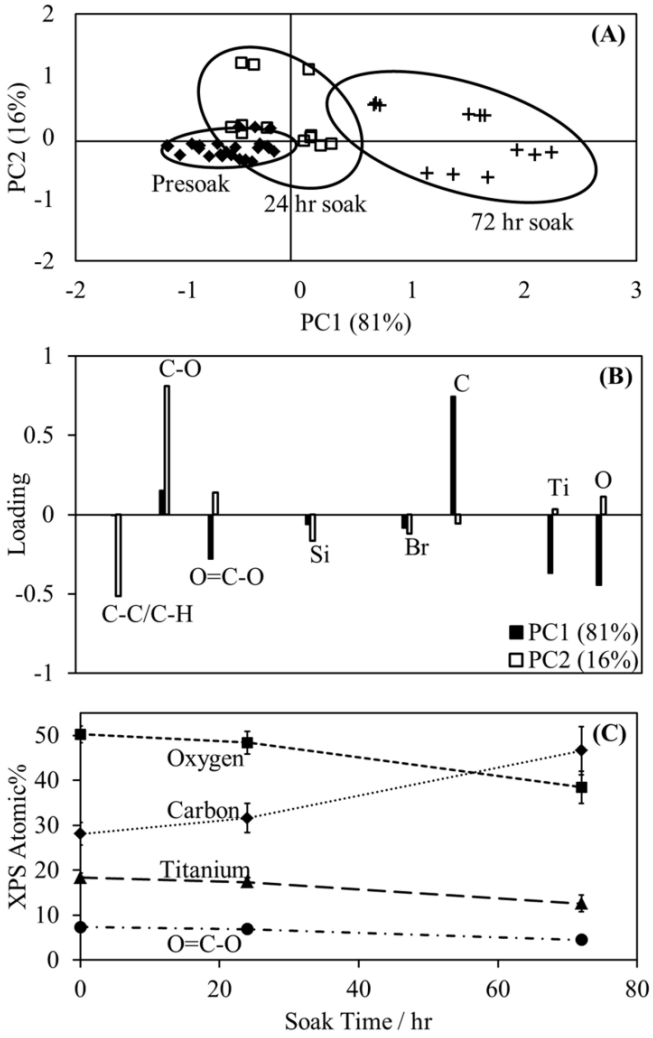

Figure 4.4. Results of a study testing the stability of the ether ClSi ATRP initiator in the reaction solvent. PC1 vs. PC2 scores plot (A) with corresponding loadings (B) and XPS compositions (C) for ester ClSi films soaked in 60/40 H_2O/MeOH for up to 72 hrs. Variability of the ClSi film chemical composition increases with soak time, though it was determined that this was due to adsorption of an adventitious carbon contamination layer.

To confirm this conclusion, and to test for hydrolysis of the siloxane bonds tethering the ClSi initiators to the titanium, the hydrolysis study was expanded to include a thiol and amide version of the same initiator (figure 4.5). Should the siloxane bonds hydrolyze, the amide ClSi films will show signs of degradation while the thiol films will remain unchanged. If the ester group is in fact hydrolyzing, then the thiol films will degrade and the amide ClSi films will remain intact.

The XPS composition and high resolution C1s spectra were analyzed using PCA, which found differences with soak time neither for the thiol nor the amide ClSi (figures S4.5 and S4.6 of the supplemental information). This apparently confirms that the decrease in the O=C-O signal observed for the ester ClSi was due to attenuation by a carbonaceous overlayer—i.e., the XPS ester carbon signal reduction was due to a layer of carbon contamination adsorbed from the ambient—rather than degradation of the ester head group. However, still unexplained is the cause of the NaSS film degradation with increasing grafting reaction time.

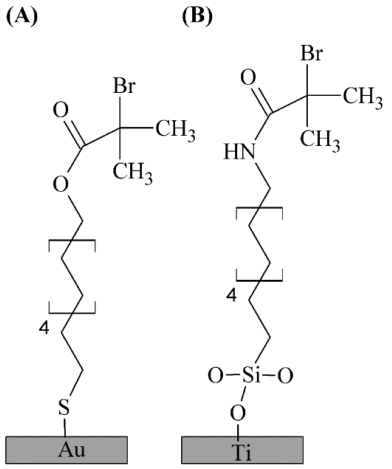

Figure 4.5. Schematic showing the thiol on gold (A) and amide ClSi on titanium (B) ATRP initiators.

The effect of grafting reaction time on NaSS film quality was also assessed for the amide ClSi-functionalized titanium and thiol-functionalized gold substrates. Low (-1) levels were used for all process variables except grafting reaction time, which varied between one and seven days. Two duplicate samples were prepared at each time point and the entire experiment was replicated twice. Three XPS composition spectra were collected for each sample and compiled into a PCA peak list. PC1 scores for the films grafted from gold substrates (figure 4.6A) show very little scatter with grafting reaction time and are associated with S, C, O, and Na—all constituents of NaSS films. This is with the exception of two samples where the grafting reaction appears to have failed, most likely due to improper substrate cleaning leading to the failure of the thiol-functionalization step. From these results, film quality does not appear to be dependent on grafting reaction time for NaSS films grafted from thiol-functionalized gold surfaces. At short reaction times the amide ClSi PC1 scores (figure 4.6B) also show low scatter—minus one errant

sample—and are associated with S, C, and Na from the NaSS film. However, a great deal of scatter is observed for the seven-day grafting reaction time point, with about half the data associated with Ti and O from the substrate. This is in agreement with the ester ClSi results (figure 4.2A), where at longer reaction times the scatter increased drastically and the samples became increasingly associated with the composition of the substrate rather than NaSS. That this was not observed in the hydrolysis study may be that the cause is somehow linked with the catalyst complex. The MSDS lists $CuBr_2$ as corrosive and the authors also observed corrosion of metal utensils used to weigh out the $CuBr_2$ powder. Thus, even though in low concentrations, it may be that the catalyst damages the titanium substrates over time. As a noble metal, gold would be resistant to such corrosive effects, explaining why no NaSS film degradation was observed on these substrates. Further study is needed to confirm this hypothesis.

4.4.4 $CuBr_2$ (C)

In the ANOVA regression model (Eq. 1), $CuBr_2$ is represented as the two-way interaction between ester ClSi reaction time and catalyst amount ($x_A x_C$). It is correlated with decreased NaSS film quality and the corresponding increased titanium signal. Both PCA and ANOVA confirm this term as significant. As previously discussed, it is more likely that the two-way interaction term is registering the significance of one or both of the main effects, which was obscured by the analyzer upgrade and/or discarded data. Having already tested ester ClSi reaction time (A) in isolation, we next studied the effect of $CuBr_2$ amount (C) on NaSS film quality. Our hypothesis was that with increasing catalyst the number of exposed radicals, and the total time that each radical is exposed, also increases. This in turn leads to decreased reaction control resulting in non-uniform NaSS films. To test this hypothesis NaSS grafting reactions were carried out using low (-1) levels for all process variables except for $CuBr_2$, which varied between 0.5 – 2 mg cm^{-2}. Chemical uniformity was characterized via XPS survey and high-resolution C1s scans. Three survey and one high-resolution scan were collected per sample. Lateral uniformity and film thickness were characterized via AFM, with three topography images obtained and three scratch tests performed per sample. Two duplicate samples were prepared per treatment, and the entire study was replicated twice resulting in a total of four samples per treatment.

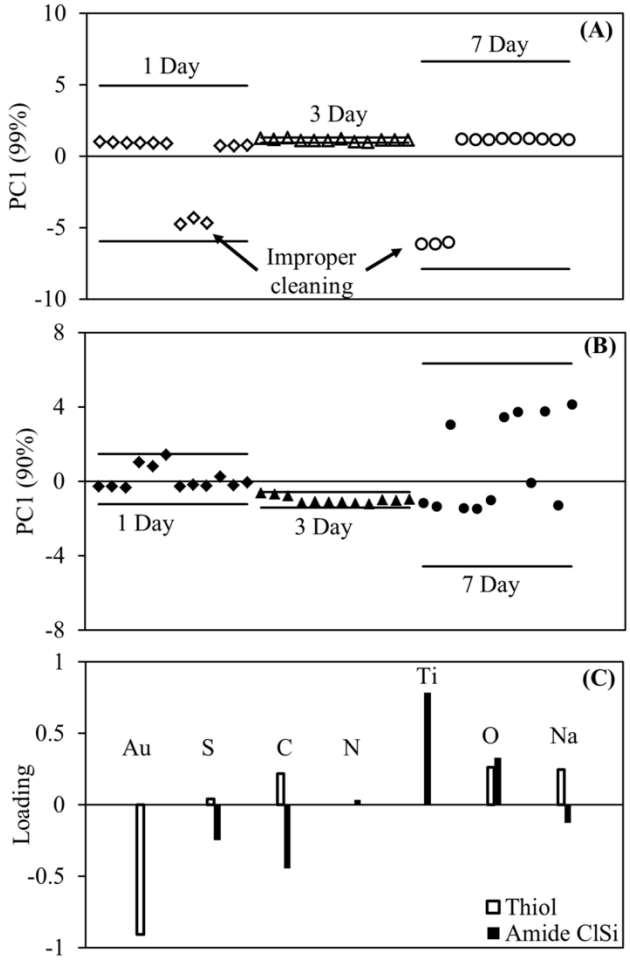

Figure 4.6. Results of a study testing the effect of reaction time on NaSS film quality for films grafted from thiol (on gold) and amide ClSi (on titanium) ATRP initiators (figure 4.5). PC1 vs. sample scores plots for NaSS films on gold using the thiol ATRP initiator (A), and on titanium using the amide ClSi ATRP initiator (B) for grafting reaction times up to 7 days. The corresponding loadings are in (C). Except for two improperly cleaned substrates, NaSS film quality appears constant with reaction time on gold, while quality and reproducibility decreases with increasing reaction time when grafted from the amide ClSi initiator on titanium.

The XPS composition results (figure 4.7A) show a trend of increasing titanium and decreasing sulfur with increasing catalyst. This suggests decreasing NaSS film thickness or uniformity with increasing $CuBr_2$. The AFM scratch tests (figure 4.7B) confirm that film thickness decreases with increasing catalyst concentration, while the topography results (figure 4.8) confirm the film uniformity does not appear to be a function of $CuBr_2$ concentration.

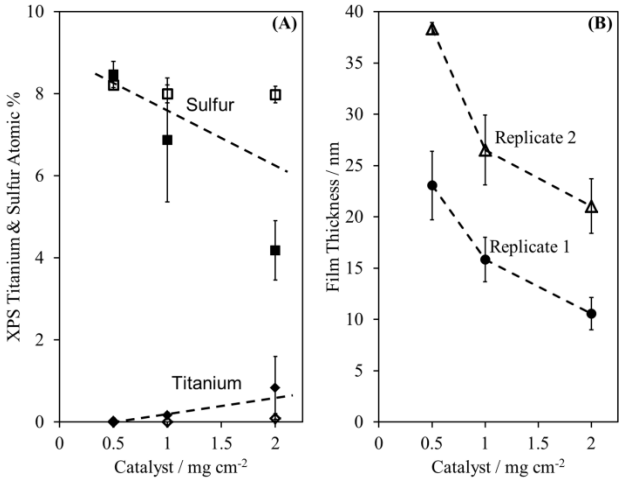

Figure 4.7. XPS titanium and sulfur composition vs. $CuBr_2$ per nominal cm^2 of initiator-functionalized surface area for both replicates (A and B, respectively). For both panels, data from replicate 1 and 2 are represented by closed and open symbols, respectively. These results show that NaSS film thickness decreases with increasing catalyst amount.

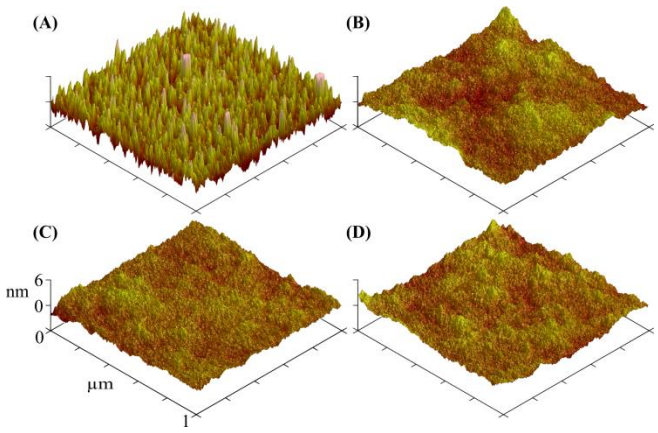

Figure 4.8. Representative AFM images of NaSS films grown with 0 (A), 0.5 (B), 1 (C), and 2 mg (D) $CuBr_2$ per nominal cm^2 of initiator-functionalized surface area. Average ± standard deviation RMS roughness values for each treatment are as follows: 1.9 ± 0.1 nm (0 mg cm^{-2} $CuBr_2$), 0.7 ± 0.2 nm (0.5 mg cm^{-2} $CuBr_2$), 0.7 ± 0.1 nm (1 mg cm^{-2} $CuBr_2$), 0.9 ± 0.2 nm (2 mg cm^{-2} $CuBr_2$).

Our hypothesized reason for the thinner films is that with increasing catalyst the number and frequency of radical activation events also increases. This leads to an increased number of

termination events between neighboring polymer chains, which in turn depletes the dormant polymer state and causes a buildup of deactivator ($CuBr_2$/bpy, in this case).[30] Therefore, we recommend using the minimum amount of $CuBr_2$ necessary, which for this system seems to be no more than 0.5 mg per nominal cm^2 of initiator-functionalized surface area.

4.5 Summary and Conclusions

A 2^4 factorial design was performed to optimize the ARGET-ATRP grafting of NaSS from titanium. The factors varied were: (A) ester ClSi initiator reaction time; (B) grafting reaction time; (C) $CuBr_2$ amount; and (D) reducing agent (vitamin C) amount. The factors and levels are listed in table 4.1. The design matrix is found in table 4.2. Films were characterized using XPS and the factorial design analyzed using ANOVA and PCA. The ANOVA results and regression model are found in table 4.3 and equation 1. The significant factors are B (grafting reaction time; P = 4.5E-3), AC (the two-way interaction between ester ClSi reaction time and $CuBr_2$ amount; P = 0.02), and BD (the two-way interaction between grafting reaction time and vitamin C amount; P = 0.04). For reasons discussed above—including the possibility of the two-way interaction terms being retained due to false positives—interpretation of these results and regression model is somewhat problematic. Therefore, PCA was used to provide additional insight into the NaSS grafting process. Additional studies were done to investigate the significant effects identified by ANOVA and PCA, as well as to gain some understanding of their influence on NaSS film quality. The conclusions are as follows: (1) no chemical, structural, or morphological changes were detected with ester ClSi reaction time (A) suggesting that this effect has little discernable influence on NaSS film quality. SFG spectra show some degree of ordering in the ClSi films on the titanium surfaces, but the ClSi film quality does not improve beyond the first day of reaction time. (2) NaSS film quality decreases with grafting reaction time for both ester and amide ClSi initiators, but not for films grafted from thiol initiators on Au. This may be due to the $CuBr_2$ corroding the titanium substrate. No decrease in film quality is observed on Au because noble metals are more resistant to corrosion. (3) In addition to potentially corroding metal surface, NaSS film thickness decreased with increasing $CuBr_2$ concentration.

From these conclusions, we suggest using the following reaction conditions to optimize grafted film quality: (1) Shorter ATRP-initiator surface functionalization reaction times, although no deleterious effects were detected at longer times. (2) Minimum ($\leq$ 24 hr for this system) grafting reaction times. (3) Minimum ($\leq$ 0.5 mg cm^{-2} for this system) $CuBr_2$

concentration. (4) Sufficient excess of vitamin C, as no deleterious effects were detected with increasing concentrations.

4.6 Acknowledgements

This study was supported by NIH grant EB-002027 to NESAC/BIO. We thank Professor Veronique Migonney for stimulating discussions about the preparation and biological applications of grafted NaSS films. We also gratefully acknowledge Professor Linda Boyle for her helpful discussions regarding the proper handling of the XPS analyzer upgrade in the factorial design ANOVA.

4.7 Supplemental Information

Experimental Design and Analysis of ARGET-ATRP Experimental Conditions for Grafting Sodium Styrene Sulfonate from Titanium Substrates

Rami N. Foster
Department of Chemical Engineering, University of Washington – Seattle, and National ESCA and Surface Analysis Center for Biomedical Problems, Seattle, WA 98195

Patrik K. Johansson
Department of Bioengineering, University of Washington – Seattle, and National ESCA and Surface Analysis Center for Biomedical Problems, Seattle, WA 98195

Nicole R. Tom
Department of Chemical Engineering, Carnegie Mellon University, Pittsburg, PA 15213

Patrick Koelsch
Department of Bioengineering, University of Washington – Seattle, and National ESCA and Surface Analysis Center for Biomedical Problems, Seattle, WA 98195

David G. Castner
Departments of Chemical Engineering and Bioengineering, University of Washington – Seattle, and National ESCA and Surface Analysis Center for Biomedical Problems, Seattle, WA 98195

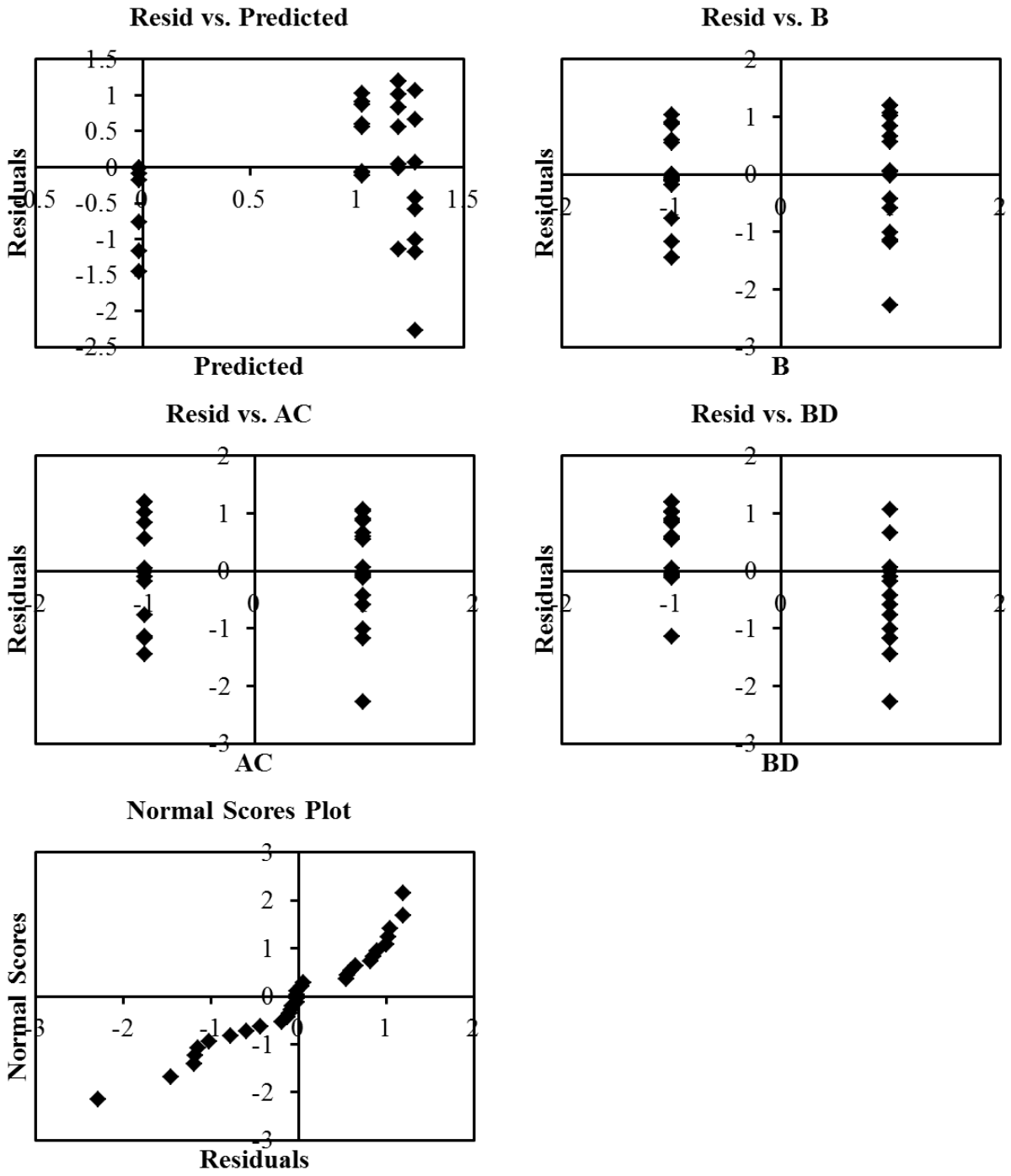

Figure S4.1. Residuals plots for the model in Eq. 1 using √Ti as the response.

Table S4.1. Experimental conditions and results with PC1 as the response. PCA was run using average compositions for each trial number, which as stated in section G of the Materials and Methods is—except in cases where spectra were discarded due to sample charging—six spectra per replicate for a total of twelve spectra per treatment combination.

Trial #	ClSi Reaction Time (hrs)		ARGET-ATRP Reaction Time (hrs)		$CuBr_2$ Catalyst (mg)		Vitamin C (mg)		Covariate	Response
	A		B		C		D			PC1
1	-1	(24)	-1	(24)	-1	(2)	-1	(79)	1	0.2315
2	1	(72)	-1	(24)	-1	(2)	-1	(79)	-1	-0.9337
3	-1	(24)	1	(72)	-1	(2)	-1	(79)	-1	1.6387
4	1	(72)	1	(72)	-1	(2)	-1	(79)	1	0.0919
5	-1	(24)	-1	(24)	1	(4)	-1	(79)	-1	-0.9420
6	1	(72)	-1	(24)	1	(4)	-1	(79)	1	0.2402
7	-1	(24)	1	(72)	1	(4)	-1	(79)	1	-0.3119
8	1	(72)	1	(72)	1	(4)	-1	(79)	-1	-0.7819
9	-1	(24)	-1	(24)	-1	(2)	1	(158)	-1	-0.5460
10	1	(72)	-1	(24)	-1	(2)	1	(158)	1	0.2295
11	-1	(24)	1	(72)	-1	(2)	1	(158)	1	-0.2648
12	1	(72)	1	(72)	-1	(2)	1	(158)	-1	-0.9545
13	-1	(24)	-1	(24)	1	(4)	1	(158)	1	-0.1610
14	1	(72)	-1	(24)	1	(4)	1	(158)	-1	-0.9422
15	-1	(24)	1	(72)	1	(4)	1	(158)	-1	-0.9098
16	1	(72)	1	(72)	1	(4)	1	(158)	1	0.2939
17	-1	(24)	-1	(24)	-1	(2)	-1	(79)	1	-0.7962
18	1	(72)	-1	(24)	-1	(2)	-1	(79)	1	-0.8143
19	-1	(24)	1	(72)	-1	(2)	-1	(79)	1	3.6148
20	1	(72)	1	(72)	-1	(2)	-1	(79)	1	-0.7180
21	-1	(24)	-1	(24)	1	(4)	-1	(79)	1	-0.9177
22	1	(72)	-1	(24)	1	(4)	-1	(79)	1	-0.8479
23	-1	(24)	1	(72)	1	(4)	-1	(79)	1	1.7046

24	1	(72)	1	(72)	1	(4)	-1	(79)	1	1.0726
25	-1	(24)	-1	(24)	-1	(2)	1	(158)	1	-0.5007
26	1	(72)	-1	(24)	-1	(2)	1	(158)	1	-0.7657
27	-1	(24)	1	(72)	-1	(2)	1	(158)	1	1.7905
28	1	(72)	1	(72)	-1	(2)	1	(158)	1	0.2549
29	-1	(24)	-1	(24)	1	(4)	1	(158)	1	0.4732
30	1	(72)	-1	(24)	1	(4)	1	(158)	1	0.1723
31	-1	(24)	1	(72)	1	(4)	1	(158)	1	-0.5862
32	1	(72)	1	(72)	1	(4)	1	(158)	1	0.8860

Table S4.2. ANOVA results using PC1 as the response.

Source	**SS**	**DOF**	**MS**	**F_o**	**F_{crit}**	**P**	**Significant?**
A	1.55	1	1.55	2.91	4.60	0.11	
B	5.82	1	5.82	10.96	4.60	0.01	yes
C	0.30	1	0.30	0.57	4.60	0.46	
D	0.29	1	0.29	0.55	4.60	0.47	
AB	1.14	1	1.14	2.14	4.60	0.17	
AC	3.46	1	3.46	6.52	4.60	0.02	yes
AD	1.44	1	1.44	2.72	4.60	0.12	
BC	0.80	1	0.80	1.51	4.60	0.24	
BD	2.28	1	2.28	4.30	4.60	0.06	
CD	0.30	1	0.30	0.56	4.60	0.47	
ABC	2.44	1	2.44	4.60	4.60	0.05	
ABD	2.04	1	2.04	3.84	4.60	0.07	
ACD	0.48	1	0.48	0.90	4.60	0.36	
BCD	0.01	1	0.01	0.02	4.60	0.90	
ABCD	0.54	1	0.54	1.02	4.60	0.33	
Covariate	2.10	1	2.10	3.96	4.60	0.07	
Blocks	2.02	1	1.55	3.81	4.60	0.07	
Error	7.43	14	0.53				
Total	34.42	31					

$$PC1 = 0 + 0.43x_B + 0.33x_Ax_C \text{ (Eq. S1)}$$

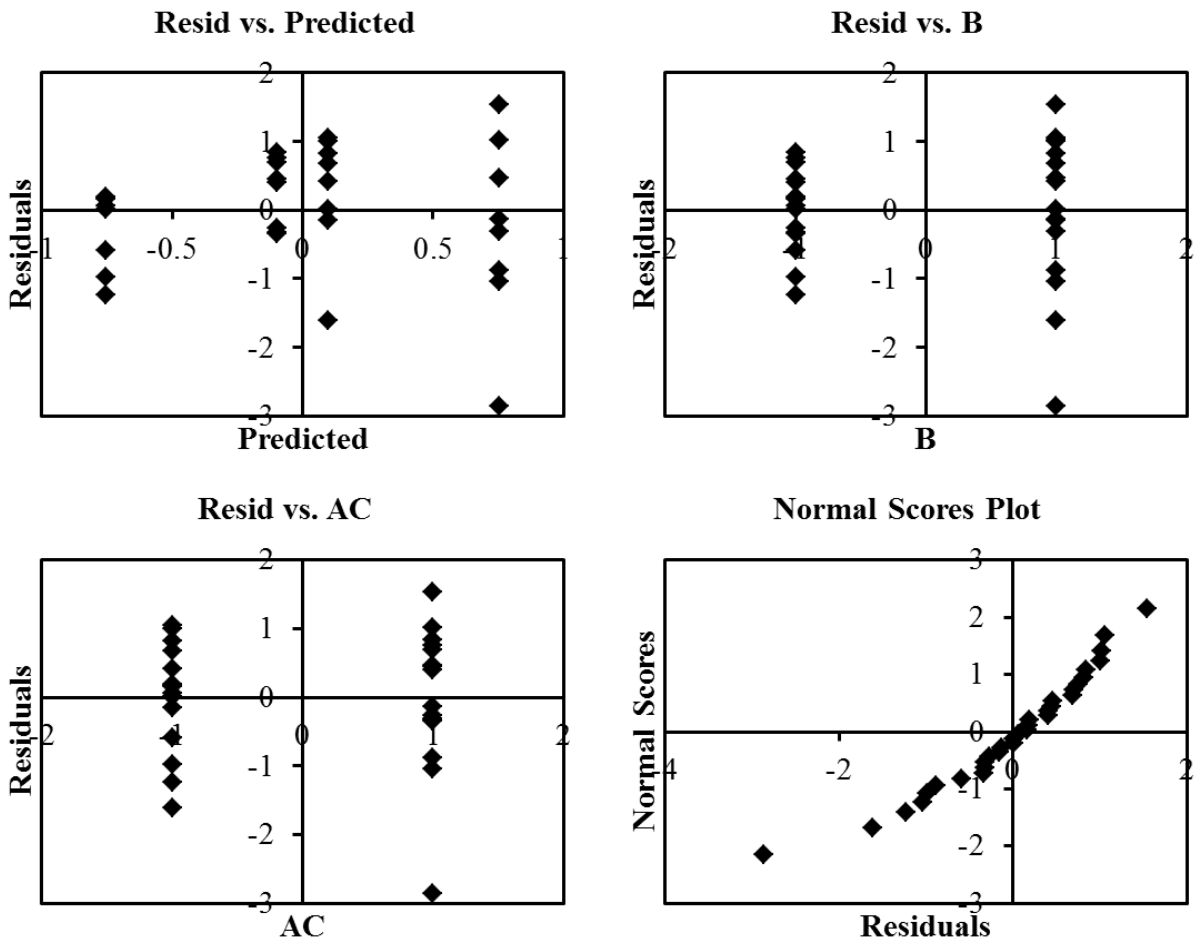

Figure S4.2. Residuals plots for the regression model using PC1 as the response (Eq. S1).

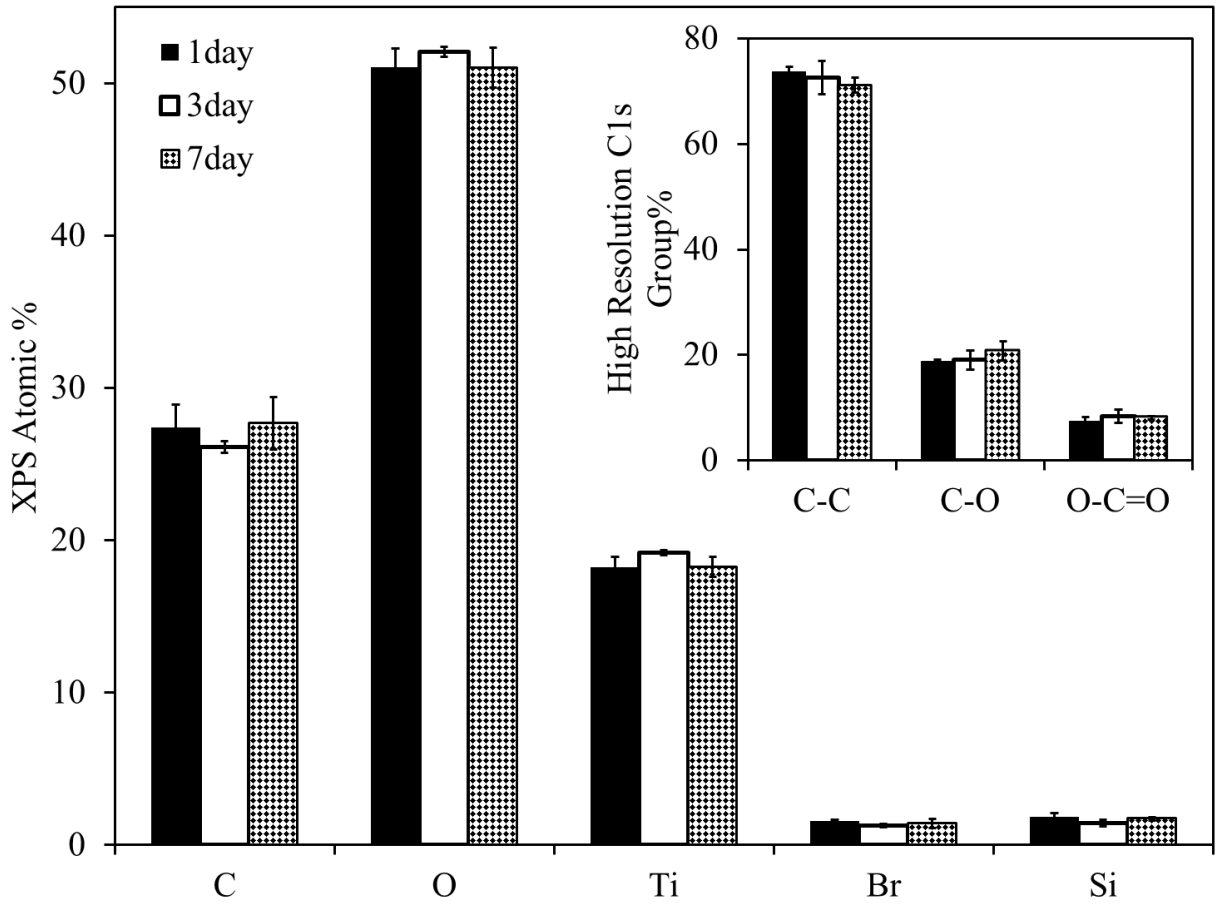

Figure S4.3. XPS Compositions and high resolution C1s group% with ClSi reaction time.

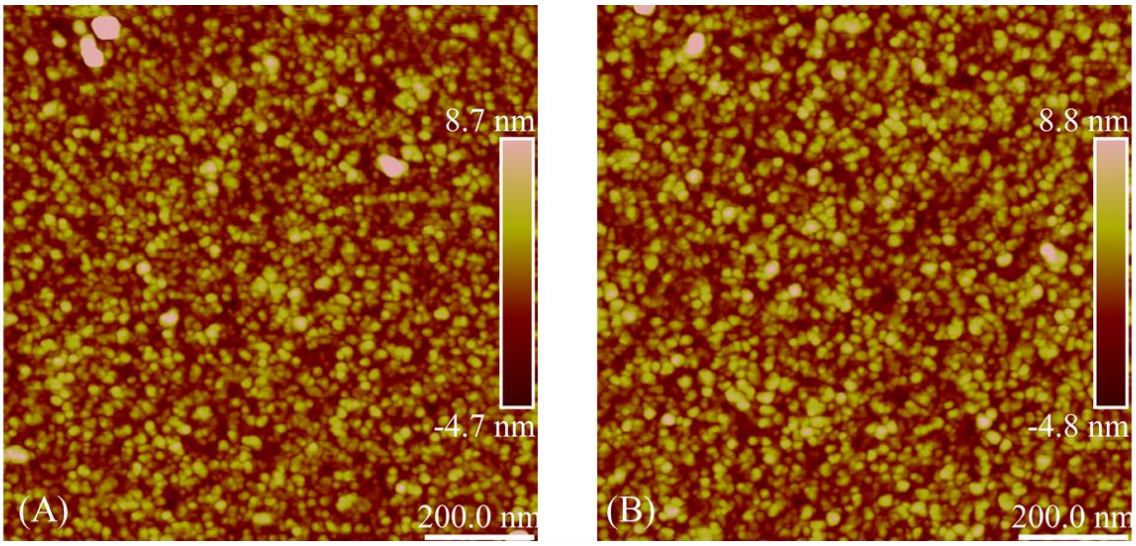

Figure S4.4. AFM of ClSi films on titanium after 1 day (A) and 7 day (B) reaction times.

Table S4.3. XPS compositions for ClSi films before and after soaking according to the treatments listed in Table 4.5. Reported values are the average ± standard deviation of three spots on two samples, except for the ClSi film values which are the average ± standard deviation of three spots on all eight samples before treatment.

XPS Atomic Percent					
	ClSi Film	1-Day Soak with Vitamin C	1-Day Soak	3-Day Soak with Vitamin C	3-Day Soak
Br_{3d}	1.5 ± 0.2	1.0 ± 0.2	1.1 ± 0.1	1.1 ± 0.1	0.9 ± 0.1
C_{1s}	28.1 ± 2.5	32.5 ± 3.4	30.8 ± 3.1	42.9 ± 4.5	50.4 ± 3.1
O_{1s}	50.3 ± 1.9	48.0 ± 3.0	48.9 ± 2.1	40.5 ± 3.3	36.4 ± 2.5
Si_{2p}	1.8 ± 0.3	1.4 ± 0.4	1.6 ± 0.2	1.5 ± 0.4	1.1 ± 0.2
Ti_{2p}	18.4 ± 1.0	17.1 ± 0.9	17.6 ± 1.1	13.9 ± 1.6	11.2 ± 0.8
High Resolution C1s Group Percent					
C-C/C-H	73.1 ± 1.5	67.2 ± 8.0	71.1 ± 0.5	72.0 ± 6.7	71.3 ± 3.8
C-O	19.5 ± 1.5	25.8 ± 6.6	22.0 ± 0.5	23.0 ± 5.6	24.6 ± 3.0
O-C=O	7.4 ± 0.2	7.0 ± 1.4	6.9 ± 0.1	5.0 ± 1.1	4.1 ± 0.8

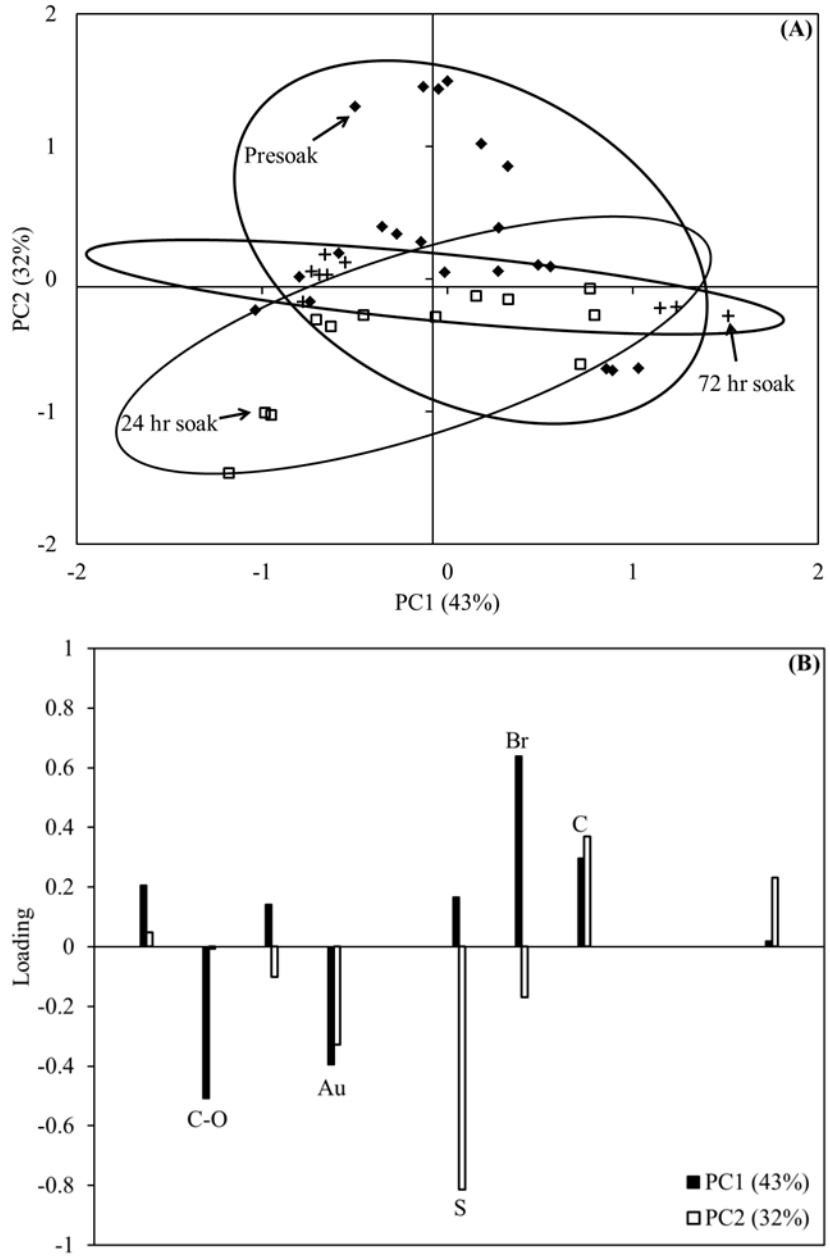

Figure S4.5. PC1 vs. PC2 scores plot (A) with corresponding loadings (B) for thiol ATRP initiator films soaked in 60/40 H_2O/MeOH for up to 72 hrs.

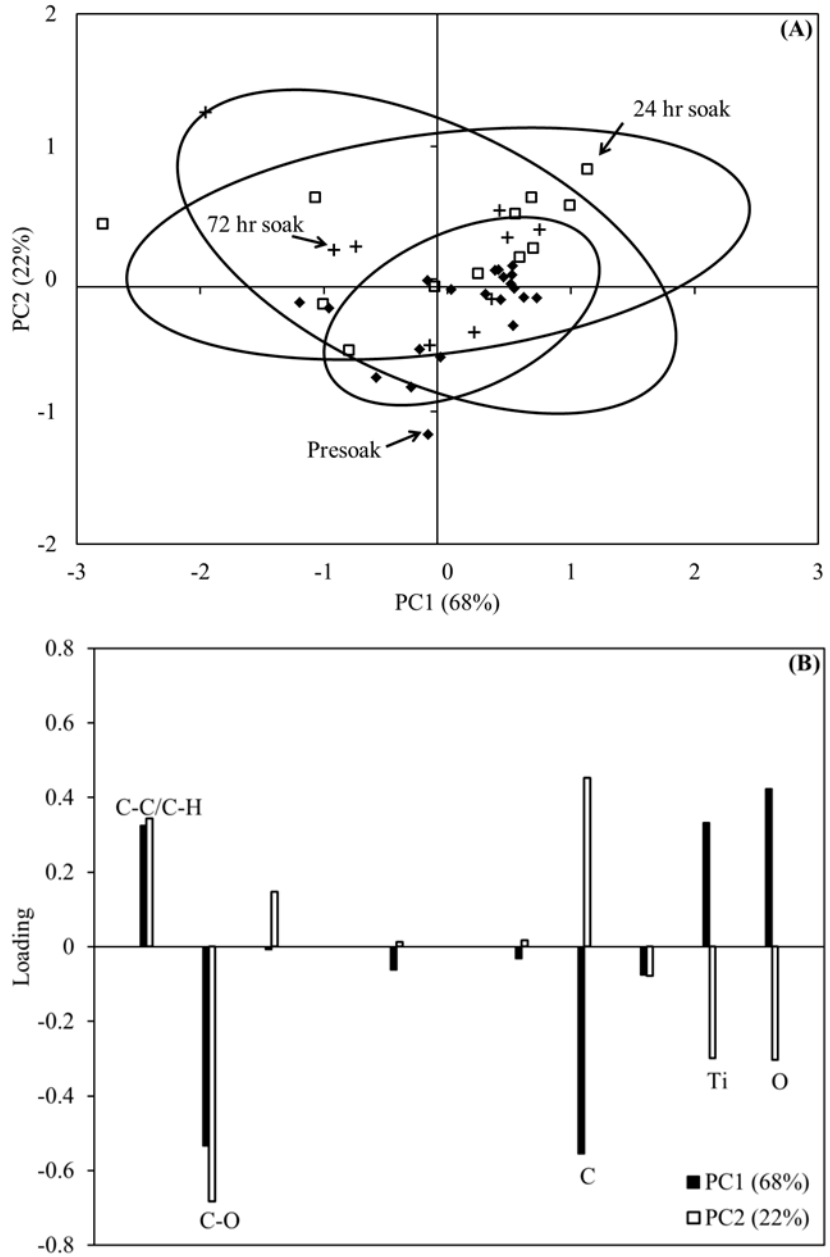

Figure S4.6. PC1 vs. PC2 scores plot (A) with corresponding loadings (B) for amide ClSi ATRP initiator films soaked in 60/40 H_2O/MeOH for up to 72 hrs.

Table S4.4. ClSi hydrolysis 2^2 factorial design ANOVA.

Source	SS	DOF	MS	F_o	F_{crit}	P	Significant?
A	0.47	1	0.47	5.4	10.1	0.10	
B	11.54	1	11.54	133	10.1	1.4E-3	yes
AB	0.32	1	0.32	3.7	10.1	0.15	
Blocks	2.65	1	2.65	30	10.1	0.01	yes
Error	1.16	3	0.39				
Total	16.14	7					

5. ToF-SIMS and XPS Characterization of Protein Films Adsorbed onto Bare and Sodium Styrene Sulfonate Grafted Gold Substrates

Rami N. Foster, Elisa T. Harrison
Department of Chemical Engineering, University of Washington – Seattle, and National ESCA and Surface Analysis Center for Biomedical Problems, Seattle, WA 98195

David G. Castner
Departments of Chemical Engineering and Bioengineering, University of Washington – Seattle, and National ESCA and Surface Analysis Center for Biomedical Problems, Seattle, WA 98195

5.1 Abstract

In this study we characterized adsorbed bovine serum albumin (BSA), bovine fibrinogen (Fgn), bovine immunoglobulin G (IgG), and bovine plasma films on bare and sodium styrene sulfonate (NaSS)-grafted gold. Protein adsorption isotherms were measured using XPS to follow changes in surface nitrogen composition with increasing protein solution concentration. Using a combination of time-of-flight secondary ion mass spectrometry (ToF-SIMS), principal component analysis (PCA), and visual molecular dynamics (VMD) differences in adsorbed protein structure between both surfaces were investigated. Principal component (PC) modeling was also used to qualitatively describe changes in bovine plasma adsorbed films with time. From the XPS isotherms we found that, at low solution concentrations, all three proteins and plasma adsorb more readily with higher affinity onto gold compared to NaSS surfaces. However, at higher concentrations NaSS surfaces adsorb the same (for plasma) or more (for BSA and Fgn) total protein than gold. This may be because proteins that adsorb onto NaSS undergo structural rearrangements over time, increasing the number of contacts with the surface and resulting in a larger fraction of irreversibly adsorbed species. The only protein that was adsorbed in lower amounts on NaSS compared to gold surfaces was IgG. This is likely because IgG adopts a highly denatured, high-surface area conformation on NaSS. Still, with the exception of BSA and plasma adsorption onto gold, the protein adsorption process on neither surface appeared to have saturated at the highest protein solution concentration studied. PCA of just the amino acid ToF-SIMS mass fragments distinguished between the same protein adsorbed onto NaSS and gold surfaces, and also between proteins adsorbed from different solution concentrations onto the same surface. This suggests that proteins adsorb differently on NaSS and gold, and that the adsorbed protein structure changes with surface concentration. Therefore, using peak ratios for buried/surface amino acids for each protein, the degree of denaturation was determined for each surface. It was found that proteins denature more on NaSS than gold. Also, peak ratios for non-uniformly distributed amino acids were used to suggest potential surface structures for BSA and IgG adsorbed onto NaSS. From the PC modeling results the adsorbed plasma films on NaSS appear to start out more BSA-like and become more Fgn-like with increasing adsorption time. Similarly, the adsorbed plasma films on gold appear to start out more IgG-like and become more Fgn-like with increasing adsorption time. However, the PC models included only three proteins, where plasma is a complex mixture of hundreds of proteins. Therefore, while both gold and

NaSS appear to adsorb more Fgn with time, further study is required to confirm that this is representative of the final state of the adsorbed plasma films.

5.2 Introduction

The performance of biomedical implants is largely determined by how proteins interact with the implant surface.[11, 39, 117] This is because proteins are the first biomolecule adsorb to the surface, and all subsequent interactions between the body and the implant are mediated by the adsorbed protein layer.[9, 118, 119] As such, understanding how proteins interact with different surface chemistries is important to aid development of next-generation biomaterials.

Polymer grafting is an effective way of making controlled changes to surface chemistry.[120, 121] Furthermore, advancements in polymer chemistry, such as the development of ARGET ATRP (Activators are continuously ReGenerated by Electron Transfer Atom Transfer Radical Polymerization), have simplified the grafting process and greatly expanded the available combination of polymers and functional groups with which to modify surfaces.[30, 33]

Surface functionalization with sodium styrene sulfonate (NaSS) has recently been shown to increase proliferation and adhesion of fibroblasts,[14] MG63 osteoblast-like cells,[15-17] and human mandibular osteoblasts[18] in vitro, with promising increases in osseointegration shown in vivo.[18-20] We hypothesize that an observed increase in osseointegration is due the ability of NaSS to preferentially adsorb specific plasma proteins in an orientation and conformation that promotes formation of new bone. We have recently developed a procedure for grafting NaSS from a number of oxide and metal surfaces to test this hypothesis.[50, 122] Beyond the potential for biomedical application, NaSS is an interesting system as it allows us to study protein interaction with a very specific surface chemistry: namely, sulfonated styrene with a sodium counter ion. This can be used as a platform for future work to study the effect of, for example, changing the counter ion from sodium to potassium, or the head group from a negatively charged sulfonate to a positively charged quaternary amine. Thus, controlled changes in surface chemistry can be related to the properties of adsorbed protein films in a continued effort to investigate the important factors controlling protein-surface interactions.

In the current work, we investigate the adsorption of bovine serum albumin (BSA), bovine fibrinogen (Fgn), bovine immunoglobulin G (IgG), and bovine plasma onto bare and NaSS-grafted gold surfaces. Protein adsorption isotherms were measured using XPS to follow changes in surface nitrogen composition with increasing protein solution concentration (5, 25, and 100

μg/ml). Since gold and NaSS do not contain nitrogen, surface nitrogen composition is directly related to the amount of protein adsorbed. A combination of time-of-flight secondary ion mass spectrometry (ToF-SIMS), principal component analysis (PCA), and visual molecular dynamics (VMD) was used to investigate differences in adsorbed protein structure between both surfaces. Principal component (PC) modeling was used to qualitatively describe changes in bovine plasma films with time.

5.3 Experimental

5.3.1 Materials

Silicon wafers (Silicon Valley Microelectronics Inc., San Jose, CA) were diced into 1×1 cm^2 substrates using a diamond saw. Gold substrates were fabricated by depositing a 5 nm titanium adhesion layer followed by a 100 nm gold layer onto the diced silicon substrates via electron-beam deposition at room temperature and pressures < 1 $x10^{-6}$ torr. Methanol, acetone, dichloromethane, phosphate buffered saline (PBS; 0.01 M phosphate, 0.138 M sodium chloride, 0.0027 M potassium chloride, pH 7.4), bovine serum albumin (BSA) (≥ 99%), bovine fibrinogen (Fgn) (65-85%), bovine immunoglobulin G (IgG) (≥ 95%), bovine plasma, Cu(II) bromide (>99.0%), 2,2'-bipyridine (bpy) (≥99%), vitamin C (≥98%), and sodium styrene sulfonate (NaSS) (≥90%) were all purchased from Sigma. Ethanol (200 proof) was purchased from Decon Laboratories. Bromoisobutyrate undecyl disulfide (99%) was purchased from Asemblon. All chemicals were used as received.

5.3.2 Substrate cleaning and ATRP-initiator functionalization

Prior to the electron-beam deposition, substrates were cleaned by sonicating twice for 5 minutes in each of dichloromethane, acetone, and MeOH. The electron-beam deposited gold substrates were rinsed with ethanol and immersed in a 1 mM solution of bromoisobutyrate undecyl disulfide in ethanol for 18 – 24 hrs. The substrates were then rinsed with ethanol, sonicated for 1 – 3 minutes to remove any unbound bromoisobutyrate undecyl disulfide, and rinsed once more with ethanol. Gold functionalization reactions were performed at room temperature in N_2-backfilled glass test tubes stoppered with rubber septa—one sample per test tube.

5.3.3 NaSS Grafting

A fresh batch of NaSS-grafted samples was prepared for each protein adsorption experiment. A batch typically consisted of 16 1×1 cm^2 functionalized gold substrates and the grafting reactions were performed in 20-ml glass scintillation vials, with two substrates per vial. To each reaction vial was added 500 mg of NaSS monomer and 1.2 ml 18-Ω DI H_2O. We previously established that NaSS film quality is sensitive to catalyst amount.[122] Therefore, to minimize weighing error, the catalyst solution was prepared in bulk for the entire batch. For 16 samples, this entailed dissolving 8 mg $CuBr_2$ and 28 mg bpy (1:2 $CuBr_2$:bpy) in 19.2 ml methanol and 9.6 ml 18-Ω DI H_2O. The catalyst solution (3.6 ml) was then added to each reaction vial so that the final concentration of $CuBr_2$ and bpy was 0.5 and 1.4 mg per nominal cm^2 functionalized surface area. At this point, the reaction vials were often briefly sonicated to fully dissolve the NaSS monomer. Two functionalized substrates were then added to each vial and the grafting reaction begun upon addition of 79 mg vitamin C dissolved in 1.2 ml 18-Ω DI H_2O (39.5 mg vitamin C per nominal cm^2 functionalized surface area). The vitamin C solution was also prepared in bulk—632 mg in 9.6 ml 18-Ω DI H_2O. The total solvent volume was 6 ml (60/40 H_2O/MeOH). Care was taken that the substrates stayed face up and did not overlap each other. The reaction vials were capped and sealed with parafilm to minimize additional oxygen leaking into the system. After 18-24 hrs, the substrates were rinsed with 18-Ω DI H_2O, soaked in PBS for a few hours, and then soaked in 18-Ω DI H_2O overnight to remove any residual catalyst and monomer. Finally, the grafted substrates were rinsed again with 18-Ω DI H_2O, gently dried with a stream of N_2, and analyzed immediately via XPS to ensure that the reaction had succeeded and the film quality was sufficient for further use. Detailed characterization of these films has been presented elsewhere.[50, 122]

5.3.4 Protein Adsorption

Substrates were hydrated for 30 min. in degassed PBS (pH = 7.4) prior to adsorption. The single-component protein adsorption experiments were performed for 2 hours at solution concentrations of 0, 5, 25, and 100 µg/ml to establish adsorption isotherms. Plasma adsorption experiments were performed at a solution concentration of 100 µg/ml for times varying between 5 and 120 min. All adsorption experiments were performed in 24-well plates in degassed PBS at 37^{o}C. Two duplicate samples were prepared at each treatment, and each experiment was replicated twice, yielding four samples for each adsorption concentration (for the single-

component experiments) or time point (for the plasma adsorption experiments). Samples were immediately stored under vacuum and analyzed via XPS and then ToF-SIMS on the two subsequent days.

5.3.5 X-Ray Photoelectron Spectroscopy (XPS)

XPS compositions were determined from the average of three spots on four samples, totaling 12 spots per treatment. The data were acquired on an SSI S-Probe instrument (Surface Science Instruments, Mountain View, California) with a 0^o photoelectron takeoff angle (TOA), defined as the angle between the surface normal and the axis of the analyzer lens. All spectra were acquired using a monochromatic Al $K\alpha_{1,2}$ X-ray source (hv = 1486.6 eV). Survey (0–1100 eV) and detailed scans were collected with analyzer pass energy of 150 eV and a 100 ms dwell time. The survey step size was 1 eV, while 0.4 eV was used for detail scans. All samples were isolated from the instrument using double-sided tape and run as insulators. Charge neutralization was achieved using a low-energy electron flood gun. Binding energy scales were calibrated by setting the CH_x peak in the C_{1s} region to 284.6 eV, and a linear background was subtracted for all peak area quantifications. The peak areas were normalized by the manufacturer supplied sensitivity factors, and atomic compositions calculated using Hawk Data Analysis 7 (Service Physics, Inc., Bend, Oregon).

5.3.6 Time-of-flight secondary ion mass spectrometry (ToF-SIMS)

Positive and negative secondary ion spectra and images were acquired on a TOF.SIMS 5-100 instrument (ION-TOF, Münster, Germany) using a pulsed 25 keV Bi_3^+ primary ion beam under static conditions (primary ion dose < 10^{12} ions/cm^2). Five positive and three negative spectra were collected from 100 × 100 μm^2 regions for each sample. Spectra were acquired in high-current bunch (high mass resolution) mode, over a range of 0–800 m/z at a mass resolution ($m/\Delta m$) between 4000 and 8000. Positive spectra were mass calibrated using CH_3^+, $C_2H_3^+$, and $C_3H_5^+$ peaks, and negative spectra were calibrating using CH^-, OH^-, C_2H^-, C_3^-, C_4H^-, and C_5^- peaks. Mass calibration errors were below 20 ppm.

5.3.7 Principal component analysis (PCA)

PCA of the ToF-SIMS data, previously described in detail,[74-76] is a multivariate analysis technique that is used to identify principal sources of variation between sample spectra. Three

peak lists were compiled and imported into a series of scripts written by NESAC/BIO for MATLAB[77, 78] (MathWorks, Inc., Natick, MA): all positive peaks, all negative peaks, and a peak list containing amino acid-derived mass fragments.[123] Data sets were also normalized by the sum of selected peaks, mean centered, and square-root transformed to ensure that variance within the data set was due to differences in sample variances rather than in sample means. Due to detector saturation during acquisition, the sodium peak was removed from all positive peak lists prior to any data pretreatment. Obvious contaminant (e.g., PDMS, Cu, I) and isotope peaks were also typically removed prior to analysis.

5.4 Results/Discussion

5.4.1 Concerns Regarding NaSS Sodium Levels and Resulting Matrix Effects

Typically, ToF-SIMS spectra with sodium (m/z 22.99) secondary ion counts ≥ 1% of the total counts are discounted from analysis. High sodium levels, most often due to excess buffer salts left by improper sample rinsing, are linked with matrix effects that fundamentally alter the formation of amino acid mass fragments.[123] In our case, this rule is appropriate for the samples prepared on gold, where the sodium percent total counts never exceeds 0.7% (figure S5.1 of the supplemental information). However, sodium is part of the NaSS structure and the percentage of the total counts made up by the sodium peak ranges from 2% – 60% (figure S5.2 in the supplemental information). Furthermore, the matrix effects caused by sodium are part of the matrix effects of the surface. To remove the sodium would be, in effect, to study a different system.

In any case, the sodium is likely bound to the NaSS sulfonate groups and unlikely to interfere with secondary ion fragmentation in the same way as unrinsed, free buffer salts. Evidence for this is the decreasing sodium signal with increasing amounts of adsorbed protein (figure 5.1A). Also, the XPS sodium signal decreases to a greater extent than the attenuation of the polymer sulfur signal. Sodium compositions decrease 93% versus only a 73% decrease for sulfur between 0 and 100 μg/ml protein solution concentrations. This suggests not only sodium attenuation, but also potentially displacement by adsorbing proteins. Counter-ion displacement during protein adsorption has been observed in other charged polymer brush systems.[120]

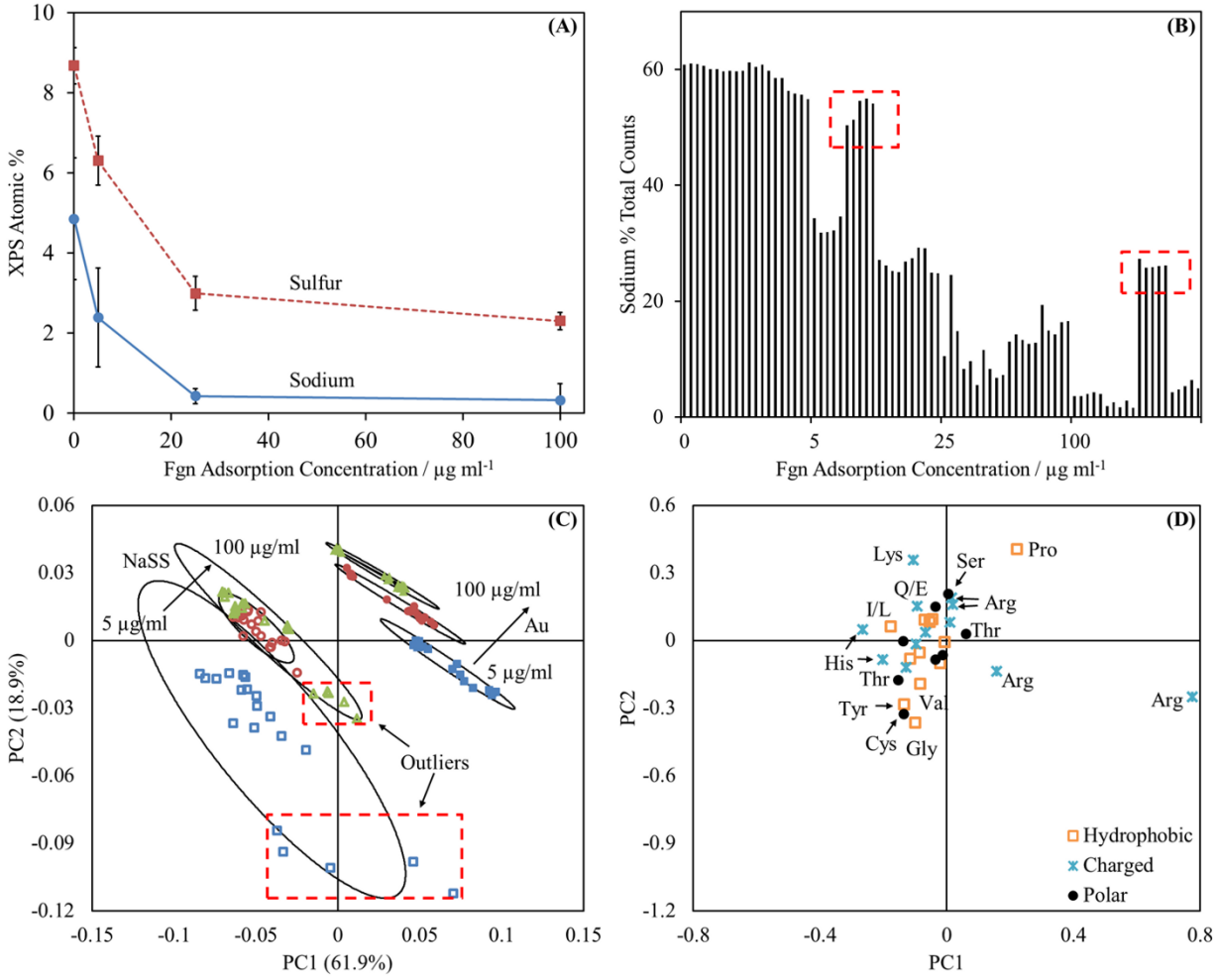

Figure 5.1. (A) Sulfur and sodium XPS compositions for Fgn adsorbed onto NaSS surfaces. (B) Sodium (m/z 22.99) percent of total counts for Fgn adsorption onto NaSS surfaces. (C) and (D) amino acid peak list PCA results for Fgn adsorbed onto NaSS surfaces. For panel (C): ■ represents adsorption from 5 µg/ml solutions, ● represents adsorption from 25 µg/ml solutions, and ▲ represents adsorption from 100 µg/ml solutions. Open symbols are used for NaSS substrates and closed symbols are used for gold substrates. The error bars in (A) represent standard deviations and the ellipses in (C) represent 95% confidence intervals. The boxed outliers in (B) indicate samples with outlying sodium concentrations relative to their respective sample groups. The corresponding samples are boxed in panel (C). Panel (A) supports the claim that the sodium is substrate bound and has little impact on amino acid fragmentation patterns. Comparison of panels (C) and (D) with panels (C) and (D) in figure 5.3 shows that the NaSS sodium levels do not drastically effect the conclusions drawn from the PCA results.

The PCA results also support the claim that the sodium does not interfere with secondary ion fragmentation. If sodium has a substantial impact on amino acid fragmentation, then fluctuations in sodium levels within treatment groups should yield fluctuations—or outliers—in the amino acid PCA results. For BSA adsorbed on NaSS the average sodium percent is 32.4% ± 3.7% (average ± standard deviation) for three of the four samples in the 25 μg/ml group, and 18.2% ± 1.1% for the last sample (figure S5.2 in the supplemental information). Similarly, for 100 μg/ml, the average sodium percent total counts 10.1% ± 2.4% for three of the four samples, and 16.4% ± 1.0% for the last sample. If the sodium in this system affects the amino acid fragmentation process, the sodium count fluctuations should register as two sets of five outliers in the PCA results—one set of five each in the 25 μg/ml and 100 μg/ml treatment groups. The BSA on NaSS results display a good deal of scatter, but there are no obvious outliers (figure 5.3A). However, groups of outliers, corresponding with samples with higher than average sodium counts, are observed for Fgn on NaSS (figure 5.1B). Separation between treatment groups does improve upon removal of these outliers (compare figures 5.1C and 5.3C); though, while the loadings change in magnitude, there are no obvious changes in loading direction. Even when the sodium levels affect the scores, removal of the outliers does not significantly change interpretation of the PCA results. Therefore, sodium appears to be bound to the grafted NaSS chains and does not seem to have a significant effect on the amino acid fragmentation patterns.

5.4.2 XPS and ToF-SIMS Isotherms

Protein adsorption, at solution concentrations ranging from 5 to 100 μg/ml, was followed with XPS, plotting nitrogen atomic% as an indication of surface protein concentration (figure 5.2). Caution must be taken with regard to classifying these adsorption curves as Langmuirian, or any other type, since the physics of protein adsorption are often at odds with the fundamental assumptions behind the classical isotherm models.[121, 124] What is clear from the shape of the adsorption isotherms, specifically the near-infinite initial slopes, is that all three proteins and plasma have a higher affinity for gold versus NaSS.[121] However, except for IgG—which shows the largest disparity in the amount of protein adsorbed between these two surfaces—NaSS adsorbs the same (for plasma) or more (for BSA and Fgn) total protein than gold at the 100 μg/ml solution concentration. A possible explanation for this is that proteins in their native state have much lower affinity and form fewer initial contacts with NaSS than gold.[121] Any proteins

that do adsorb to NaSS undergo structural rearrangements—which occur on a time scale from 10^0 to potentially even 10^3 seconds[12]—increasing the number of contacts on the surface and resulting in a larger fraction of irreversibly adsorbed species.[121] The differing plasma adsorption curves on NaSS and gold surfaces are further evidence in support of this argument. The plasma adsorption experiments were performed at a constant 100 μg/ml solution concentration and increasing times. At times up to 30 minutes, the gold surfaces adsorb substantially more protein than NaSS. Hence, proteins initially have higher affinity for gold than NaSS, even at high solution concentrations. At 60 minutes, however, NaSS adsorbs nearly as much protein as gold. And where gold appears to have saturated at 120 minutes, the slope of the NaSS isotherm is still fairly steep suggesting that this system has not yet reached its equilibrium surface concentration. Hence, the protein affinity for NaSS increases with time, and we postulate structural rearrangement of the adsorbed proteins is the reason for this. Still, except for plasma and BSA adsorbed onto gold surfaces, none of the isotherms appear to have saturated. That BSA adsorbed onto gold reaches saturation is confirmed by the measurements of Tidwell et al.[125] who arrived at a nitrogen XPS surface composition of ~9% for adsorption from a 1 mg/ml solution of BSA. The nitrogen atomic% here is also ~9%, at a BSA solution concentration of 100 μg/ml.

Structural rearrangements may also explain the differences in amounts of adsorbed IgG. If IgG adsorbs in a higher surface area conformation onto NaSS surfaces compared to gold (due to a lower packing-density orientation and/or a greater degree of denaturation), then the total amount of adsorbed protein would be much higher on gold for the same surface coverage. This is supported by the PC1 isotherms in figure 5.2 (E) through (H). In the case of BSA and Fgn, the shapes of the XPS and SIMS isotherms more or less match, indicating that PC1 scores are correlated to adsorbed protein surface concentration. However, this correlation does not hold for IgG. PC1 would predict that NaSS adsorbs more IgG than gold at 100 μg/ml, even though

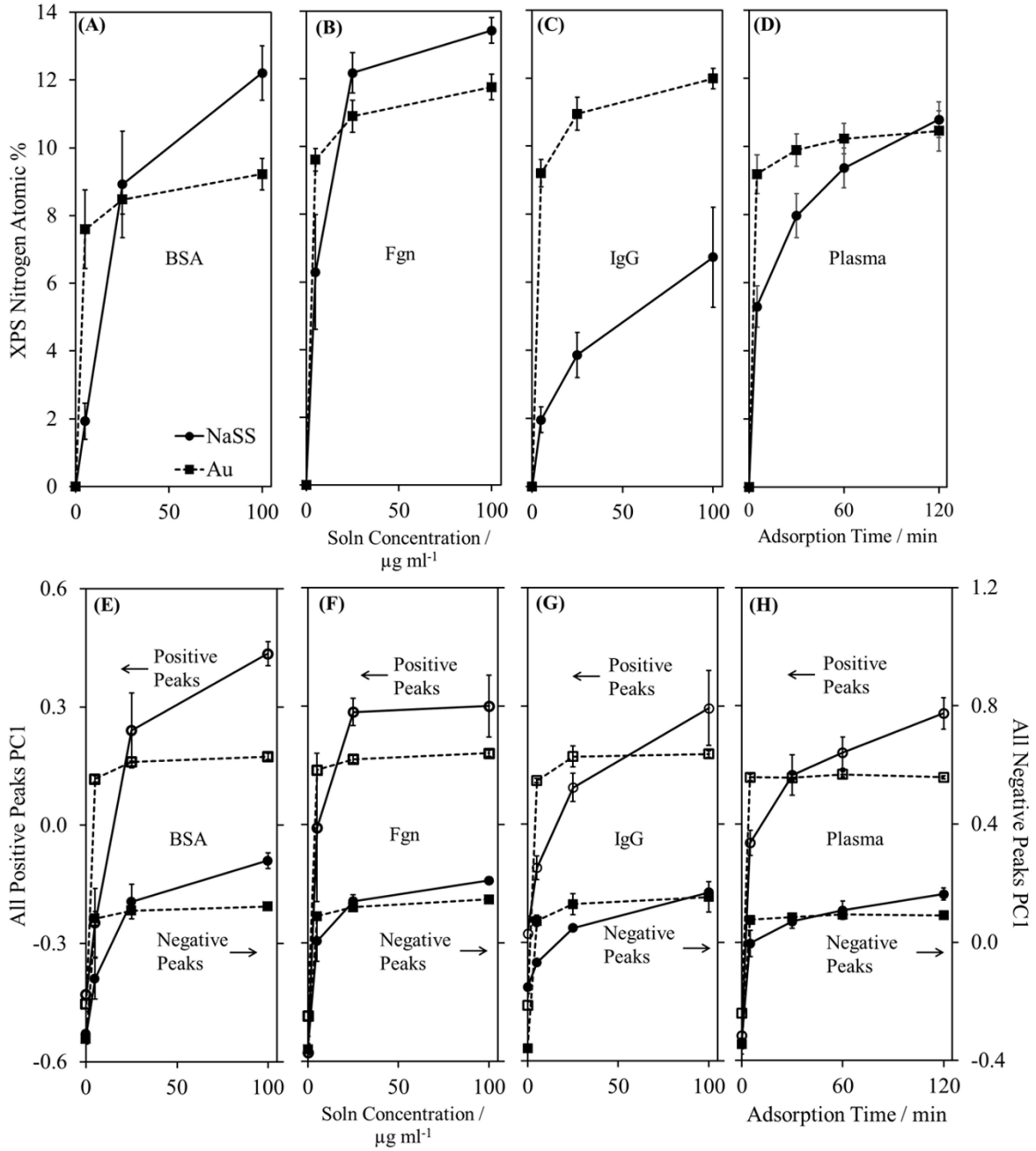

Figure 5.2. XPS isotherms for (A) BSA, (B) Fgn, (C) IgG, and (D) plasma adsorption onto gold and NaSS surfaces. Panels (E) through (H) are isotherms of the PC1 scores obtained from PCA using peak lists containing all peaks that are at least 3x the background intensity. In all panels, ■ and dashed lines represent gold substrates, while ● and solid lines represent NaSS substrates. In panels (E) through (H), open symbols represent scores from PCA of the positive spectra, and closed symbols represent scores from PCA of the negative spectra. Error bars represent standard deviations.

XPS—which is the more quantitative of the two techniques[46, 47]—clearly shows the opposite to be the case. This is simply because the XPS sampling depth (~10 nm) is nominally five times that of SIMS (~ 2 nm).[46, 47] Wagner et al. reported that, relative to ^{125}I-radiolabeling measurements, SIMS overpredicted the amount of Fgn adsorbed in a binary IgG/Fgn film. This was attributed to the differences in sampling depth between the two techniques, and the organization of the adsorbed protein film.[126] While ^{125}I-radiolabeling measured the film bulk composition, SIMS—due to its high surface sensitivity—oversampled the adsorbed Fgn, which had oriented preferentially at the vacuum interface. (The sampling depth of ^{125}I-radiolabeling, for all practical purposes, can be considered infinite.)[127] Similarly, in our case, the larger XPS sampling depth results in measurements that more closely represent the total amount of adsorbed protein, whereas SIMS more closely represent the fraction of covered versus exposed substrate. It is, therefore, more accurate to say that the SIMS isotherms are correlated to surface coverage, which is dependent not only on surface concentration but also on adsorbed protein structure. Thus, we propose that the SIMS isotherms indicate the IgG molecules have adsorbed in a lower packing-density orientation, and may also have denatured and spread out to cover a higher fraction of the NaSS surface. This is compared to more intact IgG molecules covering a smaller fraction of the surface on gold. Sampling depth differences also explain why the SIMS isotherms saturate more often and at lower concentrations than those measured by XPS. Similar differences in protein adsorption curves have been observed comparing XPS and atomic force microscopy results for fibronectin adsorbed onto mica surfaces.[128]

5.4.3 PCA of All Positive and Negative Peaks

While the focus of this paper is how adsorbed protein surface structure changes between bare and NaSS-grafted gold substrates, this section briefly addresses some overarching trends observed in the ToF-SIMS data. The PCA results discussed below were obtained using peak lists containing all positive or negative peaks with intensity at least three times the background.

PCA of All Peaks on Gold

In both polarities, PCA clearly distinguishes the protein-free from the protein-containing surfaces (panels A through C of figures S5.3 – S5.8 in the supplemental information). However, in the positive polarity, clear separation between sample groups with different protein surface coverages is observed only for BSA. Better separation is observed in the negative polarity; where

samples prepared at different solution concentrations clearly separate for Fgn and IgG, but not for BSA. Regardless of polarity, the variance in the data is dominated by differences between the protein-free and protein-containing samples, which separate along PC1. In the positive polarity, this separation appears to be based on small hydrocarbon peaks loading (negatively) with the protein-free samples, and amino acid fragments loading (positively) with the protein-containing samples. One notable exception is the arginine amino acid peak (m/z 73.06, $C_2H_7N_3$), which consistently loads with those samples that should be protein-free. Inspection of the raw spectra reveals that the arginine peak overlaps with a broad peak found only in the protein-free samples. A likely assignment for this peak is SiC_3H_9 at m/z 73.19, with poly(dimethyl silicone) (PDMS) contamination the likely source. Therefore, the m/z 73.06 peak was excluded from the protein structure analyses discussed below in the PCA of Amino Acid Mass Fragments section. Other arginine peaks (m/z 100.9, $C_4H_{10}N_3$; m/z 101.1, $C_4H_{11}N_3$; and m/z 127.1, $C_5H_{11}N_4$) were retained, minimizing the impact of the information lost. The small hydrocarbons detected on the protein-free samples are likely from adventitious carbon, which is then displaced by adsorbing protein. Thus, separation is based on substrate vs. amino acid peaks. This also appears to be the case in the negative polarity, where small hydrocarbon fragments, gold, and contaminants load (negatively) with the protein-free samples, and nitrogen-containing peaks load (positively) with the protein-containing samples. If there is any separation between the protein-containing treatment groups, it occurs along PC2. In certain cases, PC2 scores increase with increasing protein concentration. In other cases, the opposite is true. Therefore, few clear trends were observed in PC2.

PCA of All Peaks on NaSS

Despite being a more complex system, PCA is better able to separate between treatment groups on NaSS than on gold (panels D through F of figures S5.3 – S5.8 in the supplemental information). For all proteins, PC1 scores increase with increasing protein adsorption solution concentration. This is consistent our observations on gold. However, the increase in PC1 scores is more gradual since the increase in protein surface concentration is more gradual on NaSS versus gold, as evidenced by the XPS isotherms. In both polarities, substrate peaks are associated with the samples prepared from the 0 and 5 μg/ml protein solutions. Interestingly, a number of the high loading substrate peaks in the positive polarity are sodium adducts of the same peaks

observed in the negative spectra. And in both polarities, amino acid fragments are associated with samples prepared from the 25 and 100 μg/ml protein solution concentrations. Breaking with this trend in the negative polarity is the NaSS monomer ($C_8H_7SO_3$), which paradoxically loads (positively) with the samples prepared from the 25 and 100 μg/ml protein solution concentrations. There is some separation along PC2 in both polarities. However, there are no obvious trends in the loadings that lead to a physical explanation for the source of variance.

In summary, for both gold and NaSS surfaces, and for both positive and negative polarities, PC1 scores trend with protein surface concentration, as was discussed above in the XPS and ToF-SIMS isotherm section. This is confirmed by the loadings, which associate substrate peaks with the protein-free samples, and amino acid peaks with the protein-containing samples. Some separation is observed along PC2 between samples exposed to different protein solution concentrations, but not consistently. Also, no discernable trends are observed in the loadings to explain the separation. More information regarding adsorbed protein structure is likely to be obtained by narrowing the peak list to include only amino acid-derived mass fragments.

5.4.4 PCA of Amino Acid Mass Fragments

PCA using only the amino acid fragment peaks is able to distinguish between the same protein adsorbed on gold or NaSS, and also between protein films adsorbed from different solution concentrations on the same surface (Panels A, C, and E of figure 5.3). This suggests that proteins adsorb differently on NaSS and gold, and that the adsorbed protein structure changes with surface concentration. To probe these differences, we first broadly classified each amino acid as charged, polar, or hydrophobic (Panels B, D, and F of figure 5.3). However, we found no obvious trends using this general classification of amino acid fragments. For example, no apparent trend was observed that related to the coulombic interactions between sulfonate groups and positively charged amino acids to yield a preferred orientation for any protein on NaSS. Using VMD to visualize the distribution of charged, polar, or hydrophobic amino acids, we confirmed that these three categories appear evenly distributed throughout the structure of each protein (data not shown).

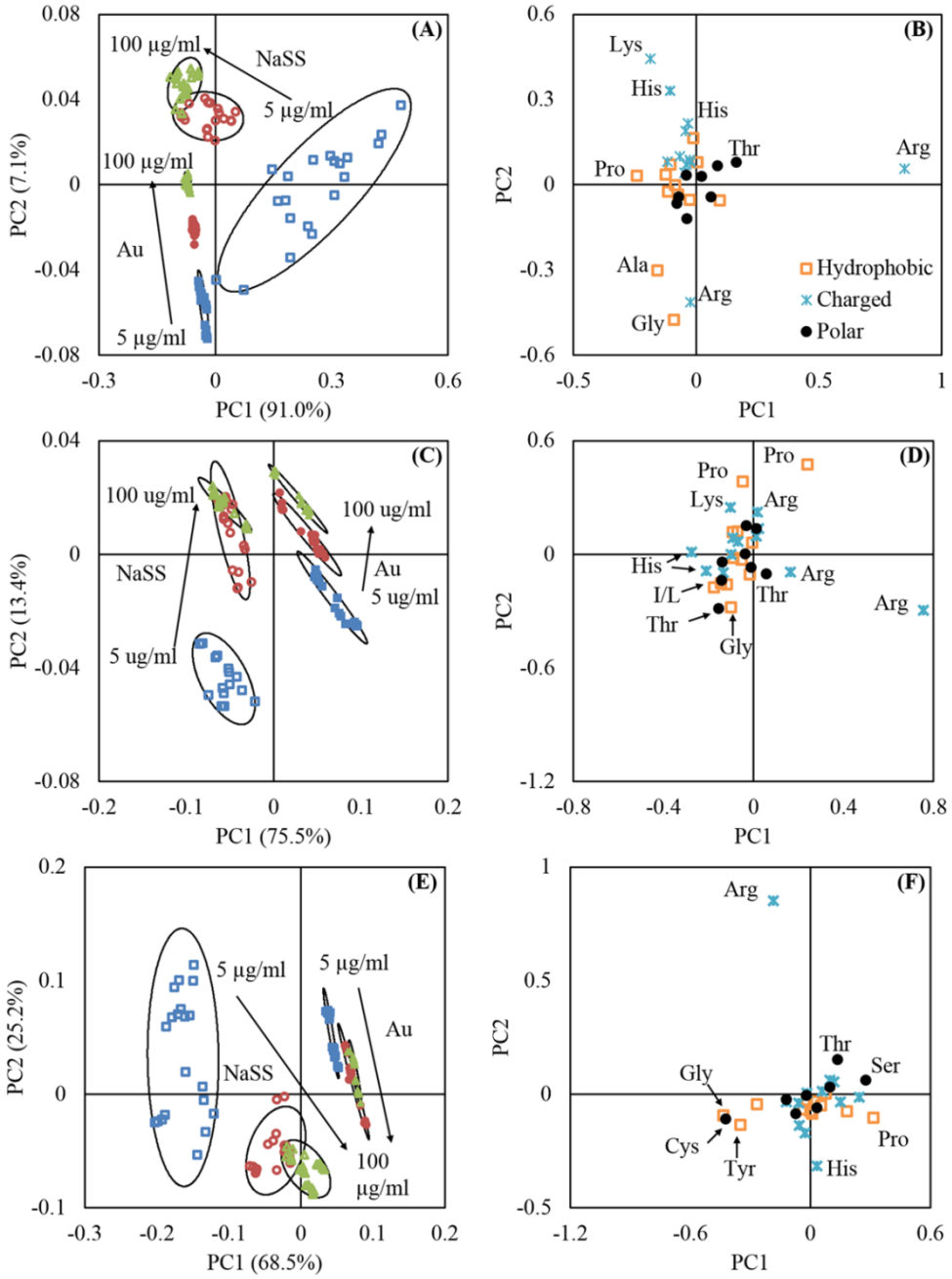

Figure 5.3. Amino acid peak list PCA results. Panels (A) and (B) are the scores and loadings plots for BSA. Panels (C) and (D) are the scores and loadings plots for Fgn. Panels (E) and (F) and the scores and loadings plots for IgG. In panels (A), (C), and (E), ■ represent adsorption from 5 µg/ml solutions, ● represent adsorption from 25 µg/ml solutions, and ▲ represent adsorption from 100 µg/ml solutions. Open symbols are used for NaSS substrates and closed symbols are used for gold substrates. The ellipses in (A), (C), and (E) represent 95% confidence intervals.

Therefore, we do not observe any of these three general categories to be correlated with conformation or orientation of the adsorbed proteins. Instead, trends in specific peak intensity ratios for strategically chosen, non-uniformly distributed amino acids were used to examine the conformation and orientation of the adsorbed proteins. Baugh, et. al., showed that structural information about surface immobilized proteins can be gleaned from such ratios.[129, 130]

To assess the level of denaturation for each protein on NaSS and gold surfaces, the first set of ratios examined were for buried/surface amino acids. An increase in the ratio of buried/surface amino acids indicates a more denatured adsorbed protein. The specific residues chosen for each protein are listed in table 5.1 and highlighted in the insets of figure 5.4, where the relevant buried and surface amino acids are highlighted in yellow and black, respectively. The peak intensity (*I*) ratios used are shown in Eq. 1.

$$\text{BSA: } \frac{I_{Cys}}{I_{Glu}} \qquad \text{Fgn: } \frac{I_{Val}}{I_{Pro}+I_{Arg}} \qquad \text{IgG: } \frac{I_{Cys}}{I_{Arg}} \quad \text{(Eq. 1)}$$

Table 5.1. Amino acids selected for protein structural analysis.

	Amino Acids for Denaturation Analysis		Amino Acids for Orientation Analysis	
	Buried	Surface	Bottom*	Top*
BSA	Cys	Glu	Asn, Tyr	His
Fgn	Val	Pro, Arg	-	-
IgG	Cys	Arg	Asp, Val	Ser

*Bottom and top refer to the protein with the orientation shown in figure 5.5.

For all three proteins, the peak ratios are higher on NaSS than gold (figure 5.4), indicating that proteins denature more on NaSS, which is particularly prominent for samples prepared from the lowest protein solution concentrations. This suggests that the extent of denaturation decreases with the increased adsorbed protein packing density achieved at higher surface concentrations.[131] This is also supported by the scatter in the scores plots (figure 5.3). As the scatter within a treatment group increases, the variability within the constituent spectra also increases. Higher scatter would be expected for a more highly denatured protein film with a random statistical sampling of amino acids exposed at the vacuum interface. The scatter for all proteins prepared from all solution concentrations is less on gold verses NaSS surfaces. Taken alongside the

buried/surface amino acid ratios, this suggests adsorbed proteins denature more on NaSS than on gold. Also, the scatter decreases with protein solution concentration for all three proteins on NaSS surfaces, supporting the conclusion that increased adsorbed protein packing density on NaSS decreases the degree of denaturation. No such trend is observed on gold, which may due to the formation of islands with high local density even at low protein solution concentrations. Or it may simply be that proteins adsorbed onto gold surfaces better retain their native conformation, even at low coverages. Proteins are known to better retain their structure on neutral hydrophilic than on charged surfaces.[118]

For all adsorbed protein films, the trend in buried/surface ratios follows the trend observed in the scatter in the PCA results. No significant difference is observed in the buried/surface amino acid ratios for any of the three proteins adsorbed onto gold. In contrast, this ratio decreases with increasing protein solution concentration for the protein films adsorbed onto NaSS. The largest difference in this ratio between the NaSS and gold surfaces is for adsorbed IgG (figure 5.4C). Thus, IgG adsorbed onto NaSS surfaces is the most denatured of the three adsorbed proteins, especially at the lowest protein surface coverages. This is consistent with the findings of a high-surface area conformation suggested by the XPS and ToF-SIMS isotherms discussed above.

To determine if any of the three proteins adopts a preferred orientation on either surface, a similar analysis was performed using ratios of amino acids on opposite sides of each protein. An increase in the ratio of amino acids on enriched one end relative to amino acids enriched on the opposite end suggests a preferred protein orientation. The key amino acids for BSA and IgG are listed in table 5.1, and the ratios are found in Eq. 2. Due to the symmetry and even distribution of amino acids throughout Fgn, we were unable to find a ratio unique to a given orientation.

$$\text{BSA: } \frac{I_{Asn}+I_{Tyr}}{I_{His}} \qquad \text{IgG: } \frac{I_{Ser}}{I_{Asp}+I_{Val}} \quad \text{(Eq. 2)}$$

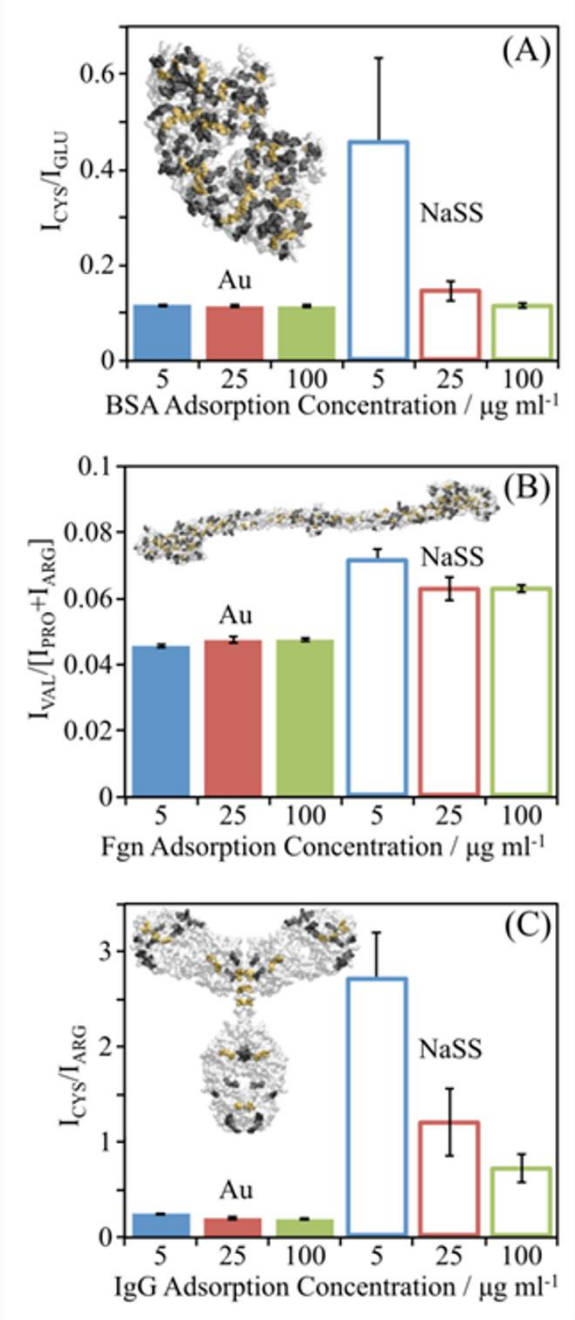

Figure 5.4. ToF-SIMS peak intensity ratios suggest levels of denaturation of (A) BSA, (B) Fgn, (C) and IgG adsorbed onto gold and NaSS surfaces. Insets show the crystal structure of each protein. Bars represent mean amino acid peak ratios for proteins adsorbed from 5 (blue), 25 (red), and 100 (green) µg/ml solutions onto Au (solid bars) or NaSS (open bars). Peak ratios are the sum of intensities of secondary ions from amino acids buried, highlighted in yellow in inset protein, divided by the sum of intensities from amino acids on the surface of the protein, highlighted in black. Error bars represent standard deviations.

If adsorbed BSA preferentially orients with the His residues enriched at the vacuum interface, the observed orientation ratio would be lower than if preferentially oriented with the His residues enriched at the substrate interface (inset of figure 5.5A). The BSA orientation ratio is higher on gold compared to NaSS surfaces, and for gold it decreases slightly with increasing solution concentration. This suggests that on gold, adsorbed BSA changes orientation slightly with surface concentration and—compared to NaSS—adopts an orientation, on average, with slightly more His residues located closer to the substrate interface. Conversely, the orientation of adsorbed BSA on NaSS appears to remain unchanged with surface concentration.

If adsorbed IgG preferentially orients with the Fab region at the vacuum interface, the observed orientation ratio would be higher than if preferentially oriented with the Fab region enriched at the substrate interface (inset of Figure 5.5B). The adsorbed IgG orientation ratio is constant on the gold surfaces and slightly higher than on NaSS. This suggests that, on average, the IgG Fab region is a bit more oriented towards the vacuum interface on gold compared to NaSS surfaces. Since there is no unique, specific attachment point on the proteins used in this study, it is expected their adsorption should result in a fairly random distribution of orientations on both surfaces. Thus, it is not surprising the orientation ratios do not exhibit large changes with increasing surface coverage, though there do appear to be significant differences between the two surfaces.

5.4.5 PC Modeling

PC models are useful for characterizing protein films adsorbed from complex mixtures, such as plasma.[123] Wagner et al. constructed such a model from ToF-SIMS data from single-component fibronectin, Fgn, IgG, BSA, and γ-globulins films on mica surfaces. Spectra from bovine plasma films, adsorbed onto mica for times ranging from 5 – 120 minutes, were then projected into the model. These experiments were done to investigate how the character of the plasma film changes with time. For Wagner et al., at short adsorption times, the plasma films were more Fgn-like in character. But at longer times, the plasma films became more γ-globulins and IgG-like than Fgn, which is a classic illustration of the Vroman effect.[123]

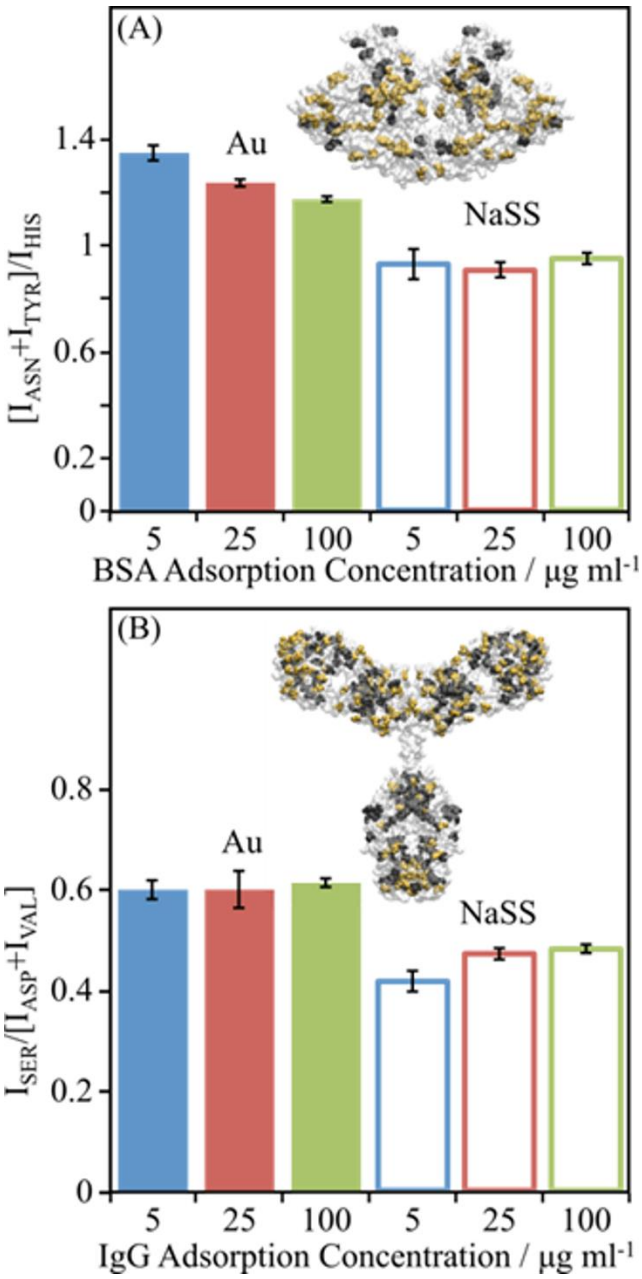

Figure 5.5. ToF-SIMS peak intensity ratios reveal possible protein orientations for (A) BSA and (B) IgG adsorbed onto gold and NaSS surfaces. Insets show the crystal structure of each protein. In (A) Asn and Tyr are highlighted in yellow while His is highlighted in black. In (B) Ser is highlighted in yellow while Asp and Val are highlighted in black. Plotted data represent average amino acid ratios for proteins absorbed from 5 (blue), 25 (red), and 100 (green) µg/ml solutions onto Au (solid bars) or NaSS (open bars) surfaces. The peak ratios are the sum of intensities of secondary ions from amino acids with asymmetric distributions, highlighted in yellow and black in the inset protein. Error bars represent standard deviations.

We replicated this procedure, constructing separate models from the single-component BSA, Fgn, and IgG ToF-SIMS data on both gold and NaSS surfaces. The amino acid peak list was used, and only two PCs were retained since retention of additional PCs had no effect on the results or conclusions of the models. Spectra from bovine plasma films, adsorbed for times ranging from 5 – 120 minutes, were then projected into the PC model for the corresponding surface. On gold, the variance in the data is dominated by differences between the single-component protein spectra, obscuring any time-dependent trends in the plasma data (Figure S5.9A in the supplemental information). On NaSS, only a weak trend is observed suggesting that the plasma film character changes from being more BSA-like to more IgG and Fgn-like with increasing adsorption time (Figure S5.9C in the supplemental information).

We found that clearer trends could be obtained by inverting the procedure above—that is, constructing the PC models from the plasma spectra and projecting in the single-component protein data. That the two procedures are mathematically different is evident since they produce distinct scores and loads plots. However, both procedures allow qualitative observations to be made about time-dependent changes in adsorbed plasma film composition. In particular, both procedures (using either signal-component data or plasma time-dependent data as the models) produce the same trends for NaSS surfaces: the plasma films are more BSA-like at short adsorption times, and more IgG and Fgn-like at longer adsorption times (Figure 5.6C). With the plasma time-dependent model, clear trends are also now observable for the gold surfaces: the plasma films are more IgG-like at short times, BSA-like at intermediate times, and Fgn-like at long times (Figure 5.6A). Therefore, gold and NaSS both apparently adsorb increasing amounts of fibrinogen with time. This is the opposite of what was observed by Wagner et al. on mica substrates.[123] However, Fgn is the heaviest of the three proteins investigated in this study, and its increase with increasing adsorption time may be related to a slower rate of diffusion from bulk solution to the surface. As Fgn arrives at the surface, it displaces the smaller BSA and IgG proteins that were the initial proteins to arrive and adsorb onto gold and NaSS. Also, mica is a rigid, oxide surface; gold is a rigid, metallic surface; NaSS is a soft, polymeric surface. It is not surprising that the composition of adsorbed plasma films changes with different surface chemistries and structures. However, our PC models are overly simplistic since they contain only three proteins, whereas plasma is composed of hundreds of proteins.[132] Therefore, while both gold and NaSS appear to adsorb more Fgn with time, further study with a more extensive set of

proteins is required to confirm that this finding is truly representative of the final state of the adsorbed plasma films.

5.5 Conclusions

In this study, we investigated the adsorption of BSA, bovine Fgn, bovine IgG, and bovine plasma onto bare and NaSS-grafted gold surfaces. We measured adsorption isotherms, using XPS to follow changes in surface nitrogen composition with increasing protein solution concentration. Using a combination of ToF-SIMS, PCA, and VMD we investigated differences in adsorbed protein structure between both surfaces. We also used PC modeling to qualitatively describe changes in bovine plasma adsorbed films with time.

Our conclusions are as follows:

- All proteins have a higher initial affinity for gold than NaSS surfaces. However, except for IgG, NaSS adsorbs the same (for plasma) or more (for BSA and Fgn) total protein than gold from the 100 μg/ml solution concentration. This may be because any proteins that do adsorb to NaSS undergo structural rearrangements over time, increasing the number of contacts with the surface and resulting in a larger fraction of the surface covered by irreversibly adsorbed species. Nevertheless, with the exception of BSA and plasma adsorption onto gold, neither surface appeared to have saturated at the 100 μg/ml protein solution concentration.
- PCA using just the amino acid peaks is able to distinguish between the same protein adsorbed on gold or NaSS, and also between protein films adsorbed from different solution concentrations on the same surface. This suggests that proteins adsorb differently on NaSS and gold, and that the structure of the adsorbed proteins changes with surface concentration.

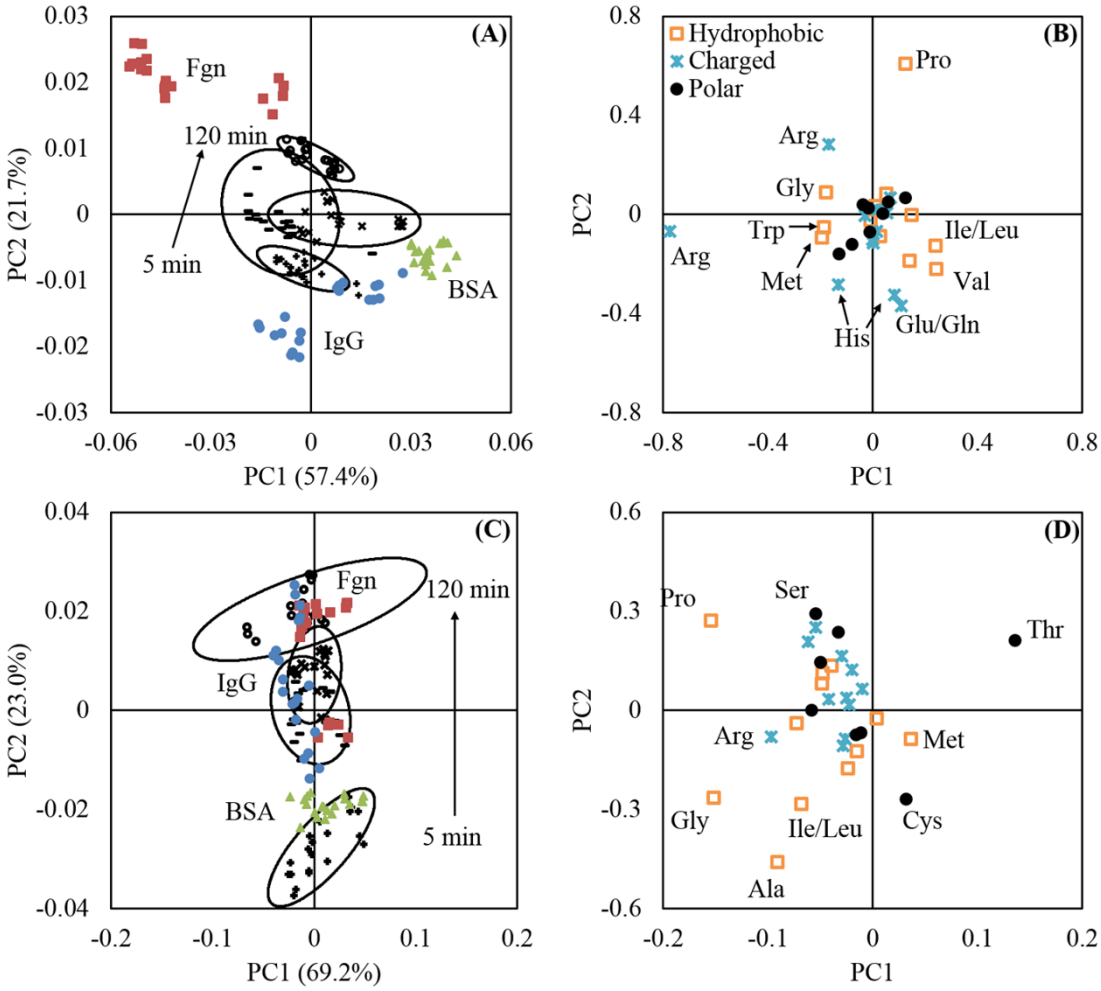

Figure 5.6. PC models for gold (A and B) and NaSS (C and D) surfaces. The models were constructed using the amino acids peaks from 100 µg/ml plasma adsorption ToF-SIMS data. Single-component BSA (▲), Fgn (■), and IgG (●) spectra were projected into the models. In panels (A) and (C) all black symbols represent the plasma adsorption data used to construct the model: + represent the 5 minute adsorption group, - represent the 30 minute adsorption group, × represent the 60 minute adsorption group, and ○ represent the 120 minute adsorption group. The ellipses in (A) and (C) represent 95% confidence intervals. Panel (A) shows that on gold: the plasma films are more like adsorbed IgG at short times, more like BSA at intermediate times, and more like Fgn at long times. Panel (C) shows that on NaSS: the plasma films are more like BSA at short times, then more like IgG and Fgn at long times.

- To assess the level of denaturation for each protein on NaSS and gold surfaces, we examined the ratio of select buried/surface amino acids. For all three proteins, the peak ratios are higher on NaSS than gold, indicating that the proteins denature more on NaSS, which is most prominently observed from protein films adsorbed at lower solution concentrations. This suggests that the increased adsorbed protein packing density, achieved at higher surface concentrations, decreases protein denaturation on NaSS.
- To determine if any of the three proteins adopts a preferred orientation on either surface, a similar analysis was performed using ratios of amino acids on opposite ends of each protein. Small differences in average orientations between the two surfaces are observed for BSA and IgG films. The symmetry of Fgn prevented us from effectively examining the orientation of those films.
- The PC models suggest the following changes in the character of proteins films adsorbed from plasma at times ranging from 5-120 minutes. For gold surfaces the plasma films are more IgG-like short times, more BSA-like at intermediate times, and more Fgn-like at long times. For NaSS the plasma films are more BSA-like at short times, and IgG and Fgn-like at long times. However, our PC models only contain three proteins, whereas plasma is composed of hundreds of proteins. Therefore, while both gold and NaSS appear to adsorb more Fgn with time, further study is required to confirm that this is truly representative of the final state of the adsorbed plasma films.

5.6 Supplemental Information

ToF-SIMS and XPS Characterization of Protein Films Adsorbed onto Bare and Sodium Styrene Sulfonate Grafted Gold Substrates

Rami N. Foster, Elisa T. Harrison
Department of Chemical Engineering, University of Washington – Seattle, and National ESCA and Surface Analysis Center for Biomedical Problems, Seattle, WA 98195

David G. Castner
Departments of Chemical Engineering and Bioengineering, University of Washington – Seattle, and National ESCA and Surface Analysis Center for Biomedical Problems, Seattle, WA 98195

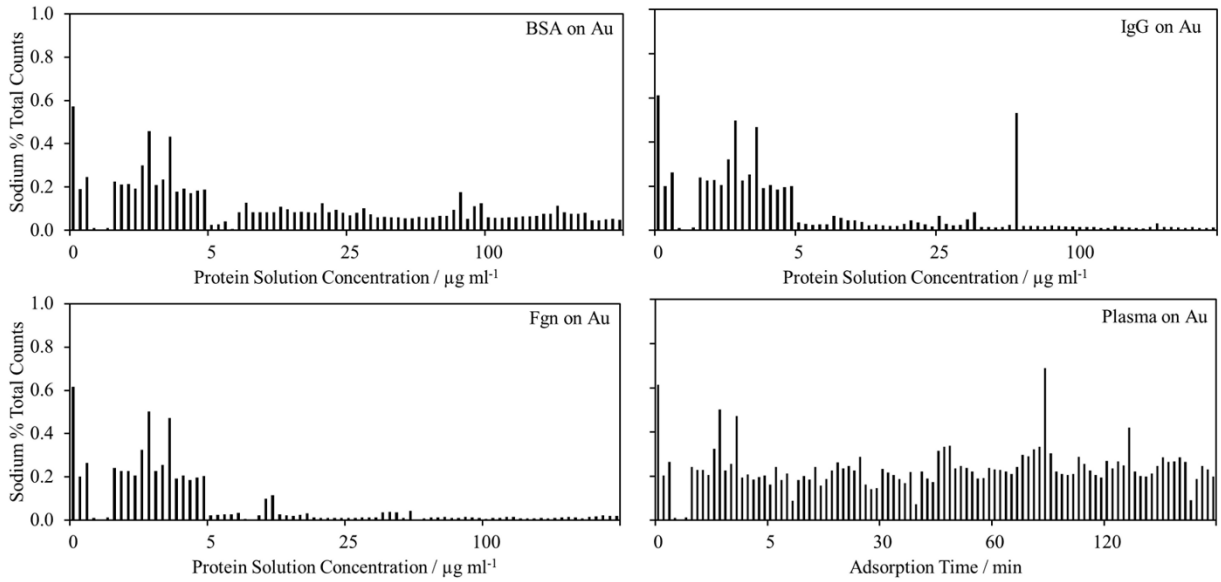

Figure S5.1. Percentage of the total secondary-ion counts accounted for by the sodium peak (m/z 22.99) for BSA, Fgn, IgG, and plasma adsorbed onto gold surfaces. Spectra containing sodium counts >1% of the total counts are typically removed from the dataset. The sodium counts in these set of spectra never exceed ~0.7%.

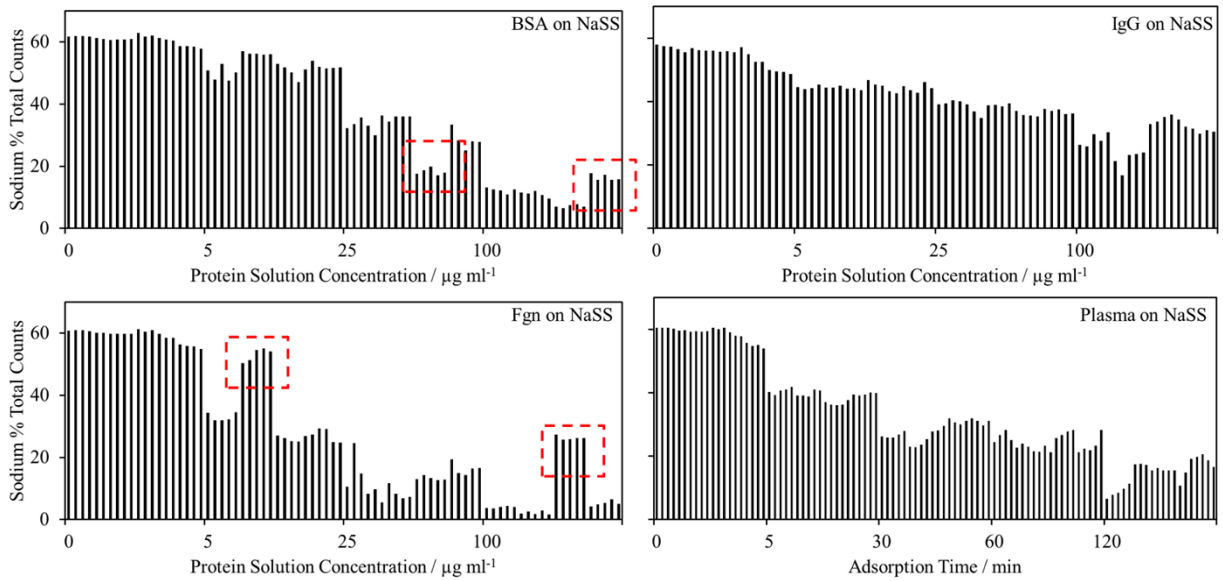

Figure S5.2. Percentage of the total secondary-ion counts accounted for by the sodium peak (m/z 22.99) for BSA, Fgn, IgG, and plasma adsorbed onto NaSS surfaces. Spectra containing sodium counts >1% of the total counts are typically removed from the dataset. The sodium counts in this set of spectra ranged from 2% – 60%. However, the sodium is part of the NaSS substrate and do not exhibit the same influence on the spectra that free buffer salts do. The samples highlighted with red boxes are the outlier groups discussed in the text.

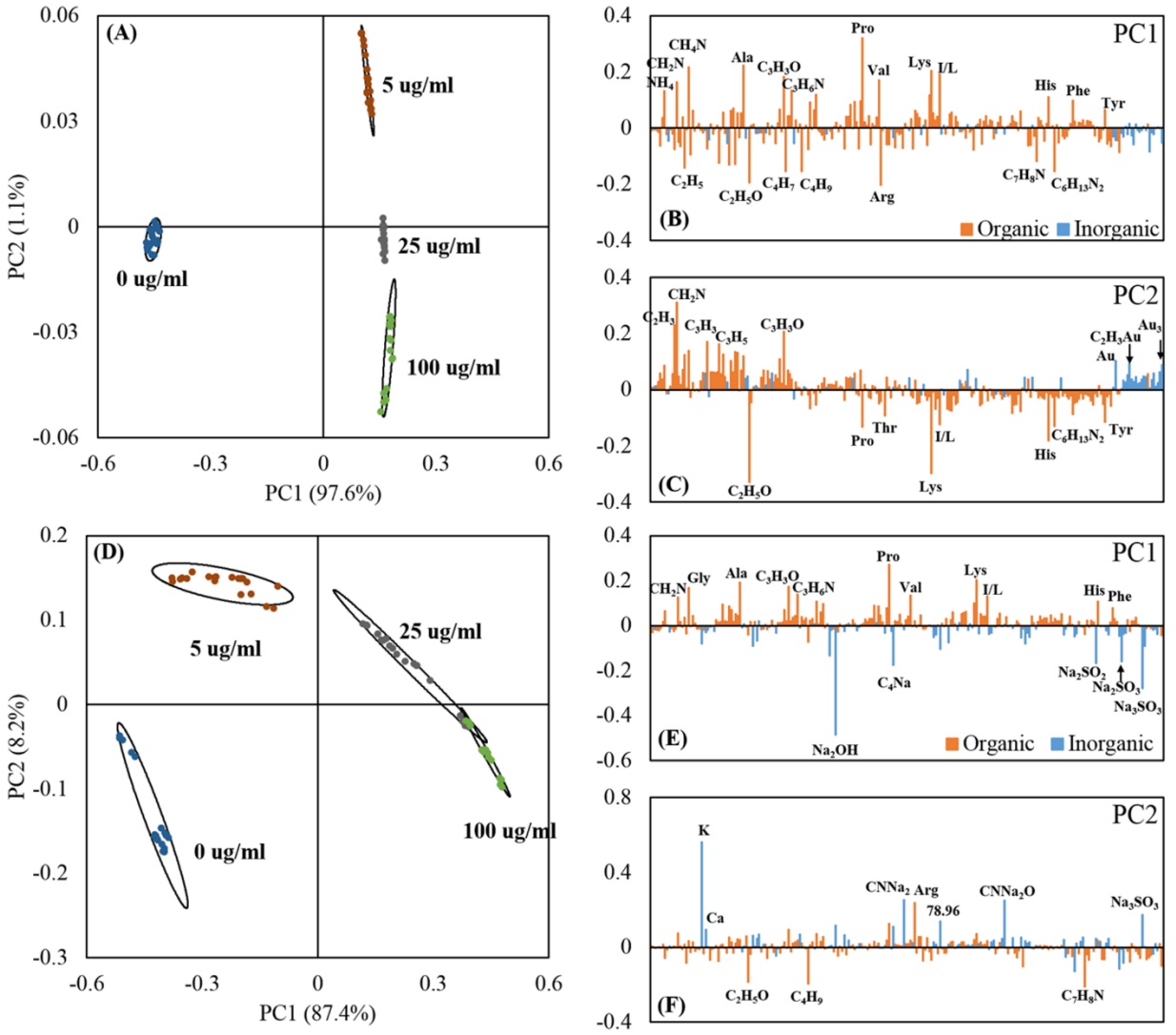

Figure S5.3. Adsorbed BSA PCA results using all peaks in the positive ion spectra. Panels A – C correspond to the scores and loadings plots for BSA adsorbed onto gold surfaces. Panels D – F correspond to the scores and loadings plots for BSA adsorbed onto NaSS surfaces.

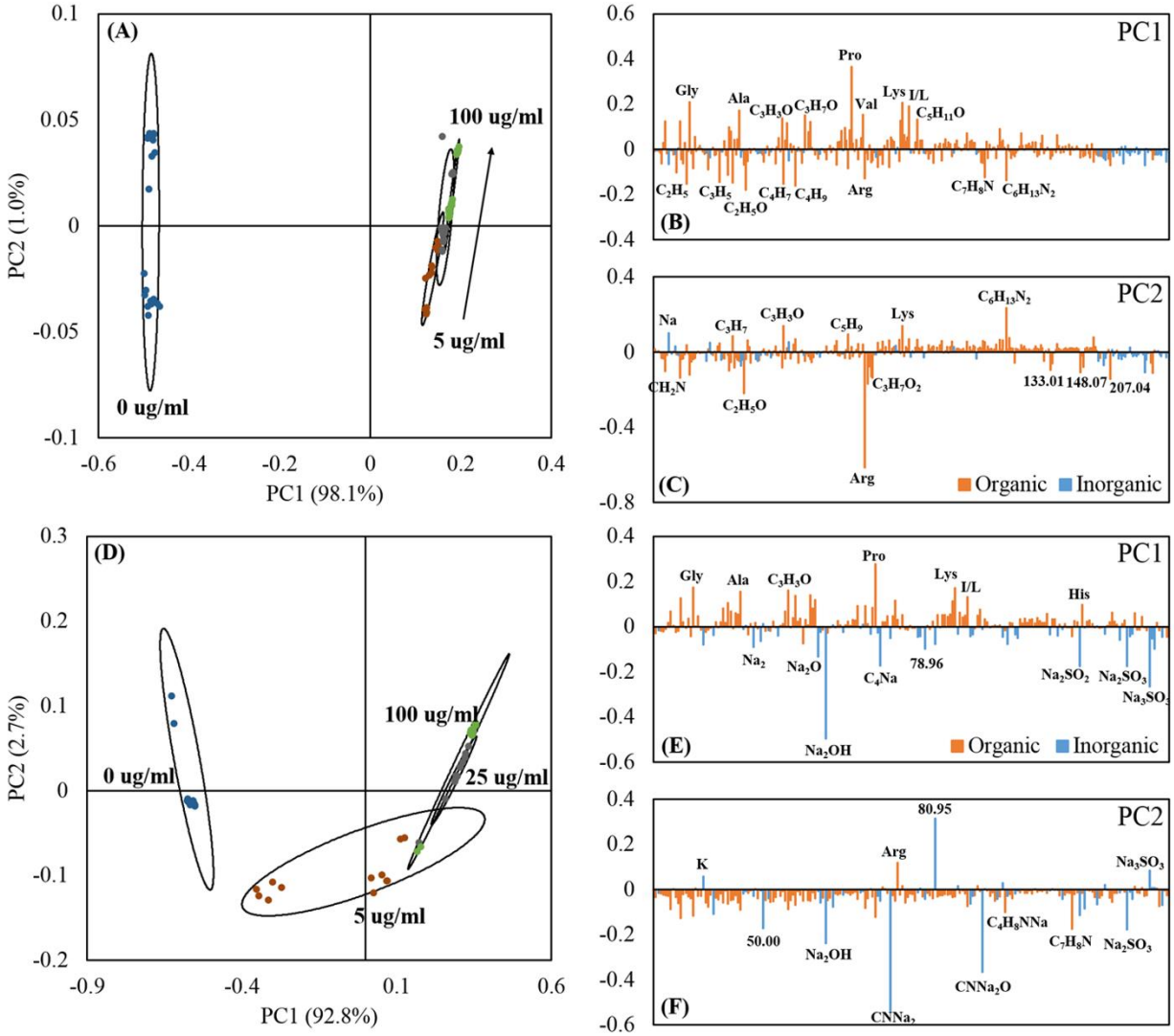

Figure S5.4. Adsorbed Fgn PCA results using all peaks in the positive ion spectra. Panels A – C correspond to the scores and loadings plots for Fgn adsorbed onto gold surfaces. Panels D – F correspond to the scores and loadings plots for Fgn adsorbed onto NaSS surfaces.

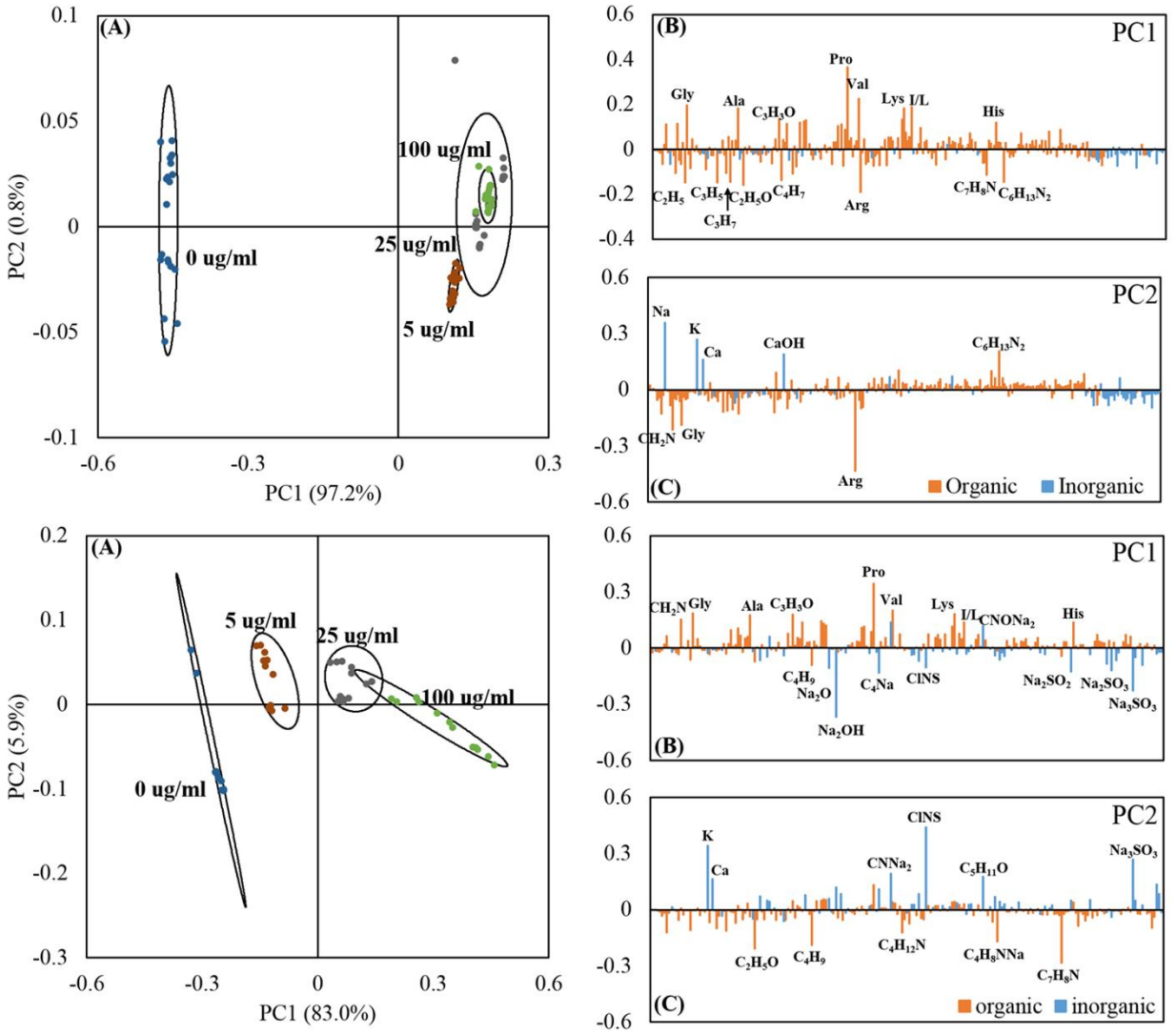

Figure S5.5. Adsorbed IgG PCA results using all peaks in the positive ion spectra. Panels A – C correspond to the scores and loadings plots for IgG adsorbed onto gold surfaces. Panels D – F correspond to the scores and loadings plots for IgG adsorbed onto NaSS surfaces.

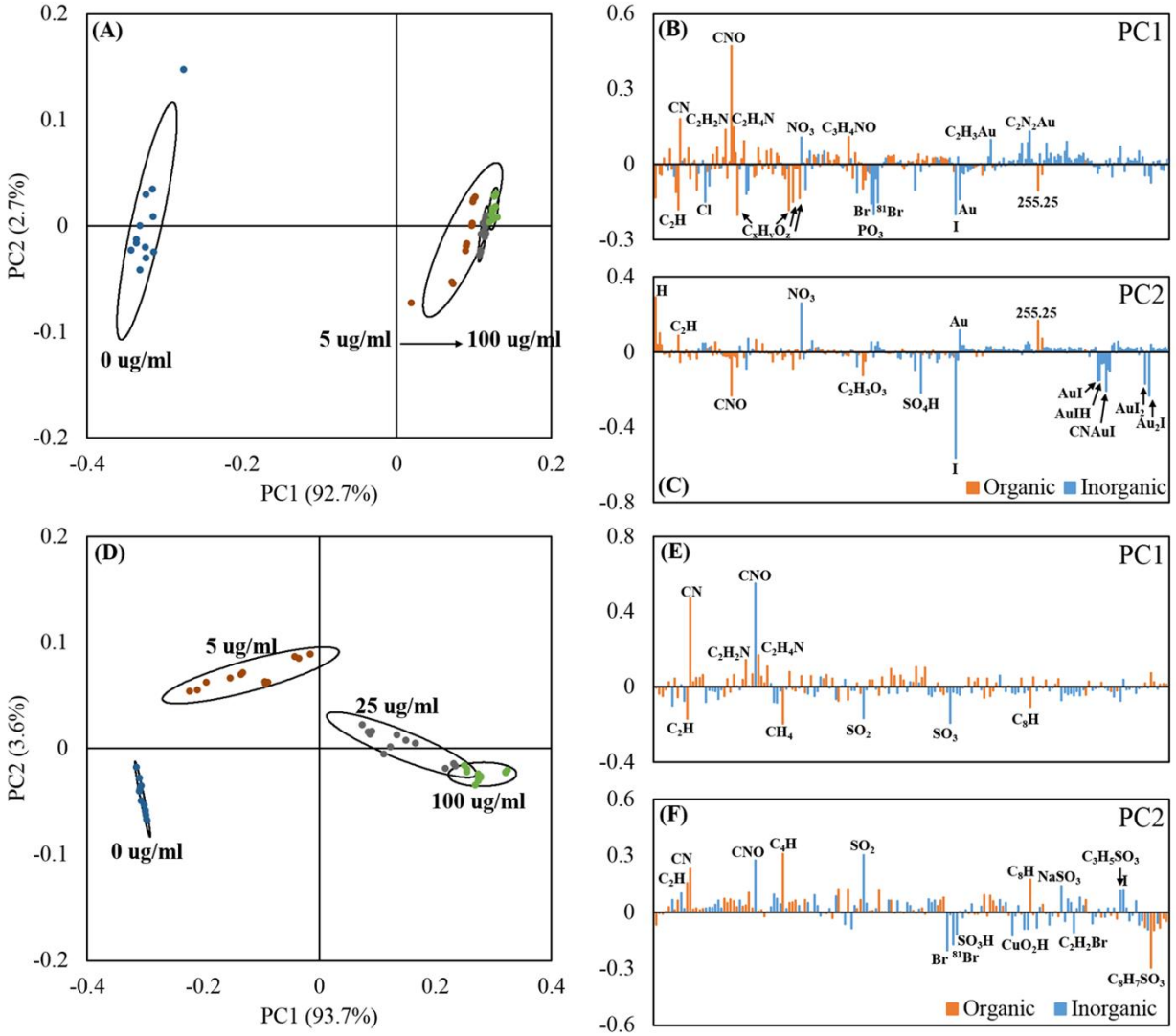

Figure S5.6. Adsorbed BSA PCA results using all peaks in the negative ion spectra. Panels A – C correspond to the scores and loadings plots for BSA adsorbed onto gold surfaces. Panels D – F correspond to the scores and loadings plots for BSA adsorbed onto NaSS surfaces.

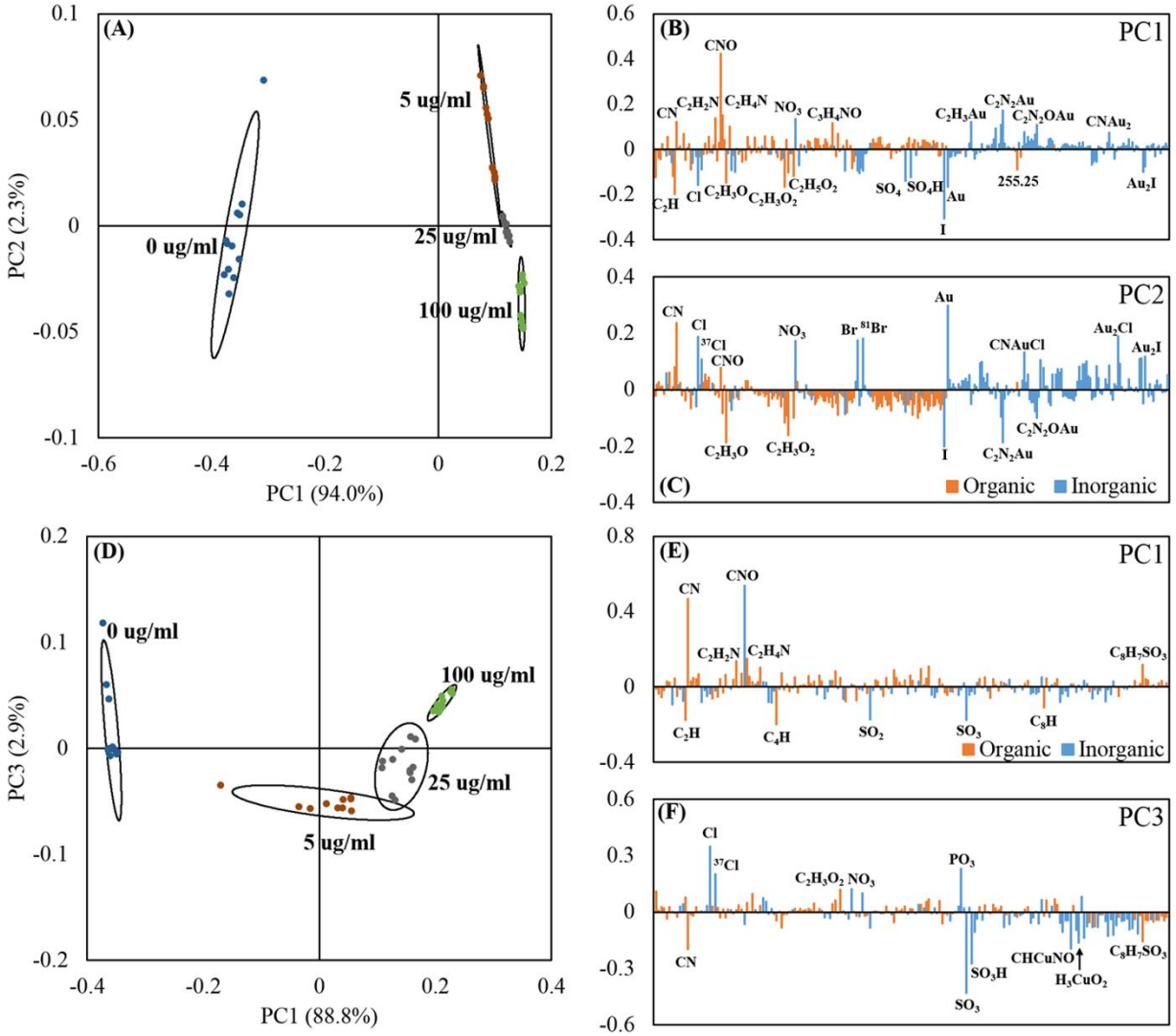

Figure S5.7. Adsorbed Fgn PCA results using all peaks in the negative ion spectra. Panels A – C correspond to the scores and loadings plots for Fgn adsorbed onto gold surfaces. Panels D – F correspond to the scores and loadings plots for Fgn adsorbed onto NaSS surfaces.

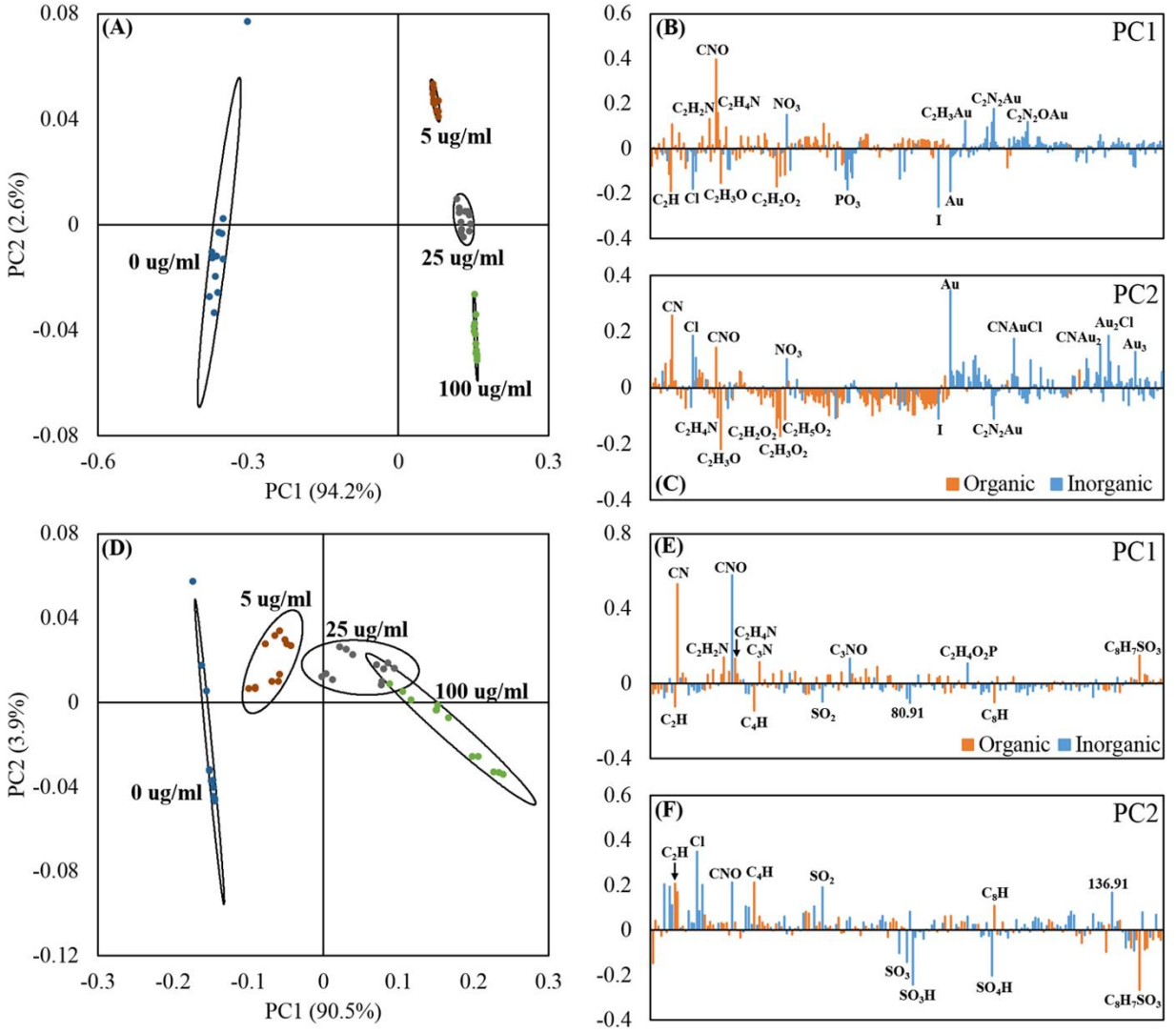

Figure S5.8. Adsorbed IgG PCA results using all peaks in the negative ion spectra. Panels A – C correspond to the scores and loadings plots for IgG adsorbed onto gold surfaces. Panels D – F correspond to the scores and loadings plots for IgG adsorbed onto NaSS surfaces.

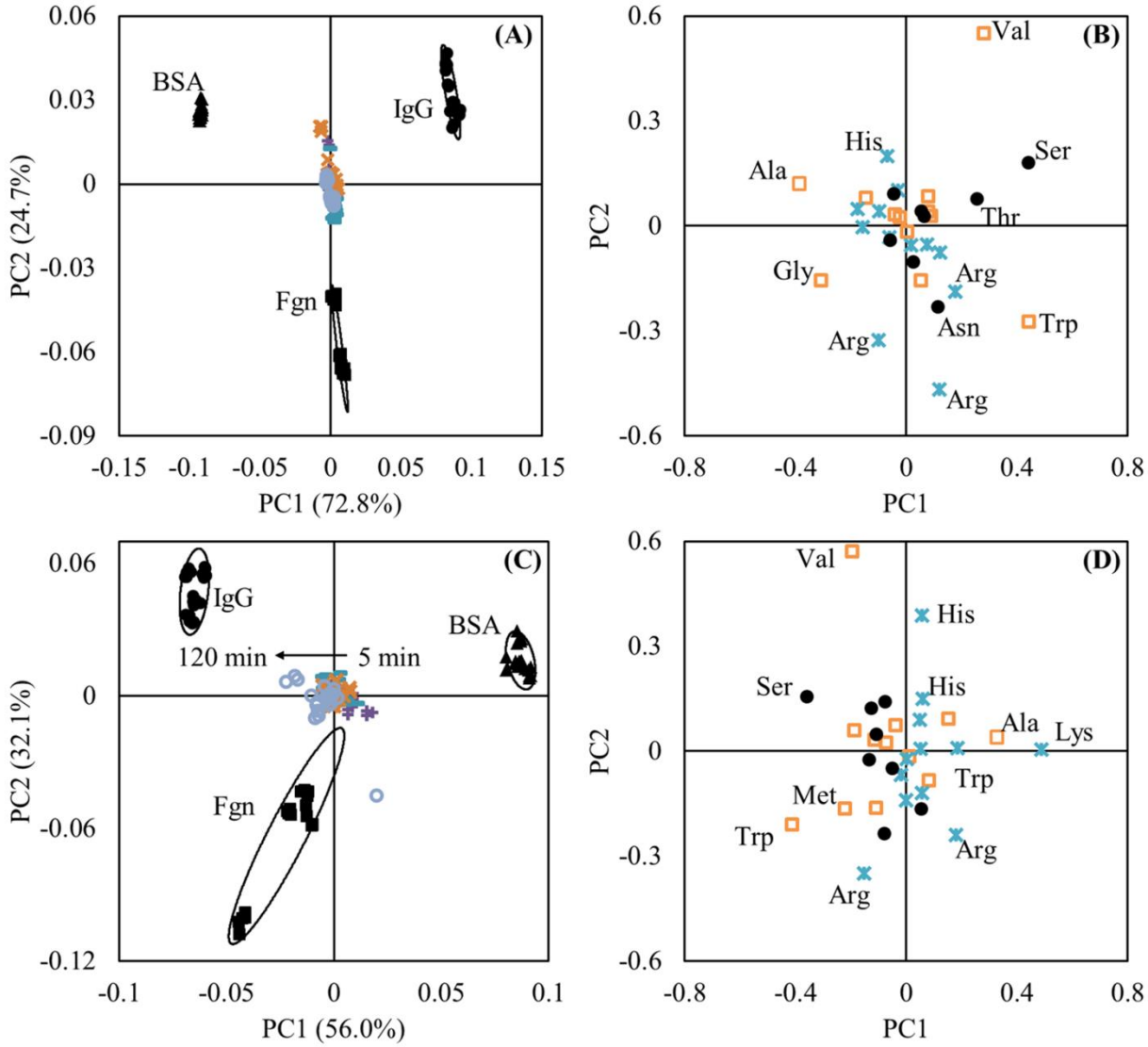

Figure S5.9. PC model constructed from the 100 µg/ml single-component protein adsorption ToF-SIMS spectra onto gold (A and B) and NaSS (C and D) surfaces. In panels (A) and (C) all black symbols represent the protein adsorption data used to construct the model: BSA (▲), Fgn (■), and IgG (●). Also in panels (A) and (C) the projected plasma data are represented as follows: (+) represent the 5 minute adsorption group, (—) represent the 30 minute adsorption group, (×) represent the 60 minute adsorption group, and (○) represent the 120 minute adsorption group.

6. Conclusions and Future Directions

6.1. Conclusions

As discussed in chapter 1, protein adsorption on synthetic surfaces is an important and widely studied phenomenon in biomaterials research. Despite its importance, it is still poorly understood. Therefore, the ultimate goal of this thesis is to contribute toward a better understanding of the protein-biomaterial interface, with application toward the next generation of biomaterial implants. Narrowing this broad objective down to something more specific, this thesis represents a body of work focused on the interaction of blood plasma proteins with sodium styrene sulfonate (NaSS) grafted surfaces. The approach to achieving this objective is straightforward. First, proof-of-concept must be established that NaSS can be successfully grafted to a given surface. This was the focus of chapter three, which details the thorough characterization of NaSS films grafted from titanium and silicon oxide surfaces using atom transfer radical polymerization (ATRP).

Next, the grafting procedure must be optimized and scaled in order to reliably produce sufficient quantities of NaSS-grafted samples to meet the demands of protein adsorption studies. This was the focus of chapter four, which describes the successful optimization of NaSS grafting from titanium and gold using a 2^4 factorial experimental design with "activators are continuously regenerated by electron transfer" (ARGET) ATRP chemistry. The optimized reaction conditions are as follows: (1) shorter ATRP-initiator surface functionalization reaction times, although no deleterious effects were observed at longer times; (2) minimum ($\leq$ 24 hr for this system) grafting reaction times; (3) minimum ($\leq$ 0.5 mg cm^{-2} for this system) catalyst concentration; and (4) sufficient excess of vitamin C, as no negative effects were detected with increasing concentrations.

The last step is application—to use the NaSS films for their intended purpose. This was the focus of chapter five, which describes the characterization of adsorbed bovine serum albumin (BSA), bovine fibrinogen (Fgn), bovine immunoglobulin G (IgG), and bovine plasma films on bare and NaSS-grafted gold surfaces. We found that at low solution concentrations all three proteins and plasma adsorb more readily to, and have a higher affinity for gold than NaSS surfaces. However, at higher concentrations NaSS adsorbs similar amounts (for plasma) or more (for BSA and Fgn) total protein than gold. This may be because any proteins that do adsorb to NaSS undergo structural rearrangements with time, increasing the number of contacts on the

surface and resulting in a larger fraction of irreversibly adsorbed species. The only protein that NaSS surfaces adsorb less of than gold is IgG. We found this to be because IgG adopts a highly denatured conformation on NaSS. Each adsorbed IgG molecule takes up more space on NaSS compared to gold surfaces, resulting in less total protein adsorbed at all concentrations. Still, with the exception of BSA and plasma on gold surfaces, neither surface appeared to have saturated at the highest protein solution concentration studied. Using principal component analysis (PCA) of just the amino acid ToF-SIMS mass fragments, we can distinguish between the same protein adsorbed on NaSS and gold surfaces, and also between proteins adsorbed from different solution concentrations onto the same surface. This suggests that proteins adsorb differently on NaSS and gold surfaces, and that the structure of the adsorbed protein film changes with surface concentration. Therefore, using peak ratios for buried/surface amino acids for each protein, we determined the degree of denaturation on each surface, and found that adsorbed proteins denature more on NaSS than gold surfaces. Also, using peak ratios for non-uniformly distributed amino acids we found small differences in average orientations between the two surfaces for BSA and IgG films. Using principal component (PC) modeling, we were also able to track changes in adsorbed plasma films with time. On NaSS surfaces the plasma films appear to be more BSA-like at short adsorption times, and more Fgn-like at longer adsorption times. Similarly, on gold surfaces the plasma films on appear to start out more IgG-like and become more Fgn-like with increasing adsorption time. However, the PC model included only the three proteins studied in chapter five, where plasma is a complex mixture of hundreds of proteins. Therefore, while both gold and NaSS appear to adsorb more Fgn with time, further study is required to confirm that this is truly representative of the final state of the adsorbed plasma films.

6.2. Future Directions

A main focus of the thesis of Wagner[133] is developing the statistical methods (one of which is PCA) for analyzing ToF-SIMS data of adsorbed proteins. He validated these methods through series of single-component and competitive adsorption studies using model surfaces such as mica. These surfaces are straightforward to prepare, allowing all the focus to be placed on method development. The work presented here is an extension of Wagner's work, applying his methodology to more complex and practically interesting surfaces. However, the time and effort

spent developing and optimizing the NaSS grafting procedure precluded any competitive adsorption studies. A logical next step would be to apply the methodology established in ref[127] to look at combinations of binary and ternary adsorbed protein films involving BSA, Fgn, and IgG on bare and NaSS-grafted gold surfaces. Also, in ref[134], XPS, ToF-SIMS, and radiolabeling were used to track the amount of Fgn adsorbed from plasma and serum solutions. Another straightforward continuation of the work in chapter 5 would be to use this methodology to confirm the results of the PC models, which suggest that plasma films on NaSS and gold become more Fgn-like with time.

Much of this work involves equilibrium measurements, and it would be interesting to study differences in adsorption kinetics on gold and NaSS surfaces using quartz crystal microbalance (QCM)[135-137] or surface plasmon resonance (SPR).[138, 139] Both are able to quantify the amount of protein adsorbed, assuming physically relevant models can be fit to the data. They also allow study of hydrated proteins films in an aqueous environment, in contrast to the ultra-high vacuum environment used in this thesis. Furthermore, both techniques can be used to study protein-antibody interactions, which is another clue regarding protein surface structure. If an antibody is able to bind an adsorbed protein, then the binding site must be oriented toward the solution interface and in a conformation close enough to native as to be recognized by the antibody.

The most obvious and perhaps beneficial future direction is to expand the work presented here to new grafted polymer systems. This thesis focused on protein interactions with a very specific surface chemistry: namely, sulfonated styrene with a sodium counter ion. What was developed along the way is a reliable and scalable method for making controlled changes in surface chemistry. This can be now used as a platform for future efforts, and the work here can be expanded to a wide variety of grafted polymer systems and surface chemistries. This could be as simple as studying changes in protein adsorption upon replacing the sodium counter ion with other alkali metals (Li, K, Cs) or alkaline earth metals (Mg, Ca). This may also produce interesting results related to the cationization of amino acid fragments in ToF-SIMS analysis. Other polymers may also be studied. For example, it would be interesting to quantify differences in protein adsorption between NaSS, styrene, and styrene with a positively charged quaternary amine head group—the negatively charged, neutral, and positively charged version of the same polymer. Thus, controlled changes in surface chemistry can be related to the properties of

adsorbed protein films in a continued effort to investigate the important factors dictating protein-surface interactions.

Bibliography

[1]G. Walter, K. Büssow, A. Lueking and J. Glökler, Trends Mol. Med. **8** (6), 250-253 (2002).

[2]H. Zhu and M. Snyder, Curr. Opin. Chem. Biol. **7** (1), 55-63 (2003).

[3]F. Rusmini, Z. Zhong and J. Feijen, Biomacromolecules **8** (6), 1775-1789 (2007).

[4]J. Ngunjiri, D. Stark, T. Tian, K. Briggman and J. Garno, Anal. Bioanal. Chem. **405** (6), 1985-1993 (2013).

[5]P. Cuatrecasas, J. Biol. Chem. **245** (12), 3059-3065 (1970).

[6]T. A. Horbett, Cardiovascular Pathology **2** (3, Supplement), 137-148 (1993).

[7]W. Kaewthong, S. Sirisansaneeyakul, P. Prasertsan and A. H-Kittikun, Process Biochem. **40** (5), 1525-1530 (2005).

[8]D. M. F. Prazeres and J. M. S. Cabral, Enzyme Microb. Technol. **16** (9), 738-750 (1994).

[9]J. L. Brash, J. Biomater. Sci. Polym. Ed. **11** (11), 1135-1146 (2000).

[10]M. Rabe, D. Verdes and S. Seeger, Adv. Colloid Interface Sci. **162** (1–2), 87-106 (2011).

[11]D. G. Castner and B. D. Ratner, Surf. Sci. **500** (1-3), 28-60 (2002).

[12]W. Norde, T. A. Horbett and J. L. Brash, in *Proteins at Interfaces III State of the Art* (American Chemical Society, 2012), Vol. 1120, pp. 1-34.

[13]O. Cohavi, S. Corni, F. De Rienzo, R. Di Felice, K. E. Gottschalk, M. Hoefling, D. Kokh, E. Molinari, G. Schreiber, A. Vaskevich and R. C. Wade, J. Mol. Recognit. **23** (3), 259-262 (2010).

[14]G. Pavon-Djavid, L. J. Gamble, M. Ciobanu, V. Gueguen, D. G. Castner and V. Migonney, Biomacromolecules **8** (11), 3317-3325 (2007).

[15]G. Helary, F. Noirclere, J. Mayingi, B. Bacroix and V. Migonney, J. Mater. Sci. Mater. Med. **21** (2), 655-663 (2010).

[16]G. Helary, F. Noirclere, J. Mayingi and V. Migonney, Acta Biomater. **5** (1), 124-133 (2009).

[17]A. Michiardi, G. Helary, P. C. T. Nguyen, L. J. Gamble, F. Anagnostou, D. G. Castner and V. Migonney, Acta Biomater. **6** (2), 667-675 (2010).

[18]C. Vaquette, V. Viateau, S. Guérard, F. Anagnostou, M. Manassero, D. G. Castner and V. Migonney, Biomaterials **34** (29), 7048-7063 (2013).

[19]J. Zhou, M. Manassero, V. Migonney and V. Viateau, IRBM **30** (4), 153-155 (2009).

[20]S. Kerner, V. Migonney, G. Pavon-Djavid, G. Helary, L. Sedel and F. Anagnostou, J. Mater. Sci. Mater. Med. **21** (2), 707-715 (2010).

[21]S. Edmondson, V. L. Osborne and W. T. S. Huck, Chem. Soc. Rev. **33** (1), 14-22 (2004).

[22]D. P. Curran, Synthesis **1988** (06), 417-439 (1988).

[23]R. G. W. Norrish and E. F. Brookman, Proceedings of the Royal Society of London. Series A, Mathematical and Physical Sciences **171** (945), 147-171 (1939).

[24]V. V. Naik, M. Crobu, N. V. Venkataraman and N. D. Spencer, The Journal of Physical Chemistry Letters, 2745-2751 (2013).

[25]A. Ulman, Adv. Mater. **2** (12), 573-582 (1990).

[26]A. Ulman, Chem. Rev. **96** (4), 1533-1554 (1996).

[27]C. N. Sukenik, N. Balachander, L. A. Culp, K. Lewandowska and K. Merritt, J. Biomed. Mater. Res. **24** (10), 1307-1323 (1990).

[28]V. Coessens, T. Pintauer and K. Matyjaszewski, Prog. Polym. Sci. **26** (3), 337-377 (2001).

[29]M. D. K. Ingall, C. H. Honeyman, J. V. Mercure, P. A. Bianconi and R. R. Kunz, J. Am. Chem. Soc. **121** (15), 3607-3613 (1999).

[30]K. Matyjaszewski, Macromolecules **45** (10), 4015-4039 (2012).

[31]R. Barbey, L. Lavanant, D. Paripovic, N. Schüwer, C. Sugnaux, S. Tugulu and H.-A. Klok, Chem. Rev. **109** (11), 5437-5527 (2009).

[32]K. Matyjaszewski and J. Xia, Chem. Rev. **101** (9), 2921-2990 (2001).

[33]K. Matyjaszewski, H. Dong, W. Jakubowski, J. Pietrasik and A. Kusumo, Langmuir **23** (8), 4528-4531 (2007).

[34]P. W. Hoffmann, M. Stelzle and J. F. Rabolt, Langmuir **13** (7), 1877-1880 (1997).

[35]S. Onclin, B. J. Ravoo and D. N. Reinhoudt, Angew. Chem. Int. Ed. **44** (39), 6282-6304 (2005).

[36]A. J. Keefe, N. D. Brault and S. Jiang, Biomacromolecules **13** (5), 1683-1687 (2012).

[37]T. L. Barr and S. Seal, Journal of Vacuum Science & Technology A **13** (3), 1239-1246 (1995).

[38]G. C. Smith, J. Electron. Spectrosc. Relat. Phenom. **148** (1), 21-28 (2005).

[39]S. Bierbaum, V. Hintze and D. Scharnweber, Biomatter **2** (3), 132-141 (2012).

[40]W. Norde and J. Lyklema, J. Colloid Interface Sci. **71** (2), 350-366 (1979).

[41]L. B. John, in *Proteins at Interfaces III State of the Art* (American Chemical Society, 2012), Vol. 1120, pp. 277-300.

[42]J. E. Baio, T. Weidner, L. Baugh, L. J. Gamble, P. S. Stayton and D. G. Castner, Langmuir **28** (4), 2107-2112 (2011).

[43]J. Baio, T. Weidner, D. Ramey, L. Pruzinsky and D. Castner, Biointerphases **8** (1), 1-8 (2013).

[44]D. G. Castner, Nature **422** (6928), 129-130 (2003).

[45]B. D. Ratner, A. Chilkoti and D. G. Castner, Clin. Mater. **11** (1–4), 25-36 (1992).

[46]B. D. Ratner and D. G. Castner, in *Surface Analysis – The Principal Techniques* (John Wiley & Sons, Ltd, 2009), pp. 47-112.

[47]J. C. Vickerman, in *Surface Analysis – The Principal Techniques* (John Wiley & Sons, Ltd, 2009), pp. 113-205.

[48]M. A. Robinson, Ph.D., University of Washington, 2013.

[49]J. L. S. Lee and I. S. Gilmore, in *Surface Analysis – The Principal Techniques* (John Wiley & Sons, Ltd, 2009), pp. 563-612.

[50]R. N. Foster, A. J. Keefe, S. Jiang and D. G. Castner, Journal of Vacuum Science & Technology A: Vacuum, Surfaces, and Films **31** (6), 06F103-109 (2013).

[51]G. J. Leggett, in *Surface Analysis – The Principal Techniques* (John Wiley & Sons, Ltd, 2009), pp. 479-562.

[52]http://blog.brukerafmprobes.com/2011/06/spm-operation-2/.

[53]T. Kokubo, D. K. Pattanayak, S. Yamaguchi, H. Takadama, T. Matsushita, T. Kawai, M. Takemoto, S. Fujibayashi and T. Nakamura, J. R. Soc. Interface **7** (Suppl 5), S503-S513 (2010).

[54]S. Ban, Y. Iwaya, H. Kono and H. Sato, Dent. Mater. **22** (12), 1115-1120 (2006).

[55]X. Liu, P. K. Chu and C. Ding, Mater. Sci. Eng., R **47** (3–4), 49-121 (2004).

[56]L. Le Guéhennec, A. Soueidan, P. Layrolle and Y. Amouriq, Dent. Mater. **23** (7), 844-854 (2007).

[57]G. Zorn, J. E. Baio, T. Weidner, V. Migonney and D. G. Castner, Langmuir **27** (21), 13104-13112 (2011).

[58]S. Tugulu and H.-A. Klok, Biomacromolecules **9** (3), 906-912 (2008).

[59]F. J. Xu, E. T. Kang and K. G. Neoh, J. Mater. Chem. **16** (28), 2948-2952 (2006).

[60]F. J. Xu, Y. Song, Z. P. Cheng, X. L. Zhu, C. X. Zhu, E. T. Kang and K. G. Neoh, Macromolecules **38** (15), 6254-6258 (2005).

[61]F. J. Xu, D. Xu, E. T. Kang and K. G. Neoh, J. Mater. Chem. **14** (17), 2674-2682 (2004).

[62]C.-Y. Tu, Y.-L. Liu, K.-R. Lee and J.-Y. Lai, Polymer **46** (18), 6976-6985 (2005).

[63]Y.-L. Liu, M.-T. Luo and J.-Y. Lai, Macromol. Rapid Commun. **28** (3), 329-333 (2007).

[64]W. H. Yu, E. T. Kang and K. G. Neoh, Langmuir **21** (1), 450-456 (2004).

[65]G. Zhai, E. T. Kang and K. G. Neoh, Macromolecules **37** (19), 7240-7249 (2004).

[66]Y. Xiao-He, Y. Qiang, Y. Hao, W. Li and C. Yu-Quan, Chinese Journal of Analytical Chemistry **35** (12), 1751-1755 (2007).

[67]H. Kong, P. Luo, C. Gao and D. Yan, Polymer **46** (8), 2472-2485 (2005).

[68]E. Marutani, S. Yamamoto, T. Ninjbadgar, Y. Tsujii, T. Fukuda and M. Takano, Polymer **45** (7), 2231-2235 (2004).

[69]Z. Lei, Y. Li and X. Wei, J. Solid State Chem. **181** (3), 480-486 (2008).

[70]X. Chen, D. P. Randall, C. Perruchot, J. F. Watts, T. E. Patten, T. von Werne and S. P. Armes, J. Colloid Interface Sci. **257** (1), 56-64 (2003).

[71]Z. Lei, S. Bi, B. Hu and H. Yang, Food Chem. **105** (3), 889-896 (2007).

[72]C.-D. Vo, A. Schmid, S. P. Armes, K. Sakai and S. Biggs, Langmuir **23** (2), 408-413 (2006).

[73]A. Y. Sankhe, S. M. Husson and S. M. Kilbey, J. Polym. Sci., Part A: Polym. Chem. **45** (4), 566-575 (2007).

[74]M. S. Wagner, B. J. Tyler and D. G. Castner, Anal. Chem. **74** (8), 1824-1835 (2002).

[75]M. S. Wagner, D. J. Graham, B. D. Ratner and D. G. Castner, Surf. Sci. **570** (1–2), 78-97 (2004).

[76]M. S. Wagner, D. J. Graham and D. G. Castner, Appl. Surf. Sci. **252** (19), 6575-6581 (2006).

[77]D. J. Graham and D. G. Castner, Biointerphases **7** (1-4), 1-12 (2012).

[78]D. J. Graham and D. G. Castner, Mass Spectrometry **2** (Special_Issue), S0014-S0014 (2013).

[79]C.-K. Choi and Y.-B. Kim, Polym. Bull. **49** (6), 433-439 (2003).

[80]J. V. M. Weaver, I. Bannister, K. L. Robinson, X. Bories-Azeau, S. P. Armes, M. Smallridge and P. McKenna, Macromolecules **37** (7), 2395-2403 (2004).

[81]D. G. Castner and B. D. Ratner, Surf. Interface Anal. **15** (8), 479-486 (1990).

[82]G. Beamson and D. Briggs, *High Resolution XPS of Organic Polymers: The Scienta ESCA300 Database*. (John Wiley & Sons Ltd, Chichester, 1992).

[83]S. D. Techane, L. J. Gamble and D. G. Castner, J. Phys. Chem. C **115** (19), 9432-9441 (2011).

[84]C. D. Wagner, W. M. Riggs, L.E.Davis and J. F. Moulder, *Handbook of X-Ray Photoelectron Spectroscopy*. (Perkin-Elmer Corporation Physical Electronics Division, Eden Prairie, MN, 1979).

[85]A. Chilkoti, D. G. Castner and B. D. Ratner, Appl. Spectrosc. **45** (2), 209-217 (1991).

[86]Y. L. Jeyachandran, B. Karunagaran, S. K. Narayandass, D. Mangalaraj, T. E. Jenkins and P. J. Martin, Mater. Sci. Eng., A **431** (1–2), 277-284 (2006).

[87]D. Bhattacharyya, N. K. Sahoo, S. Thakur and N. C. Das, Thin Solid Films **360** (1–2), 96-102 (2000).

[88]L. Sun and P. Hou, Thin Solid Films **455–456** (0), 525-529 (2004).

[89]A. Franquet, H. Terryn, P. Bertrand and J. Vereecken, Surf. Interface Anal. **34** (1), 25-29 (2002).

[90]B. Johs and J. S. Hale, physica status solidi (a) **205** (4), 715-719 (2008).

[91]J. A. W. C. Inc., CompleteEase TM software manual (version 4.63) (ed. 2011).

[92]L. A. A. Pettersson, S. Ghosh and O. Inganäs, Org. Electron. **3** (3–4), 143-148 (2002).

[93]N. Vogel, M. Jung, M. Retsch, W. Knoll, U. Jonas and I. Köper, Small **5** (7), 821-825 (2009).

[94]S. R. Wasserman, Y. T. Tao and G. M. Whitesides, Langmuir **5** (4), 1074-1087 (1989).

[95]B. Zhao and W. J. Brittain, Prog. Polym. Sci. **25** (5), 677-710 (2000).

[96]R. Jordan, A. Ulman, J. F. Kang, M. H. Rafailovich and J. Sokolov, J. Am. Chem. Soc. **121** (5), 1016-1022 (1999).

[97]J. Huang, H. Murata, R. R. Koepsel, A. J. Russell and K. Matyjaszewski, Biomacromolecules **8** (5), 1396-1399 (2007).

[98]T. Matsugi, J. Saito, N. Kawahara, S. Matsuo, H. Kaneko, N. Kashiwa, M. Kobayashi and A. Takahara, Polym. J **41** (7), 547-554 (2009).

[99]M. Himmelhaus, F. Eisert, M. Buck and M. Grunze, The Journal of Physical Chemistry B **104** (3), 576-584 (2000).

[100]J. Qiu and K. Matyjaszewski, Macromolecules **30** (19), 5643-5648 (1997).

[101]C.-H. Peng, J. Kong, F. Seeliger and K. Matyjaszewski, Macromolecules **44** (19), 7546-7557 (2011).

[102]A. K. Nanda and K. Matyjaszewski, Macromolecules **36** (3), 599-604 (2003).

[103]W. Jakubowski and K. Matyjaszewski, Angew. Chem. Int. Ed. **45** (27), 4482-4486 (2006).

[104]W. Jakubowski, K. Min and K. Matyjaszewski, Macromolecules **39** (1), 39-45 (2006).

[105]J. Listak, W. Jakubowski, L. Mueller, A. Plichta, K. Matyjaszewski and M. R. Bockstaller, Macromolecules **41** (15), 5919-5927 (2008).

[106]K. Min, H. Gao and K. Matyjaszewski, Macromolecules **40** (6), 1789-1791 (2007).

[107]M. Ciobanu, A. Siove, V. Gueguen, L. J. Gamble, D. G. Castner and V. Migonney, Biomacromolecules **7** (3), 755-760 (2006).

[108]D. C. Montgomery, *Design and Analysis of Experiments*. (John Wiley & Sons, Inc., 2005).

[109]A. Y. Fadeev and T. J. McCarthy, Langmuir **16** (18), 7268-7274 (2000).

[110]Y. Iwasaki and N. Saito, Colloids Surf. B. Biointerfaces **32** (1), 77-84 (2003).

[111]J. C. Conboy, M. C. Messmer and G. L. Richmond, The Journal of Physical Chemistry **100** (18), 7617-7622 (1996).

[112]F. Vidal and A. Tadjeddine, Rep. Prog. Phys. **68** (5), 1095 (2005).

[113]P. Guyot-Sionnest, R. Superfine, J. H. Hunt and Y. R. Shen, Chem. Phys. Lett. **144** (1), 1-5 (1988).

[114]P. B. Miranda and Y. R. Shen, The Journal of Physical Chemistry B **103** (17), 3292-3307 (1999).

[115]H. Asanuma, H. Noguchi, K. Uosaki and H.-Z. Yu, The Journal of Physical Chemistry B **110** (10), 4892-4899 (2006).

[116]Y. Tateishi, N. Kai, H. Noguchi, K. Uosaki, T. Nagamura and K. Tanaka, Polymer Chemistry **1** (3), 303-311 (2010).

[117]F. Fang and I. Szleifer, Biophys. J. **80** (6), 2568-2589 (2001).

[118]J. J. Gray, Curr. Opin. Struct. Biol. **14** (1), 110-115 (2004).

[119]C. A. Haynes, E. Sliwinsky and W. Norde, J. Colloid Interface Sci. **164** (2), 394-409 (1994).

[120]E. Bittrich, S. Burkert, K.-J. Eichhorn, M. Stamm and P. Uhlmann, in *Proteins at Interfaces III State of the Art* (American Chemical Society, 2012), Vol. 1120, pp. 179-193.

[121]C. A. Haynes and W. Norde, Colloids Surf. B. Biointerfaces **2** (6), 517-566 (1994).

[122]R. N. Foster, P. K. Johansson, N. R. Tom, P. Koelsch and D. G. Castner, Journal of Vacuum Science & Technology A: Vacuum, Surfaces, and Films **Accepted** (2015).

[123]M. S. Wagner and D. G. Castner, Langmuir **17** (15), 4649-4660 (2001).

[124]R. A. Latour, Journal of Biomedical Materials Research Part A **103** (3), 949-958 (2015).

[125]C. D. Tidwell, D. G. Castner, S. L. Golledge, B. D. Ratner, K. Meyer, B. Hagenhoff and A. Benninghoven, Surf. Interface Anal. **31** (8), 724-733 (2001).

[126]M. S. Wagner, M. Shen, T. A. Horbett and D. G. Castner, Journal of Biomedical Materials Research Part A **64A** (1), 1-11 (2003).

[127]M. S. Wagner, T. A. Horbett and D. G. Castner, Langmuir **19** (5), 1708-1715 (2003).

[128]J. R. Hull, G. S. Tamura and D. G. Castner, Biophys. J. **93** (8), 2852-2860.

[129]J. E. Baio, T. Weidner, N. T. Samuel, K. McCrea, L. Baugh, P. S. Stayton and D. G. Castner, Journal of Vacuum Science & Technology B **28** (4), C5D1-C5D8 (2010).

[130]L. Baugh, T. Weidner, J. E. Baio, P.-C. T. Nguyen, L. J. Gamble, P. S. Stayton and D. G. Castner, Langmuir **26** (21), 16434-16441 (2010).

[131]N. Xia and D. G. Castner, Journal of Biomedical Materials Research Part A **67A** (1), 179-190 (2003).

[132]J. D. Andrade and V. Hlady, Ann. N. Y. Acad. Sci. **516** (1), 158-172 (1987).

[133]M. Wagner, 2002.

[134]M. S. Wagner, T. A. Horbett and D. G. Castner, Biomaterials **24** (11), 1897-1908 (2003).

[135]M. Rodahl, F. Hook, C. Fredriksson, C. A. Keller, A. Krozer, P. Brzezinski, M. Voinova and B. Kasemo, Faraday Discuss. **107** (0), 229-246 (1997).

[136]P. Roach, D. Farrar and C. C. Perry, J. Am. Chem. Soc. **127** (22), 8168-8173 (2005).

[137]F. Höök, J. Vörös, M. Rodahl, R. Kurrat, P. Böni, J. J. Ramsden, M. Textor, N. D. Spencer, P. Tengvall, J. Gold and B. Kasemo, Colloids Surf. B. Biointerfaces **24** (2), 155-170 (2002).

[138]V. Silin, H. Weetall and D. J. Vanderah, J. Colloid Interface Sci. **185** (1), 94-103 (1997).

[139]V. Silin and A. Plant, Trends Biotechnol. **15** (9), 353-359 (1997).